Master's Thesis

Metal surface adsorbed retinoic acid as a Kondo switch:
Ab initio investigations of isomerization and spin localization

Georg S. Michelitsch

Georg Siegmund Michelitsch, BSc

Metal surface adsorbed retinoic acid as a Kondo switch: Ab initio investigations of isomerization and spin localization

MASTERARBEIT

zur Erlangung des akademischen Grades

Master of Science

Masterstudium Chemie

eingereicht an der

Technischen Universität Graz

Betreuer
Ao.Univ.-Prof. Dr.phil. Alexander F. Sax
Univ.-Prof. Dr. Dipl.-Phys. Karsten Reuter

Institut für Chemie, Physikalische und Theoretische Chemie, Universität Graz
Lehrstuhl für Theoretische Chemie, Technische Universität München

Zweitbetreuer
Mag. Dr. Reinhard J. Maurer
Dr. Dipl.-Phys. Univ. Katharina Diller

Graz, Juni 2014

Abstract

Current strategies for increasing performance and at the same time decreasing the size of electronic devices are based on the miniaturization of their most basic functional units. The physical limit of the established techniques, however, will be reached soon. One alternative approach towards new kinds of miniaturized logical elements is based on molecular electronics, i.e., using molecules as building blocks which replace the current semiconductor-based components. One of the most fundamental elements is a switch, which is not only crucial in logical electronics, but plays an important role in a multitude of additional applications, such as controllable surface functionalization or data storage. It was recently discovered that the organic compound retinoic acid can act as such a molecular switch, i.e., it can be reversibly switched between four different states on a Au(111) surface by applying a bias voltage through a scanning tunneling microscopy (STM) tip. Concurrently, the corresponding dI/dV curves suggest the presence of a Kondo-effect, usually associated with the presence of an unpaired electron spin. The goal of this thesis is to identify the geometry and electronic structure of the switching intermediates from first-principles calculations in order to justify the experimentally observed changes using a molecular model. In order to reduce the computational requirements to simulate the molecule on the metal surface, an embedding model based on the separation of short-range density-functional-theory contributions and the long-range dispersive interactions was implemented and tested. Before the surface was explicitly included in the simulations, retinoic acid was studied in gas phase, which led to the discovery of first indications on a correlation between the electronic and geometric structure. However, the metal-induced switching mechanism can not be rationalized without considering the substrate. Subsequently, an extensive structural analysis of metal-adsorbed retinoic acid was conducted using density-functional-tight-binding and the implemented van-der-Waals embedding model. In this context, 122 starting geometries were reduced to 18 chemically relevant adsorbate geometries. These 18 geometries were compared with the experimental results by means of Tersoff-Hamann simulated STM topographs. It could be shown that the observed appearance of the switched states can be explained on the grounds of geometrical changes alone. Finally, the obtained DFTB geometries and corresponding Tersoff-Hamann images of four typical isomers were verified using full DFT calculations.

Kurzfassung

Die gegenwärtige Strategie um die Leistungsfähigkeit elektronischer Geräte zu steigern und zeitgleich selbige zu verkleinern, besteht darin deren grundlegenste funktionale Einheiten zu miniaturisieren. Allerdings wird das physikalische Limit der aktuell etablierten Techniken bald erreicht sein. Eine der alternativen Methoden zur Realisierung kleinerer Bausteine baut auf *molekulare Elektronik* auf, wobei Moleküle verwendet werden um Halbleiter-basierte Komponenten zu ersetzen. Einer der grundlegensten logischen Bausteine ist ein Schalter, welcher nicht nur von entscheidender Bedeutung in logischer Elektronik ist, sondern auch in vielen anderen Bereichen Anwendung findet, beispielsweise zur kontrollierbaren Oberflächenfunktionalisierung oder als Datenspeicher. Erst kürzlich wurde entdeckt, dass die organische Verbindung Retinolsäure als molekularer Schalter verwendet werden kann: Durch das Anlegen einer Spannung an der Spitze eines Rastertunnelmikroskops (scanning tunneling microscope - STM) kann reversibel zwischen vier unterschiedlichen Zuständen auf einer Au(111) Oberfläche geschalten werden. Gleichzeitig zeugt die Form der gemessenen dI/dV Kurven von der Anwesenheit eines Kondo-Effekts, welcher üblicherweise auf die Präsenz eines ungepaarten Elektrons zurückzuführen ist. Das Ziel der vorliegenden Arbeit ist es, die Geometrie und Elektronenstruktur der Schaltintermediate mittels quantenchemischer Rechnungen zu identifizieren und die experimentell beobachteten Änderungen mithilfe eines molekularen Modells zu begründen. Um die rechnerischen Anforderungen der Simulation des Moleküls auf der Metalloberfläche zu reduzieren, wurde eine Einbettungsmethode basierend auf der Trennung des kurzreichweitigen Dichtefunktionalanteils und des langreichweitigen Dispersionsanteils implementiert und getestet. Bevor die Oberfläche explizit in die Berechnungen miteinbezogen wurde, wurde Retinolsäure in der Gasphase untersucht, wodurch erste Anhaltspunkte auf eine Korrelation zwischen der elektronischen und geometrischen Struktur entdeckt wurden. Der metall-induzierte Schaltmechanismus kann jedoch ohne explizite Berücksichtigung des Substrates nicht rationalisiert werden. Darauffolgend wurde eine ausgedehnte Strukturanalyse metalladsorbierter Retinolsäure mittels Dichtefunktional-Tight-Binding und dem implementierten van-der-Waals Einbettungsmodell durchgeführt. Hierbei wurden 122 Startgeometrien auf 18 chemisch relevante Adsorbatgeometrien reduziert. Diese 18 Geometrien wurden mittels Tersoff-Hamann simulierter STM-Topographien mit den experimentellen Ergebnissen verglichen. Hierbei zeigte sich, dass das beobachtete Erscheinungsbild der geschaltenen Zustände bereits nur auf Basis der Geometrieänderungen verstanden werden kann. Schlussendlich wurden die Geometrien und STM-Topographien von vier charakteristischen Isomeren mittels Dichtefunktionaltheorie validiert.

EIDESSTATTLICHE ERKLÄRUNG

AFFIDAVIT

Ich erkläre an Eides statt, dass ich die vorliegende Arbeit selbstständig verfasst, andere als die angegebenen Quellen/Hilfsmittel nicht benutzt, und die den benutzten Quellen wörtlich und inhaltlich entnommenen Stellen als solche kenntlich gemacht habe. Das in TUGRAZonline hochgeladene Textdokument ist mit der vorliegenden Masterarbeit identisch.

I declare that I have authored this thesis independently, that I have not used other than the declared sources/resources, and that I have explicitly indicated all material which has been quoted either literally or by content from the sources used. The text document uploaded to TUGRAZonline is identical to the present master's thesis.

Datum / Date	Unterschrift / Signature

Contents

Chapter 1

Introduction

Probably the first two words learned in a new language are the equivalents of *yes* and *no*, because they enable communication on a rudimentary level. It was stated by G. Boole in his introduction to *The mathematical analysis of logic* that the concept of a language was intimately connected with logic, since the language itself is only a way to express an impression of the human mind [1]. It is therefore not surprising that at the base of *technical languages*, which enable humans to communicate with machines, these two words are found again in the form of *binary logic*. Inside modern computers, a multitude of electronic miniature components perform logical operations involving only the two signals *yes* (`True`) or *no* (`False`) encoded in the current flowing through them. Prior to the invention of the transistor - a logical electronic component, which performs the aforementioned operations within the size of a few tenths of nanometers - computers commonly occupied the space of a whole room and were based on the much larger and fragile vacuum tubes such as the first electrical computer ENIAC [2] or mechanically driven ones such as the early versions of ZUSE [3]. The quick development of computers is showcased by the fact of the first commercially available computer, built less than a century ago, being capable of one mathematical operation per second [4], whereas the average mobile phone nowadays already exceeds this by a factor of 10^9. With decreasing size and increasing performance, computers became customary objects of everyday life and are indispensable in fields such as science, medicine, the automotive industry, or the banking sector, to name only a few.

In the second half of the 20th century Moore predicted that every two years the number of transistors on integrated circuits doubles [5]. This prediction is still valid until today. However, by continuing miniaturization mankind is slowly reaching the physical limit of the established techniques and architectures, while the demand of more powerful and at the same time smaller computer components is still present. One suggested approach towards smaller logical elements is based on *molecular electronics*, i.e. using small molecules to substitute the currently used transistors, etc. Because of the inherent fragility of small molecules, the principal idea is to stabilize them by adsorption on a support. One of the elementary building blocks required for the realization of such computational logic is a switch, which can be set to at least two distinguishable states corresponding to the initially introduced vocabulary of `True` and `False`. Of course, the requirements imposed on such a molecular switch are well-defined: distinguishable and reversible switching between long-time stable states. Fulfilling these requirements, a molecule can be used to store information in a binary, ternary or even higher base system, ideally while tightly packed structures on a surface reduce the effective space needed for storage by orders of magnitudes.

Furthermore, molecules capable of switching on a surface are of ubiquitous importance in other fields, as they were also shown to selectively control the surface-behavior of new *smart* materials by enabeling them to switch between hydrophobic and hydrophilic behavior [6–9], move on a surface in a controllable manner in lateral directions [10], or mechanically, comparable to a motor [11]. These

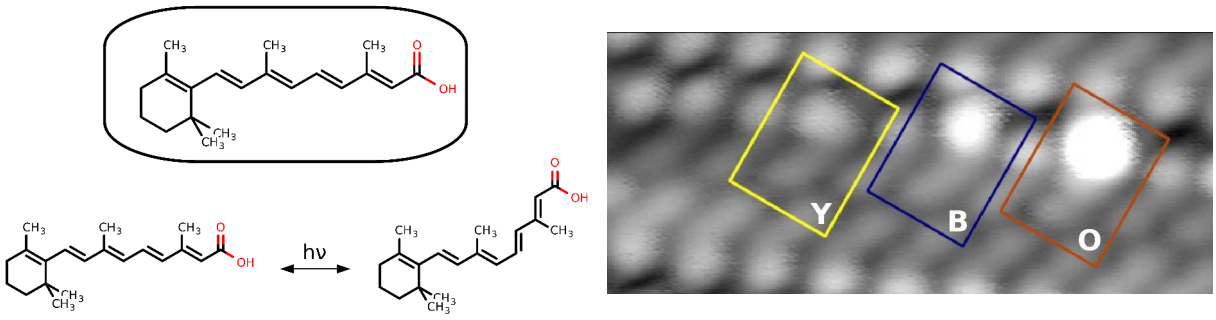

Figure 1.1: Left: *Chemical structure of all-trans[1] retinoic acid (ReA, top). Incident UV-Vis radiation is known to switch the C-11[2] bond in the polyene chain from its trans- to the cis-state (bottom, [14]).*

Right: *Experimental STM topograph of dense packed ReA molecules on a Au(111) surface [24]. After the application of a bias voltage at the STM tip, three new states (Y, B, O, indicated by boxes) are distinguishable.*

molecular switches are triggered by different external stimuli such as UV radiation, temperature, changes in pH, and reversible reduction-oxidation by applying an electrical potential [12]. Clearly, their functionality is determined by the presence of a *switchable* moiety, such as represented by a double bond [13]. A molecule, which fulfills this prerequisite of switchable double bonds and is well-known due to its biological importance is retinoic acid (ReA, shown in Figure 1.1), the active species within the protein receptor responsible for eyesight in mammals [14]. So far, photochemical switching and the electronic transitions associated were studied in detail [15–18], however just recently the behavior of surface-adsorbed retinoic acid sparked interest, when different regular adsorption patterns were observed on a Au(111) surface with Scanning Tunneling Microscopy (STM) [19].

Developed in the late 20th century [20], STM has become one of the standard techniques in experimental surface analysis nowadays. In this method a metallic probing tip is placed within a very short distance of the sample. Due to the proximity it is possible that electrons tunnel over this junction. Two methods of operation can be used in STM: Either the piezoelectric motor of the STM tip is coupled to a feedback-loop which ensures that the current is kept constant by vertical adjustment (constant current mode), or the vertical distance is kept fixed and the associated current is measured (constant height mode). In either case, the received signal is transformed into a STM topograph, which represents an atomic-resolution image of the surface. With or without adsorbates present on the surface, these topographs usually exhibit distinct features ("protrusions"). However, in contrast to the classical picture, a protrusion in a STM topograph does not have to correlate with a geometrical feature of the surface or adsorbate but can equally well correspond to a change in the electronic structure such as the presence of electron-rich atoms. Not only can the tip be used for recording STM topographs, it can more actively interact with the surface or adsorbate on a molecular level, pushing single atoms [21], forming chemical bonds, [22] or (as being investigated in this work) inducing geometrical changes within a molecule [23].

Deposition of evaporated all-trans retinoic acid on Au(111) led to the assembly of distinct patterns on the surface corresponding to dimeric (as shown in Figure 1.1), tetrameric and pentameric arrangements of the molecule as a function of the coverage [19]. Recent experimental STM results of our collaborators [24] suggest a switching capability of retinoic acid adsorbed to a Au(111) surface upon stimulation by inelastic electron tunneling. The observed STM topographs show three distinct

[1] In this work the cis/trans nomenclature instead of the E/Z designation of bond arrangements is used. The designations exclusively relate to the conformation of double bonds incorporating carbon atoms C5-C15.

[2] The enumeration of carbon atoms in retinoic acid used in this work is based upon the recommended nomenclature of carotenoids [25].

states (**Y**,**B**, and **O**), which can be reversibly switched from an initial state **N** as shown in Figure 1.1. Furthermore, the switching ability was found to be independent of the arrangement of the molecules on the surface. The exact geometry of the adsorbed molecule **N** as well as the nature of the switched states **Y**,**B**, and **O** is not known. It was assumed that cis/trans isomerization of a double bond in vicinity of the cyclohexene-ring or other geometrical distorsions in this region are involved in the appearance of the bright protrusions [24]. In addition, for the unswitched ReA molecule and each of the switched states obtained after inelastic electron tunneling with a bias voltage of -2.5 V, the dI/dV curves shown in Figure 1.2 were recorded. The narrow spectroscopic feature seen within the switched states **Y**,**B**, and **O** is associated with a so-called Kondo-effect [26, 27], which was first experimentally observed in 1934 [28]. The macroscopic manifestation of the Kondo effect is a peculiar

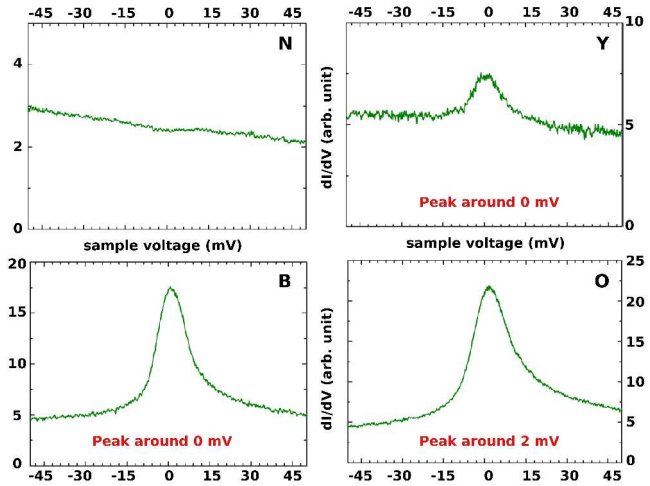

Figure 1.2: *Experimentally observed dI/dV diagram which shows a peak around 0 mV for each of the states observed in Figure 1.1. This phenomenon occurs only below the Kondo-temperature and vanishes above - it is the accepted evidence of a Kondo-effect within the studied system [26].*

dI/dV diagrams of states in Figure 1.1 (fltr):
N: *unswitched stated*
Y: *switched state within yellow rectangle*
B: *switched state within blue rectangle*
O: *switched state within orange rectangle*

behavior of the resistivity of a material at very low temperatures: Below a certain temperature (the Kondo temperature T_K), the resistance of some materials increases instead of reaching a saturation point after decreasing, as it is usually observed. The material then either becomes superconducting or the resistance again asymptotically approaches a material-specific value.
The Kondo effect was explained by the interaction of an unpaired electron spin (i.e. within a magnetic ion or atom) with the conducting electrons of the material. The electrons are scattered at this impurity, therefore reducing the conductivity ($\propto$ resistance^{-1}), as described for the first time theoretically by Kondo [27] within the scope of perturbation theory.

A Kondo effect of an adsorbed molecule is usually known from transition metal complexes [29, 30] and was also already observed in organic charge-transfer assemblies [31] but has not yet been observed on single weakly-adsorbed organic molecules. It is unclear whether or not the observed states in Figure 1.1 are solely based on geometric rearrangements of the molecule on the surface or if changes in the electronic structure are the dominant contribution leading to increased brightness of the protrusions. Furthermore, a Kondo effect involves the presence of an unpaired electron (*vide supra*), which is chemically unintuitive in conjunction with an organic molecule, since organic radicals are usually known to be highly reactive and short-lived, whereas in the present case reversible non-destructive switching is observed. It is therefore the motivation of this work to disentangle geometric and magnetic effects contributing to the observed signature and identify the correct electronic structure associated with the Kondo-behavior observed experimentally.
Identification of the correct electronic structure of an adsorbate however has one important prerequisite: the knowledge of the exact adsorption geometry. If computational chemistry is applied to model and reproduce experimental findings, a common approach to adress this requirement is the usage of crystal structures or optimized geometries from high-level theory of the compound in the gas phase. However, the present situation is different due to the presence of the surface which affects the adsorbate geometry and reactivity in an initially unknown manner. Typically, physisorption

and chemisorption as well as long-range interactions between neighboring surface molecules mesh together and result in a complex many-body dependence on the final result. Unfortunately, it is impossible to account for all these effects simultaneously, because the computational effort connected with that approach is simply too large. Therefore, in the course of this thesis a simplified embedding model is conceived and implemented which aims to include the majority of aforementioned effects while keeping the computational cost affordable. After implementation and successful testing of this new methodology, current state-of-the-art dispersion-corrected Density-Functional Theory will be used to analyze the obtained geometries and reproduce the experimental findings.

This work is organized in five separate chapters. The first (Chapter 2) introduces the underlying theoretical models, including all approximations which allow the calculations of the electronic structure. It contains a short introduction of wave function theory, Hartree Fock, Density-Functional Theory (DFT), van-der-Waals corrections in DFT, Density-Functional Tight Binding, and Tersoff-Hamann simulations of STM topographs.
Chapter 3 introduces the implementation of an embedding model developed in the course of this thesis in order to simplify the identification of adsorbate geometries within a computational screening approach employed in Chapter 5. The embedding approach aims to reduce the computational requirements by embedding the adsorbate and a few additional layers of gold atoms within a periodic system of only dispersively interacting metal atoms. One major point in this chapter is the analysis of the validity and convergence behavior of this approach for physisorbed and chemisorbed test systems.
In order to first understand the electronic structure of retinoic acid, Chapter 4 encompasses a description of the electronic structure of several gas phase isomers of this molecule and their electronic and geometric properties within different electronic configurations.
Chapter 5 presents the screening approach employed to find the most probable adsorbate geometry on the surface and preliminary simulations of STM topographs on the level of dispersion-corrected Density-Functional Tight Binding as well as a final description of selected geometries using a full DFT description.
Chapter 6 summarizes the results obtained, analyzes which conclusions can be drawn, and gives an outlook to further development on the basis of this work.

Chapter 2

Theoretical Background

Quantum mechanics has puzzled scientists for the better part of the last century. The most important approaches to make quantum mechanical behavior accessible in conjunction with the calculations in this work are briefly outlined here. The following chapter is largely based on the work of Levine [32], Szabo and Ostlund [33], and McQuarrie [34]. The section on density functional theory additionally relates to the introductory work of Koch and Holthausen [35].

2.1 The Many-Body Problem

Quantum Chemistry deals with the problem of finding an accurate value of a given observable by initially only knowing the molecular structure of a given system. Therefore the methods which enable these observations are known as *ab initio* or *first principles* methods. As it became apparent with the dawn of quantum mechanics that microscopic particles can be described as behaving like waves, Schrödinger introduced the idea of using a wave function as the basis for calculating the energy of the system [36]:

$$i\hbar\frac{\partial}{\partial t}\Psi(\vec{r},t) = \hat{H}\Psi(\vec{r},t) \tag{2.1}$$

This equation is commonly referred to as *Schrödingers equation* or SGE. The wave function Ψ includes a description of all particles in the system as a function of their coordinates and of time. However, the following work only concerns itself with stationary states, which are solutions of the time-independent SGE, only dependent on spatial coordinates. The Hamiltonian $\hat{H}$ then contains several independent terms which act on Ψ, its expectation value is the energy of the system. For a molecular system of N electrons and M nuclei, the Hamiltonian in atomic units[1] is defined as follows:

$$\hat{H} = \underbrace{-\sum_{i=1}^{N}\frac{1}{2}\nabla_i^2}_{\hat{T}_e} \underbrace{-\sum_{A=1}^{M}\frac{1}{2M_A}\nabla_A^2}_{\hat{T}_n} \underbrace{-\sum_{i=1}^{N}\sum_{A=1}^{M}\frac{Z_A}{r_{i,A}}}_{V_{e,n}} + \underbrace{\sum_{i=1}^{N}\sum_{j>i}^{N}\frac{1}{r_{i,j}}}_{V_{e,e}} + \underbrace{\sum_{A=1}^{M}\sum_{B>A}^{M}\frac{Z_A Z_B}{R_{A,B}}}_{V_{n,n}} \tag{2.2}$$

The first two terms ($\hat{T}_e$ and $\hat{T}_n$) describe the kinetic energy of electrons and nuclei, the third term ($V_{e,n}$) relates to the attraction between them and the last two terms ($V_{e,e}$ and $V_{n,n}$) describe

[1] Atomic units are the mass of an electron m_e, the charge of a proton e, the bohr radius a_0, Hartree-energy E_H, the Planck constant divided by 2π, $\hbar$ for the angular momentum and $\kappa_0 = 4\pi\epsilon_0$ as the permittivity.

the repulsion between electrons and electrons and nuclei and nuclei, respectively. $r_{i,A}$, $r_{i,j}$, and $R_{A,B}$ relate to the inter-particle distance of the interacting particles with lowercase indices $\{i, j\}$ referring to different electrons and uppercase letters $\{A, B\}$ to different nuclei, mathematically understood as $r_{i,j} = |\vec{r}_i - \vec{r}_j|$. M and Z relate to mass and charge of the nuclei.

Equation 2.2 describes the Hamilton operator of a many-body system, which yields the total energy (as the sum of kinetic and potential energy) as expectation value of the system. The problem hereby lies in the correct description of a full many-body wave function. Even with modern computational methods this is not possible for real systems due to the immense amount of variables involved and therefore approximations have to be introduced.
Based on the assumption of nuclei being much heavier and slower than electrons, a change in position of a nucleus can be seen as instantly followed by equilibration of electronic motion. From the perspective of the electrons the nuclei are not moving - in other words their kinetic energy is zero. Following the picture of fixed nuclei, applying this simplification was termed the *clamped nuclei (cn)* approximation. As a result, the repulsive potential $V_{n,n}$ becomes a constant value and the attractive potential $V_{e,n}$ only parametrically depends on the positions of the nuclei, which allows to write an electronic Hamiltonian in the following form:

$$\hat{H}^{\text{elec}}_{\text{cn}} = \hat{T}_e + \hat{V}_{e,e} + \hat{V}_{e,n} \tag{2.3}$$

A nuclear Hamiltonian can be constructed in analogy and describes nuclear motion (such as vibrations or rotations) within the potential obtained from equation 2.3. This approach of decoupling electronic and nuclear motion is one of the fundamental approximations which modern quantum chemistry is built upon and is usually referred to as the Born-Oppenheimer approximation (BOA) [37]. The BOA is also the root of the idea of a potential energy surface (a mathematical representation of the potential energy depending on the nuclear degrees of freedom), which is a key concept within computational chemistry.

The application of the concepts introduced above to a system of chemical interest therefore leads to the problem of solving the electronic SGE[1]:

$$\hat{H}^{\text{elec}}\Phi(\vec{r}, \vec{R}) = E^{\text{elec}}\Phi(\vec{r}, \vec{R})$$

$$with \quad \hat{H}^{\text{elec}} = \underbrace{-\sum_{i=1}^{N} \frac{1}{2}\nabla_i^2}_{\hat{T}_e} \underbrace{-\sum_{i=1}^{N}\sum_{A=1}^{M} \frac{Z_A}{r_{i,A}}}_{V_{e,n}} + \underbrace{\sum_{i=1}^{N}\sum_{j>i}^{N} \frac{1}{r_{i,j}}}_{V_{e,e}} \tag{2.4}$$

As mentioned above, the electronic Hamiltonian only consists of contributions ascribed to the kinetic energy of the electrons, the electron-electron interaction and an electron-nuclei interaction with only a parametric dependence on $\vec{R}$. Instead of the full many-body wave function $\Psi(\vec{r}, \vec{R})$, the electronic Hamiltonian only acts on $\Phi(\vec{r}, \vec{R})$, which is the electronic many-body wavefunction. This wave function can be approximated in a variety of ways[2], one of them is to describe it as a product of single-electron eigenfunctions ψ_i. This is justified by the fact that the Hamiltonian in

[1] The subscript *cn* is dropped in all further derivations

[2] In the *wave function methods* discussed here, the central idea is to improve accuracy by an improvement of the description of the wave function, while the operator $\hat{H}$ is known exactly. The central idea behind it is the *variational principle*, which states that any wavefunction other than the correct one always yields an energy higher or equal to the ground state.

equation 2.4 can be written as a non-interacting term ($\hat{T}_{e_i}$ and $V_{e_i,n}$) and a coupling term V_{e_i,e_j}. The non-interacting term is a sum of single-electron Hamiltonians $\sum_i \hat{h}_i + V_{e_i,e_j}$, consisting of a set of unique operators h_i for each electron. Therefore the electronic wave function $\Phi(\vec{r},\vec{R})$ becomes:

$$\Phi(\vec{r},\vec{R}) = \prod_{i}^{N} \psi_i(\vec{r}_i) \tag{2.5}$$

This ansatz is called a *Hartree product* (HP) and constitutes the simplest approximation of the wave function. However, the way how $\Phi(\vec{r},\vec{R})$ is expressed in equation 2.5 causes two inherent flaws in the description of electrons: it does not respect the requirement of antisymmetry due to exchange of two electrons and their inherent indistinguishability. The solution to this problem was introduced by Slater in form of a determinental ansatz for the wave function. The so-called Slater determinant Φ_0^{SD} is formed by constructing the wave function based on the lowest occupied spin orbitals:

$$\Phi_0^{\mathrm{SD}}(\vec{r}) = \frac{1}{\sqrt{N!}} \begin{vmatrix} \psi_i(\vec{r}_1) & \psi_j(\vec{r}_1) & \cdots & \psi_N(\vec{r}_1) \\ \psi_i(\vec{r}_2) & \psi_j(\vec{r}_2) & \cdots & \psi_N(\vec{r}_2) \\ \vdots & \vdots & & \vdots \\ \psi_i(\vec{r}_N) & \psi_j(\vec{r}_N) & \cdots & \psi_N(\vec{r}_N) \end{vmatrix} \tag{2.6}$$

The resulting wave function satisfies both the antisymmetry requirement due to exchange of electrons with each other (by changing the sign of the determinant if columns are exchanged with each other) and the requirement for any two electrons to always differ in their quantum numbers (by resulting in 0 for the determinant if two columns (:= spin orbitals[1]) are equal in the matrix).

The one-electron functions ψ_i can be expressed in a well-known analytical form[2], which is, however, not easily evaluated mathematically. Fortunately a variety of approximations using analytically more accessible functions in approximation to the original form were developed. Many of them are based on a linear combination of functions (often Gaussians), which has to obey the physical boundary conditions. This way of approximating a wave function representation is called a *basis set expansion*. The one-electron function ψ_i can then be represented by:

$$\psi_i(\vec{r}) = \sum_{\nu=1}^{K} c_{\nu i}\phi_\nu(\vec{r}) \tag{2.7}$$

Where ϕ_ν is called a *basis function*, which is used to approximate the behavior of the real wave function. The value K specifies how many functions are used in the approximation, adding accuracy but also computational cost with each additional step. The coefficients $c_{\nu i}$ are the variables being optimized during a calculation and specify the contribution of this one basis function to the overall wave function.

A very well known method which uses these ideas and approximations is termed the *Hartree-Fock* (HF) method and relies on solving the electronic SGE on the basis of one Slater-determinant wave functions. By calculating the expectation value of the Hamiltonian from equation 2.4 with the Slater determinant from equation 2.6, three terms arise:

[1] A spin function is a wave function with a spatial part multiplied by a spin part of either two orientations, therefore for each spatial one-electron function $\psi_i(\vec{r})$ one can form two spin functions $\psi_i^{\alpha}(\vec{r})$ and $\psi_i^{\beta}(\vec{r})$

[2] For a detailed derivation consult [34]

$$\langle \Phi_0^{\mathrm{SD}} | \hat{H}^{\mathrm{elec}} | \Phi_0^{\mathrm{SD}} \rangle = \sum_{i=1}^{N} \langle \psi_i | -\frac{1}{2}\nabla_i^2 - \sum_{A=1}^{M} \frac{Z_A}{r_{i,A}} | \psi_i \rangle + \sum_{i=1}^{N}\sum_{j>i}^{N} \left(\langle \psi_i \psi_i | \, r_{12}^{-1} \, | \psi_j \psi_j \rangle - \langle \psi_i \psi_j | \, r_{12}^{-1} \, | \psi_j \psi_i \rangle \right) \tag{2.8}$$

The two electron term $V_{e,e}$ was rewritten to two different contributions, namely the Coulomb Integral $\hat{J} = \langle \psi_i \psi_i | \, r_{12}^{-1} \, | \psi_j \psi_j \rangle$ and the exchange integral $\hat{K} = \langle \psi_i \psi_j | \, r_{12}^{-1} \, | \psi_j \psi_i \rangle$. This formulation led to the interpretation of each electron j in the system interacting with the mean potential $\sum_{i \neq j} (\hat{J}_i + \hat{K}_i)$ of the (N-1) other electrons. Of physical importance is the fact, that $\hat{K}_{ii} = \hat{J}_{ii}$, therefore the formulation corrects itself for the initial error due to self-interaction of an electron with itself if $i = j$. $\{i, j\}$ denote indices of the orbitals considered, whereas $\{1, 2\}$ relate to the electrons.

HF has nowadays become the foundation of other more sophisticated approaches based on wave function theory which additionally consider a quantity called the correlation energy (the difference between the true value of the energy and the energy obtained by HF). These methods are called *post-HF* methods and typically improve the wave function by linearly combining more and more Slater determinants of different single particle states with Φ_0^{SD} and by varying their influence on the wave function through the introduction of coefficients for each determinant. These linear combinations of Slater determinants can be seen as excited states with respect to HF. Obviously, every improvement of the wave function adds variables to the solution of the SGE, which makes post-HF methods computationally very demanding. By carefully truncating the expansion after only few additional excited determinants Φ_i^{SD}, it is possible to recover the correlation energy almost entirely (depending on the system under study and the method chosen) with still manageable computational effort. One such technique that has been used in this thesis is termed *Approximate Coupled Cluster Doubles* (CC2) [38] and accounts for all singly and a part of doubly excited determinants. For a detailed explanation of the method see Levine [32].

2.2 Density Functional Theory

A completely different approach is density functional theory (DFT), the principal technique of this work. The formal foundation for DFT was laid by Hohenberg and Kohn [39] in the form of two theorems, the first of which states that there is a direct and invertible relation between the ground state electron density $\rho_0(\vec{r})$ and the external potential describing the system[1], which then allows the construction of a Hamiltonian $\hat{H}[\rho]$, making the energy a direct functional of the electron density ($E_0 = E_0[\rho_0(\vec{r})]$). Therefore it is possible to replace the high-dimensional wave function introduced before by the electron density, a function of three variables, as the principle quantity.

$$E_0[\rho_0(\vec{r})] = \underbrace{\int \rho_0(\vec{r}) V_{n,e} d\vec{r}}_{\mathrm{system-dependent}} + \underbrace{T[\rho_0(\vec{r})] + V_{e,e}[\rho_0(\vec{r})]}_{\mathrm{universally\ valid} \; := \; F_{\mathrm{HK}}[\rho_0(\vec{r})]} \tag{2.9}$$

The second term on the right hand side of equation 2.9 is the functional predicted by Hohenberg and Kohn ($F_{\mathrm{HK}}[\rho_0(\vec{r})]$) and is fully independent of the system which it is applied to. It consists of the kinetic energy $T[\rho_0(\vec{r})]$ and the electron-electron interaction $V_{e,e}[\rho_0(\vec{r})]$. The latter one can be

[1] Such a density connected with a potential V_{ext} is called *V-representable*.

partly represented by the Hartree term $J[\rho_0(\vec{r})]$ (see equation 2.8) of the interaction of two charged particles and an additional term E_{ncl}, which contains all non-classical interactions.

$$E_0[\rho_0(\vec{r})] = \int \rho_0(\vec{r}) V_{n,e} d\vec{r} + T[\rho_0(\vec{r})] + J[\rho_0(\vec{r})] + E_{\mathrm{ncl}}[\rho_0(\vec{r})] \tag{2.10}$$

The second Hohenberg-Kohn theorem connects the previous findings with the fact that $F_{\mathrm{HK}}[\rho_0(\vec{r})]$ only yields the correct ground-state energy if the associated density is the correct ground state density. As a consequence of this the variational principle can be applied, which states that for every density other than the ground state density, the energy value obtained by application of the Hohenberg-Kohn functional is higher. This assumption is only valid under the premise of non-degenerate ground states and following the boundary condition of the density of $\rho(\vec{r}) \geq 0$ and $\int \rho(\vec{r}) d\vec{r} = N$.

Therefore density functional theory in principle allows to calculate the correct ground state properties of any system if a way to mathematically express the unknown terms in equation 2.10 can be found. A solution to this problem was suggested by Kohn and Sham [40] and their method became the standard approach to tackle the problem. Their ansatz assumed that the largest contribution of the kinetic energy contained within the kinetic energy operator $T[\rho_0(\vec{r})]$ can be approximated by calculating the kinetic energy of a reference system of non-interacting particles given by a single Slater determinant as discussed above. The remaining contribution in energy can then be subsummed together with the term $E_{ncl}[\rho_0(\vec{r})]$ containing all non-classical interactions and is denoted as the exchange-correlation term $E_{xc}[\rho_0(\vec{r})]$. If $T_s[\rho(\vec{r})]$ is defined as the kinetic energy operator of the reference system (the index s designating the reference system), then the KS-energy is given by (with $V_{\mathrm{ext}}(\vec{r})$ meaning the external potential $V_{n,e}$):

$$E[\rho(\vec{r})] = T_s[\rho(\vec{r})] + J[\rho(\vec{r})] + E_{xc}[\rho(\vec{r})] + E_{N,e}[\rho(\vec{r})] \tag{2.11}$$

$$\text{with} \quad T_s[\rho(\vec{r})] = -\frac{1}{2} \sum_{i=1}^{N} \left\langle \varphi_i \middle| \nabla^2 + V_{\mathrm{ext}}(\vec{r}_i) \middle| \varphi_i \right\rangle \tag{2.12}$$

$$\text{and} \quad \rho_s(\vec{r}) = \sum_i^N \sum_s |\varphi_i(\vec{r}, s)|^2 = \rho_0(\vec{r}) \tag{2.13}$$

The only term which is not familiar from wave function methods is E_{xc}, the *exchange-correlation energy*, which basically holds all the additional contributions which arise from the nonclassical interaction of the electrons with each other. Up to now, KS-DFT is still without any simplification and therefore theoretically leads to the exact solution of the given system. However, the exact form of E_{xc} is unknown and in the years since the initial proposal of KS-DFT many different approaches on how to approximate it were developed, the three major ones being outlined in the following paragraphs.

Local Density Approximation LDA The Local Density Approximation (LDA) was the first attempt to model the unknown energy term E_{xc} under the assumption of it only being dependent on the density ρ_0 at a certain point in space. This idea was already mentioned in the paper of Kohn and Sham [40] and relies on the model of the electrons being distributed in a uniform electron gas with a constant charged background.

$$E_{\mathrm{xc}}^{\mathrm{LDA}}[\rho(\vec{r})] = \int \rho(\vec{r}) \epsilon_{xc}(\rho(\vec{r})) d\vec{r} \tag{2.14}$$

$\epsilon_{\mathrm{xc}}(\rho(\vec{r}))$ is the exchange-correlation energy per particle, thus the overall $E_{\mathrm{xc}}^{\mathrm{LDA}}$ is an average weighted energy. This model (as might be intuitively expected) performs very well for materials with

only little variation in the electron distribution such as alkali metals. However, for the description of molecules and transition metals, which are marked by rapid changes in their density distribution, this model has its limitations [35, 41].

Generalized Gradient Approximation GGA The GGA approach not only relates the E_{xc} to the density but additionally introduces the gradient of the density $\nabla\rho(\vec{r})$ at this point as parameter to the functional. This is done by using the LDA as the first term of a Taylor expansion, the following terms then naturally involve derivatives and therefore the gradient of the given density.

$$E_{\mathrm{xc}}^{\mathrm{GGA}}[\rho_\alpha(\vec{r}),\rho_\beta(\vec{r})] = \int f(\rho_\alpha,\rho_\beta,\nabla\rho_\alpha,\nabla\rho_\beta)d(\vec{r}) \tag{2.15}$$

By introducing the density gradient into the functional, some physically imposed boundary conditions are lost. The straightforward approach is to simply discard the terms which do not obey the boundary conditions, leading to a physically meaningful functional which produces better results compared to the LDA approach [35, 42]. Nevertheless, GGA and also LDA functionals suffer from two major problems: By including the Coulomb integral from HF theory (see equation 2.8), electrons are allowed to interact with themselves. This self-interaction error is cancelled within the formulation of the HF approach but can not be exactly accounted for within the approximated E_{xc}. The second problem associated with the given forms is that neither LDA nor GGA account for the correct asymptotic long-range behavior of the E_{xc}. A well-known GGA functional is PBE [42], which was also used in this work.

Hybrid-Functionals Like the name already suggests, these exchange-correlation functionals, include contributions from different theories. They are based on LDA or GGA functionals and include a specific amount of exact exchange from the Hartree-Fock theory in order to counteract the inherent self-interaction error which arises from the use of LDA or GGA functionals. The intermix ratio of the different contributions follows two different philosophies, one of which aims to create the most accurate results within the limit of physical constraints (such as the PBE0 [43, 44] functional), whereas the other approach aims to reproduce experimental values by empirically fitting the parameters without strictly following physical grounds (the most prominent representative being the B3-LYP functional [45]). The comparatively high accuracy obtained with these functionals made them mark the dawn of DFT for application to chemical problems and became the de-facto standard for a variety of systems [35, 41].

The exchange-correlation term in the simulations of this work employ a GGA-functional for surface-adsorbed systems and hybrid functionals for gas phase simulations. The GGA functional in the description of the systems involving solid state matter was chosen because the corrections introduced in hybrid functionals improve the description of molecules, but are less successful in reproducing the correct band structure and other properties in solid state systems [41] compared to LDA and GGA. DFT was chosen because it is less computationally demanding compared to more accurate wave-function methods whilst still including exchange and correlation effects of the electrons and therefore correctly describing the nature of the chemical bonds. Wave function methods are less suited to describe the special bonding situation in solids and, most importantly, would also be too demanding in terms of computational cost.
One serious disadvantage in using DFT with current semi-local or hybrid exchange-correlation functionals consists of the problem that weak long-range interactions such as van-der-Waals forces are not sufficiently being accounted for by standard DFT methodology. Since the given problem requires the inclusion of dispersive interactions due to the interaction of the adsorbate with the metal surface, the following chapter briefly introduces approaches which address this issue.

2.3 Van-der-Waals interaction in DFT

Current functionals, such as those introduced above, perform very well when describing the covalent bonding inside a molecule, however when it comes to dispersive long-range interactions one has to go beyond local and semi-local approximations to exchange and correlation. In a generalized form, the non-covalent interactions between particles can be separated into four categories, namely interactions between static multipoles, between static and induced multipoles, the short range-repulsion due to the Pauli principle (which is already accounted for in the exchange-correlation term in DFT) and finally the interaction between induced and fluctuating multipoles, giving rise to what is commonly referred to as dispersion or van-der-Waals interaction. The leading term of a power series describing the mutual polarization of atoms with respect to their interatomic distance has a R^{-6} dependence. This long-range asymptotic behavior is crucial in describing for example the interaction of large organic molecules with a metal surface. The main flaw within the above mentioned functionals is their inherent local description of exchange and correlation, thus not including a term which accounts for the R^{-6} behavior at long distances while still including some terms describing dipole-interactions at short distances. To overcome this deficiency, two ways of supplementing the missing interaction were developed, namely either explicitly constructing long-range correlation within the exchange-correlation functional (a prominent approach here would be vdW-DF [46]), or by adding an empirical correction with an interatomic pairwise potential. Within this work, the latter approach was used. The global energy contribution including dispersive interactions is approximated as:

$$E_{\mathrm{tot}} = E_{\mathrm{DFT}} - \sum_{A,B} \frac{C_6^{\mathrm{AB}}}{R_{\mathrm{AB}}^6} \tag{2.16}$$

In equation 2.16 C_6^{AB} designates a constant dispersion coefficient which depends on the atom pair A and B. However, at very small distances of the nuclei, the term diverges, additionally at short distances the local description of the DFT functional sets in, which leads to double-counting of contributions. To counteract this behavior a damping function $f(r_{cut}, A, B)$ is introduced which sets in at an empirically defined cutoff r_{cut}, specifying the onset of the damping. Equation 2.16 thus becomes

$$E_{\mathrm{tot}} = E_{\mathrm{DFT}} - \sum_{A,B} f(r_{cut}, A, B) \frac{C_6^{\mathrm{AB}}}{R_{\mathrm{AB}}^6} \tag{2.17}$$

Different models on how to efficiently calculate the C_6^{AB} parameters of this correction scheme were proposed by different groups [47]. The most well-known are the schemes by Grimme [48] and the approach used in this work, developed by Tkatchenko and Scheffler [49] and further improved by Ruiz et. al. [50] to include the collective response within the substrate (screening) that reduces the van-der-Waals interaction and leads to smaller C_6^{AB} coefficients and smaller van-der-Waals radii R_{vdW} for the metal atoms, based on the underlying theory published by Zaremba and Kohn [51].

The method of Tkatchenko and Scheffler takes the initially introduced approach to calculate the pairwise potential via C_6^{AB} coefficients as shown in equation 2.17, but additionally scales the C_6^{AB} parameters with relation to their effective Hirshfeld-volume [52] as obtained from the DFT calculation, therefore accounting for the chemical environment of each atom. The effective Hirshfeld volume of an atom A inside the whole system of particles is calculated as shown in equation 2.18.

$$\rho_A(\vec{r}) = \rho(\vec{r}) \frac{\rho_A^0(\vec{r})}{\sum\limits_i \rho_i^0(\vec{r})} \tag{2.18}$$

$\rho_A(\vec{r})$ is the density of the atom A in the Hirshfeld-partitioning scheme, $\rho_A^0(\vec{r})$ the density of the isolated atom, and $\sum_i \rho_i^0(\vec{r})$ is the sum of atomic densities of all atoms at their positions within the simulated system (for this reason also referred to as *promolecule density*).

There are much more involved methods to adress the dispersive interaction known to date, with the ones chosen in this work representing the most balanced approach in terms of accuracy and computational tractability. Other approaches (such as vdW-DF mentioned above) calculate the dispersive interaction within the description of the exchange-correlation functional or rely on more accurate contributions as calculated from wave function methods, which for the better part require the same if not more computational effort as the underlying DFT calculation [47]. Since this work aims (as will be discussed in Chapter 3) at developing a simplified embedding model to cut down on computational cost and at the same time properly account for van-der-Waals interactions, these were not the methods of choice.

2.4 Density Functional Tight Binding

Density functional theory has become one of the major methods used in theoretical chemistry nowadays, because it combines sufficiently high accuracy with modest amount of computational effort. In this section a method will be introduced which is a *tight-binding* approach *derived from DFT* which requires only very *few empirical parameters*, called Density Functional Tight Binding (DFTB). Despite the computational efficiency of DFT, sometimes there is the need for computationally even less demanding methods - for example in applications like computational screening approaches or preoptimizations of large systems. What makes DFTB special in this regard is the fact that the parameters and formalism contained within are all based on DFT itself [53, 54].

Tight binding approaches in physics are conceptually similar to an LCAO ansatz, such as Hückel theory for π-extended systems in chemistry. In both cases one only accounts for the interactions between nearest-neighbor atoms. The concept of the application of this theory to electronic structure was first published by Slater and Koster [55] and built around the ansatz of approximating the wave function by a linear combination of atomic orbitals in conjunction with a simplified Hamiltonian which only depends on internuclear distances. The problem can then be reduced to a set of secular equations which can be evaluated to yield the energy eigenvalues. The basic principle is still the same today, but was improved and extended in a variety of ways to encompass a well-defined set of parameters [53].

DFTB is derived from the Kohn-Sham DFT perspective and the fact that the functional $E[\rho(\vec{r})]$ (see eqn. 2.11) is variational with respect to the density $\rho(\vec{r})$, which in turn is approximated by an expansion within a basis as explained in section 2.2. Following the ansatz of Foulkes and Haydock [56], we formulate the functional with respect to $\rho_0(\vec{r})+\delta\rho(\vec{r})$ (introducing a small fluctuation $\delta\rho(\vec{r})$) and expand the energy functional around ρ_0 to the second order in the perturbation $\delta\rho$, which results in the following equations [54, 57, 58]:

$$E[\delta\rho] \approx \overbrace{\sum_a f_a \langle\varphi_a| -\frac{1}{2}\nabla^2 \; + \; V_{\text{ext}} \; + \; V_H[\rho_0] \; + \; V_{\text{xc}}[\rho_0] \,|\varphi_a\rangle}^{E_{\text{BS}}}$$
$$\underbrace{+\frac{1}{2}\int\int \left(\frac{\delta^2 E_{\text{xc}}[\rho_0]}{\delta\rho\delta\rho'} \; + \; \frac{1}{|\vec{r}-\vec{r}'|}\right) \delta\rho\delta\rho' \; d\vec{r}d\vec{r}'}_{E_{\text{coul}}}$$
$$\underbrace{-\frac{1}{2}\int V_H[\rho_0](\vec{r})\rho_0(\vec{r}) \; d\vec{r} \; + \; E_{\text{xc}}[\rho_0] \; + \; E_{n,n} \; - \; \int V_{\text{xc}}[\rho_0](\vec{r})\rho_0(\vec{r}) \; d\vec{r}}_{E_{\text{rep}}} \tag{2.19}$$

$f_a \in [0,2]$ designates the occupation of the single-particle state φ_a which stems from the basis expansion of $\rho(\vec{r})$ as it is done in KS-DFT. V_H is the same as $J[\rho]$ in DFT-terminology. ρ_0 designates the ground state density of a collection of free and neutral atoms (as a reference), ρ and ρ' are two different densities in pairwise interaction. $\vec{r}$ and $\vec{r}'$ are their associated position vectors.
The expression in equation 2.19 can be separated into 3 terms: the *band structure term* E_{BS}, the *charge fluctuation term* E_{coul} containing not only coulombic interaction but also exchange interaction, and the *repulsive term* E_{rep}, containing ion-ion interaction and the exchange-correlation part. Due to approximations used in DFTB theory[1], these three terms can be approximated in a numerically accessible form.

The band structure term is parametrized by the results taken from an initial DFT calculation: The diagonal Hamiltonian elements $H^0_{\mu\mu}$ are taken as the eigenvalues of free atoms and the off-diagonal elements $H^0_{\mu\nu}$ calculated within a two-center approximation [57].

$$E_{BS} = \sum_a f_a \sum_{\mu\nu} c^{a*}_\mu c^a_\nu H^0_{\mu\nu}$$
$$\text{with}: \;\; H^0_{\mu\nu} = \begin{cases} \epsilon^{\text{free atom}}_\mu & \text{if } \mu = \nu \\ \langle\varphi_\mu| \hat{T} + V_{\text{eff}}[\rho^0_\alpha + \rho^0_\beta] \,|\varphi_\nu\rangle & \mu \in \alpha, \nu \in \beta \end{cases} \tag{2.20}$$

The coefficients c^{a*}_μ and c^a_ν are those associated with the minimal basis functions φ_μ and φ_ν, respectively. $\hat{T}$ is the kinetic energy operator, and V_{eff} is an effective potential including V_H, J, and V_{xc}. ρ^0_α and ρ^0_β are the densities of the neutral free atoms. The values of $H^0_{\mu\nu}$ and also the overlap integrals $S_{\mu\nu} = \langle\varphi_\mu|\varphi_\nu\rangle$ are collected in so-called *Slater-Koster tables* and serve as primary input parameters in DFTB calculations.

The charge fluctuation term can be approximated in an electrostatic manner depending on a charge difference Δq [2] and in terms of the Hubbard U (difference in energy between ionization energy and electron affinity) by taking advantage of an elegant relation between basic atomic physics, electrostatics, and symmetry [54].

$$E_{\text{coul}}[\Delta q_I, \Delta q_J] = \frac{1}{2}\sum_{\text{IJ}} \Upsilon_{\text{IJ}}(R_{\text{IJ}})\Delta q_I \Delta q_J \quad \text{with} \quad \Upsilon_{\text{IJ}} = \begin{cases} U & , I = J \\ \frac{\text{erf}(C_{\text{IJ}} R_{\text{IJ}})}{R_{\text{IJ}}} & , I \neq J \end{cases} \tag{2.21}$$

[1] The detailed derivations are not reproduced here but well-document in several reviews on the topic [53, 54, 57–59].
[2] These are approximated by Mulliken orbital population analysis [60].

Because of the localized basis sets used the integral part of the repulsive term can be interpreted on a per-atom basis, reducing the integral over space to a mere sum of atom pairs only depending on atomic numbers and their respective distance, similar to the ion-ion interaction which only depends on the valence number Z^V. Hence, E_{rep} reduces to pairwise evaluated functions $V_{\mathrm{rep}}^{\mathrm{IJ}}$ which are fitted to DFT results with polynomial series or splines. This approach allows to avoid the problem of treating the complicated contributions, such as exchange and correlation, within the repulsive potential and can therefore be regarded as the DFTB-equivalent of the E_{xc} term in DFT [53].

$$E_{\mathrm{rep}} = \sum_{\mathrm{IJ}} V_{\mathrm{rep}}^{\mathrm{IJ}}(R_{\mathrm{IJ}}) \tag{2.22}$$

The final energy expression follows by combination of equations 2.20, 2.21, and 2.22:

$$E = \sum_a f_a \sum_{\mu\nu} c_\mu^{a*} c_\nu^a \langle \varphi_\mu | H^0 | \varphi_\nu \rangle + \frac{1}{2} \sum_{\mathrm{IJ}} \Upsilon_{\mathrm{IJ}}(R_{\mathrm{IJ}}) \Delta q_I \Delta q_J + \sum_{IJ} V_{rep}^{\mathrm{IJ}}(R_{\mathrm{IJ}}) \tag{2.23}$$

In the context of an LCAO ansatz, this energy can be minimized by variation of the left term in equation 2.24, which yields a system of secular equations then to be solved to obtain the set of eigenvalues.

$$\delta(E - \sum_a \epsilon_a \langle \varphi_a | \varphi_a \rangle) \quad \rightarrow \quad \sum_\nu c_\nu^a (H_{\mu\nu} - \epsilon_a S_{\mu\nu}) = 0 \tag{2.24}$$

$$H_{\mu\nu} = H_{\mu\nu}^0 + \frac{1}{2}(\in_I + \in_J) \tag{2.25}$$

Here $\in_I$ and $\in_J$ designate the electrostatic potential on atom I and J, respectively.
Equations 2.24 and 2.25 have to be solved self-consistently similarly to DFT: Starting from an initial guess of the values of $\{\Delta q\}$, the electrostatic potential and therefore the Hamiltonian $H_{\mu\nu}$ is constructed, followed by evaluation of equation 2.24, which in turn returns the expansion coefficient c_ν^a, leading to a new population value. Then the cycle is repeated until convergence is achieved.
A description of the parameters for the system treated in this work and the DFTB-Code Hotbit [54] is presented in the Appendix A.2.

2.5 Tersoff-Hamann Simulation

The first theoretical approach in predicting and reproducing STM topographs from the theoretical point of view was developed by Tersoff and Hamann [61]. Their approach was based on earlier works which describe the tunneling of electrons between two conducting materials according to Fermi's golden rule [62]. The tunneling current I is given by:

$$I = \frac{2\pi e}{\hbar} \sum_{\mu\nu} f(E_\mu)[1 - f(E_\nu + eV)]|M_{\mu\nu}|^2 \, \delta(E_\mu - E_\nu) \tag{2.26}$$

Here $f(E)$ is the Fermi-Dirac distribution, e is the electron charge, V corresponds to the applied voltage bias. The transition matrix element $M_{\mu\nu}$ describes the tunneling propability between the wave function ψ_μ of the surface and ψ_ν of the STM tip. Their respective energies $E_{\mu,\nu}$ relate to the non-tunneling case.

Typically STM experiments are conducted at low temperatures and low voltages, in which case equation 2.26 can be simplified to [61]:

$$I = \frac{2\pi}{\hbar} e^2 V \sum_{\mu\nu} |M_{\mu\nu}|^2 \ \delta(E_\nu - E_F)\delta(E_\mu - E_F) \tag{2.27}$$

The central assumption within the approach presented by Tersoff and Hamann was the idea of neglecting the exact influence of the wave function of the tip. The matrix element $M_{\mu\nu}$ is determined as:

$$M_{\mu\nu} = \frac{\hbar^2}{2m} \int (\psi_\mu^* \nabla \psi_\nu - \psi_\nu \nabla \psi_\mu^*) d\vec{S} \tag{2.28}$$

$\int d\vec{S}$ is the integral over all space between the tip and the surface.
If the tip is now assumed as a spherically symmetric potential (like a s orbital), then the current in equation 2.27 becomes essentially only dependent on the wave function of the surface and therefore simplifies to:

$$I \propto \sum_{\nu}^{eV} |\psi_\nu(r_0)|^2 \ \delta(E_\nu - E_F) \tag{2.29}$$

Here, the expression $\sum_\nu^{eV} |\psi_\nu(r_0)|^2$ equals to the local density of states (LDOS). Of course the approximation of neglecting the electronic structure of the tip is severe and following this initial approach of Tersoff and Hamann, more complex methods were developed to account for the influence of the tip wave function. Nevertheless, the simple model presented here is in many cases a good approximation and compares well with experiments.

Chapter 3

Implementation of a van-der-Waals embedding scheme

The goal of this work is to study the interplay of an organic adsorbate with an inorganic (metal) surface. Long-range contributions to the bonding situation such as weak dispersive interactions are of utmost importance for such systems [63]. There is a plethora of different approaches known to date to tackle exactly this problem, namely the description of dispersive interactions within the framework of DFT theory [47]. Often enough, large molecular adsorbates featuring interesting chemical functionalities and electronic properties are studied by experimental means, whereas the theoretical treatment of the geometry and adsorption energy unfortunately encompasses a considerable computational effort and therefore complicates the study of these systems in a systematical manner. The major contribution in terms of computational expense can usually be ascribed to finding the correct adsorption geometry within the huge parameter space spanned, encompassing the internal degrees of freedom of adsorbate and surface. It is therefore of great importance and interest to develop models which can efficiently search for adsorption geometries of different minima on the potential energy surface - in other words an efficient way of computational screening. The here presented embedding approach is one possible way to enable more efficient geometrical screening of large organic adsorbates on metal surfaces.

3.1 The embedding approach

The molecule of interest in this work, retinoic acid, is a medium-sized molecule of 50 atoms, which from a computational point of view is nowadays in principle addressable with a variety of computational schemes such as DFT or wave function based methods, as can be seen from many theoretical studies published about the photochemistry and switching behavior in the gas phase or inside biological systems [16, 17, 64, 65]. This work adresses the adsorption and relevant effects on the electronic structure due to interaction with a Au(111) surface and the different possible geometric and magnetic states that arise as a consequence. This situation requires to explicitly account for the Au surface in a quantum-chemical calculation, which significantly increases the system size to be studied, but lies within an area where - despite becoming computationally challenging - DFT can still be applied. Furthermore, not only the global minimum of the potential energy surface is of interest to the present study, but also several local minima which would in turn explain the difference in the protrusions observed in Figure 1.1. Due to the large number of internal degrees of freedom in the retinoic acid molecule, many local minima are present. Hence, the search for those which best describe the experimental observation involves many calculations and therefore this system is a prime

example of a computationally challenging adsorbate-substrate system which would profit immensely from a speedup in the determination of the on-surface geometry.

The current state-of-the-art of simulating adsorbates on metal surfaces is based on Density-Functional-Approximations that include the description of dispersion interactions. This significantly improves the description of adsorbate structure and energetics when compared to adsorbate geometries obtained from plain LDA or GGA approximations [63, 66]. The most commonly used method of including dispersion interactions is the use of an empirical correction by addition of a pairwise-atomic van-der-Waals potential (see section 2.3). The most recent of such DFT-D approximations (DFT+D3 [48] and DFT+vdW^{surf} [50]) yield an accurate description of geometry and energetics as has been shown for a variety of different organic adsorbates on metal surfaces [50, 63, 67, 68]. This increase in accuracy comes for almost negligible additional computational cost. Nevertheless, the description of systems, such as ReA adsorbed to Au(111) becomes infeasible already on the level of pure DFT, due to the immense amount of substrate atoms that have to be accounted for. In order to achieve a converged description of geometry and energetics one typically models the surface by including a minimum of 4 layers of substrate. In the case of ReA on Au(111) in a (3x7) unit cell this would amount to 134 atoms and 6800 electrons. Even with current computational infrastructure a necessary extensive geometry search of the adsorbate structure would be unfeasible and undesirable. Just reducing the necessary amount of substrate by one layer can already reduce the number of electrons in the system by almost 25%. Here the fact can be utilized that for molecules, which mainly physisorb on the surface or which only show weak chemical interaction, the DFT contribution to structure and energetics converges very quickly with the number of substrate layers, whereas the dispersion correction, by construction, shows a slow long-range decay, which necessitates the inclusion of many more substrate layers.

With this thought in mind, an embedding model was developed and implemented in which the number of substrate layers treated explicitly with DFT is reduced to the minimally necessary amount, while the dispersion correction is included for an extensive substrate. In this way the differing convergence behavior of the two contributions, DFT and dispersion interactions, is optimally used to reduce computational cost with hopefully minimal loss in accuracy on the adsorbate structure. As shown in Figure 3.1 the explicitly treated DFT slab is therefore 'embedded' in a van-der-Waals continuum that properly accounts for the long-range interaction of the adsorbate with the extended substrate. The implementation was realized as a part of ASE [69] [1]: The Atomic Simulation Environment is a python-based open-source software package, which provides a unified interface to access different quantum chemistry packages through so-called `calculators`. It combines therefore the advantage of python-based scripting with the numerical efficiency of quantum chemistry software. Additionally

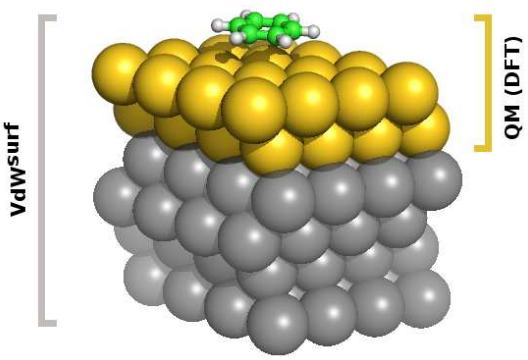

Figure 3.1: *Schematic illustration of the embedding scheme implemented in this work. The adsorbate and a small number of metal layers are simulated within the scope of quantum mechanics (DFT). The whole system is then embedded in a description of van-der-Waals interactions, relying on the* vdW^{surf} *method [50] as discussed in section 2.3, including more metal layers and therefore describing long-range influences that are not present in current DFT approximations.*

[1] Atomic Simulation Environment, freely available from https://wiki.fysik.dtu.dk/ase/

it includes a feature-rich toolbox which allows creation, manipulation, and analysis of the geometries calculated within in a variety of ways.
Two new calculators were incorporated into ASE, one of which is a very generic *QM/MM*-module[1], which can split an initial geometry into different subunits (e.g., the adsorbate and the surface) in order to use the ASE-interface to any external quantum chemistry code to calculate the total energy and forces. Contributions to the total energy and the forces of each atom of every fragment are then summed up and evaluated by the QMMM module. Also, modifications to the whole system such as in the case of geometry optimizations are entirely left to ASE and the quantum chemistry codes are only used for calculating the energy and force contributions of a single geometry. In order to add flexibility to the module, it was designed to support an arbitrary number of possible fragments, which do not have to be contiguous in a chemical sense and are allowed to overlap. ASE already contains a variety of interfaces to different quantum chemistry codes, however the desired DFT-dispersion correction scheme was not available. Therefore an already existing FORTRAN-module, implemented in the CASTEP code [70, 71], was adapted and interfaced with ASE via f2py [72], which allows to keep computational efficiency of numerical routines written in FORTRAN and the flexibility of data processing within python. In order to account for the change in chemical environment, the C_6^{AB} coefficients in the dispersion correction scheme vdW$^{\text{surf}}$ have to be dynamically rescaled (see section 2.3 on van-der-Waals corrections in DFT). This was done by adapting the DFT-code interfaces of FHI-AIMS [73] and CASTEP [70] to provide a value of the Hirshfeld-partitioning ratio [52] for each atom. The embedding module then mediates the data transfer between the DFT software and the dispersion correction module (for atoms not lying within the area explicitly treated by the DFT code, the C_6^{AB} coefficients are not rescaled).

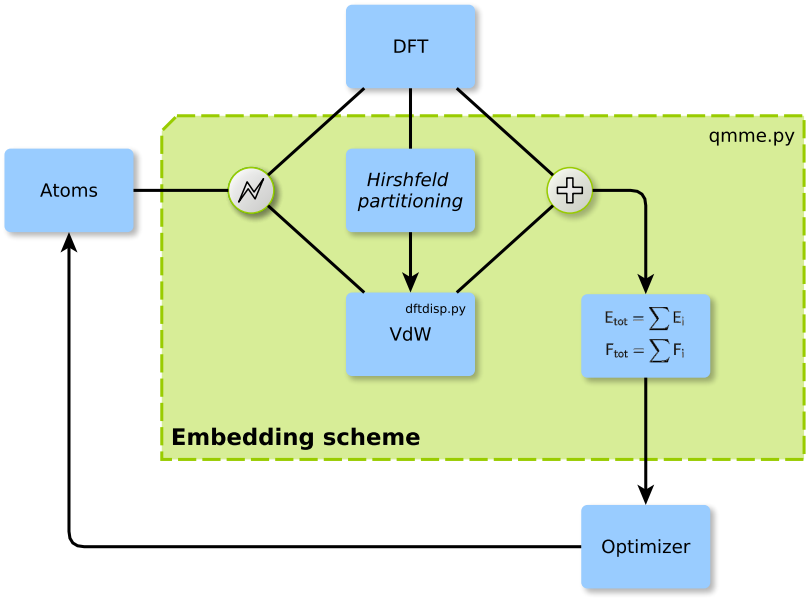

Scheme 3.1: *Schematic workflow of the embedding scheme implementation. A chosen initial geometry is split into an arbitrary number of desired parts, which are then used as the input geometry for a quantum chemistry code accessible from ASE. Since the QMMM module is built upon the calculator class within ASE, it can be used like any other quantum chemistry code within ASE and therefore geometry optimizations as well as single-point calculations are available. The parts marked in green were newly implemented during this thesis.*

[1] The module is rather a very generic embedding approach, however the principal idea of combining different levels of theory even with different software is commonly termed QM/MM.

The workflow diagram in Scheme 3.1 depicts the process of a geometry optimization in the implemented embedding scheme. The `Atoms` object (which within ASE holds the geometry and all the molecular properties of the observed system) is partitioned into two or more specified fragments, each one representing a new `Atoms` object, whose properties are then in turn computed by the assigned `calculator`. Since the `calculator` evaluating the vdW^{surf} dispersion correction requires the input of scaling parameters, the embedding model first runs the quantum chemical software codes which are capable of providing a value for the Hirshfeld-partitioning ratio in order to dynamically adapt the C_6^{AB} coefficients, whereas the rescaling due to screening effects [50] needs to be manually provided. Finally, the total energies of each system as well as the force constants of each atom are summed up, the chosen optimizer algorithm within ASE evaluates if the predefined convergence criterion was reached and based on this result the optimization is finished or the geometry of the `Atoms` object is modified and the process restarted.

3.2 Convergence Tests

The newly implemented embedding scheme was developed with the goal of simplifying the calculation by treating only a small part of the system explicitly with DFT. It is therefore of interest how well the embedding model performs in dependence of the number of explicitly treated metal layers. In order to evaluate this property, two metal-adsorbate systems of benzene (adsorbed on Au(111) and on Pt(111)) were simulated by variation of the number of layers in the DFT and van-der-Waals regimes, respectively. These two systems represent two limiting cases, namely a molecule dominantly bound by van-der-Waals interactions (Au) and a molecule dominantly bound by covalent interactions (Pt) [67, 74]. The convergence was tested towards two observables: the geometry (represented by the average distance of hydrogens and carbons from the first layer of atoms) as well as the adsorption energy. The following section 3.2.1 gives a detailed description of the settings used for the evaluation of the convergence behavior. The corresponding results are given in sections 3.2.2 and 3.2.3. Figure 3.2 illustrates the adsorption geometries of benzene on Au(111) and Pt(111) surfaces and the arrangement of the molecule on the surface used in the convergence testing.

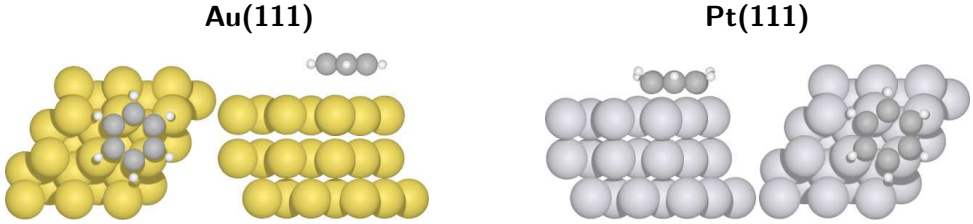

Figure 3.2: *Illustration of adsorption geometries of benzene on a Au(111) and Pt(111) surface. The adsorption site was chosen such as the C-C bonds are inclined by 30° compared to the metal bonds and the carbon atoms placed on a bridged position.*

3.2.1 Computational details:

The all-electron DFT code FHI-AIMS [73][1] was used in the DFT part of the embedding scheme. Following Ref. [67], a 3x3x6 slab of Au(111) and Pt(111), with lattice constants optimized from a run with the PBE [42] GGA functional, namely $g_{Au} = 4.19$ Å and $g_{Pt} = 3.97$ Å was used. The basis sets were chosen as the *tight* standard numerical atom centered sets as supplied by FHI-AIMS. The convergence criteria for the maxium force were set to 10^{-2} eV A^{-1}, 10^{-4} eV for the total energy, and 10^{-5} Å^{-3}. The calculations were done using periodic boundary conditions and the employed k-point

[1] Available from www.fhi-berlin.mpg.de/aims/

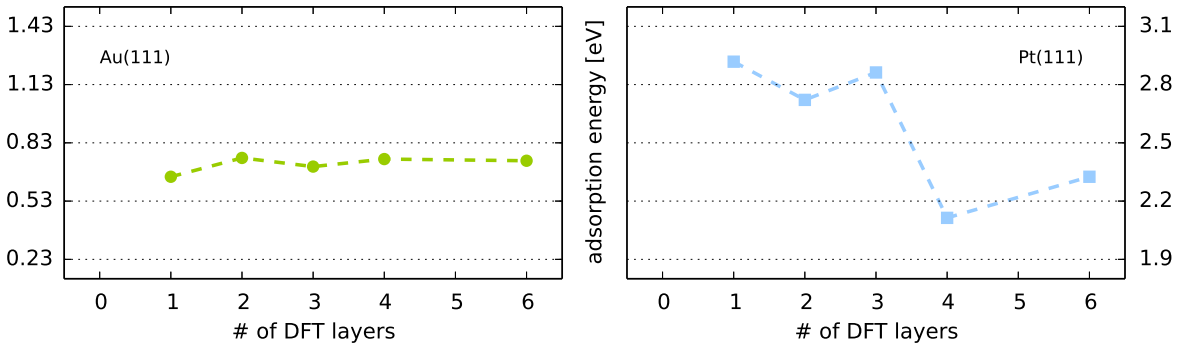

Figure 3.3: *Adsorption energies of benzene on Au(111) and Pt(111) as functions of the number of layers treated with DFT theory. Convergence towards a final value is reached quickly in the case of adsorption to Au (shown on the left), whereas in the case of strong chemisorption more layers need to be taken into account to correctly evaluate the adsorption energy (shown on the right). In both cases the values shown are calculated encompassing a total of 10 layers of* vdW^{surf}*-embedding.*

grid was chosen as a 2x2x1 mesh. For the geometry optimizations we constrained all but the highest-lying $n_{DFT} - 1$ layers and therefore also allowed the surface atoms to adapt to the adsorbate. The dispersive interaction was modeled by the DFT-SEDC module [71] mentioned before, the Hirshfeld-partitioning being dynamically provided by the DFT part. The maximum force value including both contributions from DFT and dispersion correction was set to 0.025 eV A^{-1}. The adsorption height was calculated as the average distance between the first metal layer and all carbon and hydrogen atoms, respectively. The adsorption energy was calculated as the difference between the optimized structure and the sum of the relaxed bulk material and the relaxed isolated molecule:

$$E_{ads} = E^{opt}_{blk+mol} - E^{rlxd}_{blk} - E^{rlxd}_{mol}$$

3.2.2 Convergence of adsorption energy

The dependence of the adsorption energy on the number of explicit DFT layers (n) is shown in Figure 3.3. On Au(111) convergence is reached quickly: Already for $n = 2$ the adsorption energy (0.75 eV) only differs by 0.01 eV ($= 1.35$ %) from the value for $n = 6$. Additionally, the values for $n > 2$ (0.70 - 0.74 eV) show excellent agreement with the adsorption energy determined in Ref. [67] (0.74 eV). In the case of Pt(111), as it would be intuitively expected for a system primarily described by covalent bonding, similar convergence could not be reached even with 5-6 layers. Each additional layer has a much larger effect compared to the values of Au(111) and the adsorption energy only slowly decreases towards the reference value of 1.96 eV [67]. Taking into account the results for both systems, the embedding model seems to be well suited to describe systems which primarily interact by dispersive forces but does not allow a reduction of substrate layers for strongly chemisorbed systems.

Figure 3.4 displays the adsorption energy in relation to the number of layers considered in the description of the dispersive interaction part. In both cases the consecutive addition of further layers of van-der-Waals embedding results in an increase of the adsorption energy and convergence towards a limiting value. Especially for Pt(111) (but to a smaller extend also for Au(111)) the crucial factor is, however, the number of layers treated by DFT, whereas the number of vdW-layers plays a much smaller role.

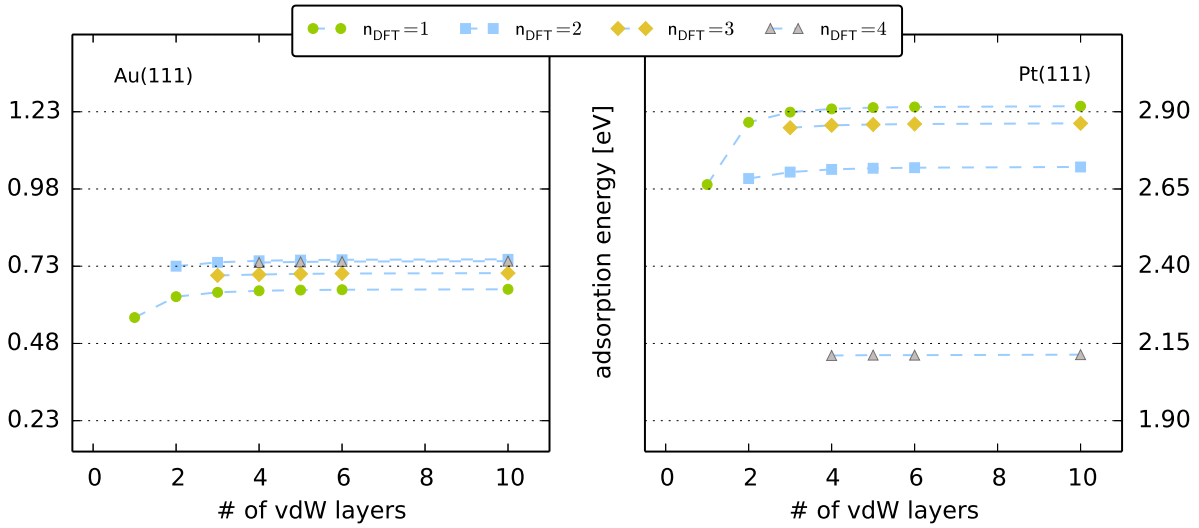

Figure 3.4: *Adsorption energies of benzene on Au(111) and Pt(111) depending on the number of layers treated with dispersive interaction theory (*vdW^{surf}*) in the embedding scheme.*

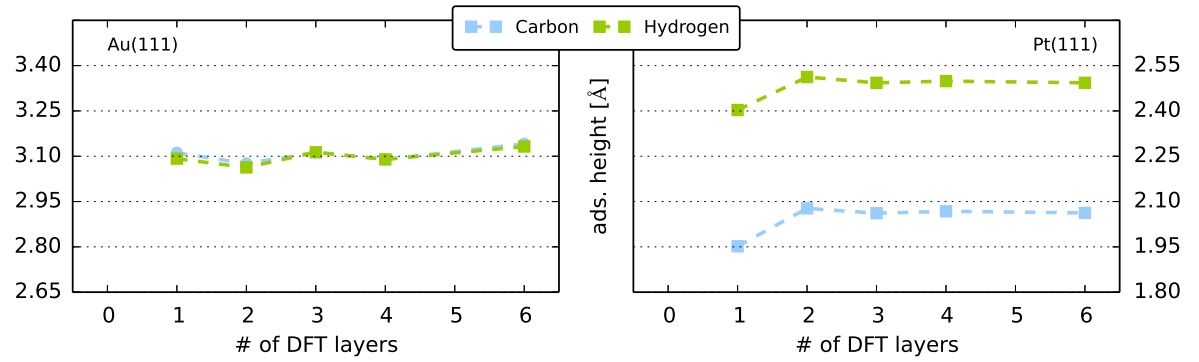

Figure 3.5: *Adsorption height in relation to the number of DFT layers. The bonding character between the substrate and adsorbate is mirrored by the difference in adsorption height of carbons and hydrogens on Pt(111) (shown on the right). The values presented were obtained from a calculation encompassing a total of 10 layers of* vdW^{surf}*- embedding.*

3.2.3 Convergence of geometry

Figure 3.5 shows the dependence of the adsorption height of the carbon and hydrogen atoms on the number of metal layers explicitly included in the DFT description. Two things are observed at this point - in the weakly bound Au(111) system, the benzene molecule remains flat on the surface, whereas on the Pt(111) surface the hydrogens are pointing upwards and the carbon atoms approach the surface - indicative of the stronger covalent bonding on Pt(111). Whereas in the case of Au(111) there is only a small difference between the adsorption height of each additional explicitly considered layer (in the order of 0.07 Å difference from the lowest to the highest geometry), there are considerably stronger fluctuations present in the system with benzene adsorbed to Pt. The convergence of the geometry in relation to the number of vdW^{surf}-layers is shown in Figure 3.6. Changes in geometry were observed only by the first or second additional layer considered. This behavior is expected and physically intuitive, since the attractive forces of lower-lying metal atoms are decaying strongly with distance and are not expected to contribute equal changes in geometry compared to the first few layers at the organic-inorganic boundary region.

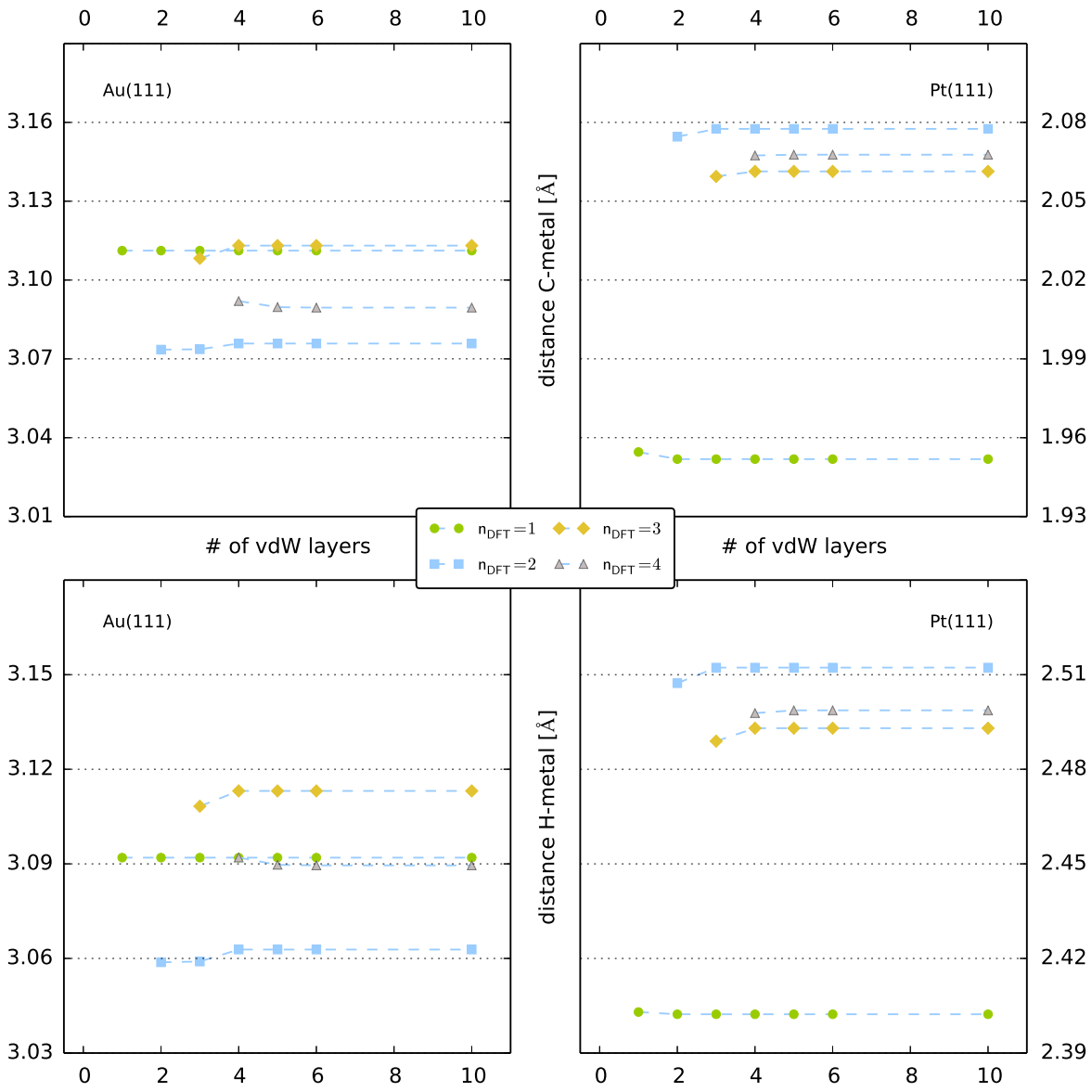

Figure 3.6: *Convergence behavior of adsorption height of benzene on Au(111) and Pt(111) in relation to the number of layers treated only with dispersive interaction (*vdW^{surf}*) in the embedding scheme. Due to the constraints imposed on the geometry during the optimization, changes are only observed for an all but equal amount of layers within DFT and dispersive correction. The embedding scheme therefore primarily contributes energetic corrections by incorporating a large amount of dispersively interacting layers.*

3.3 Summary and Conclusion

In this chapter an embedding scheme was presented, which enables to cut down on the computational cost required for the treatment of organic adsorbates on a Au(111) surface. The applicability of this scheme was evaluated by varying the number of metal layers considered explicitly by DFT calculations within an optimization of physisorbed benzene on a Au(111) and chemisorbed benzene on a Pt(111) surface and analyzing the adsorption energy and geometry (evaluated through the average adsorption height of carbons and hydrogens). This led to the observation of benzene on Au(111) showing fast convergence towards a final geometry and adsorption energy with only two explicitly considered layers.

On the Pt(111) surface, similar convergence was observed for the geometry, but due to the stronger covalent bonding interaction the adsorption energy requires more metal layers treated explicitly with DFT. It was observed that the adsorption geometry converges faster than the adsorption energy and the embedding model performs well for predominantly physisorbed adsorbates.

From the above observations and due to the fact that a system adsorbed on Au(111) will be studied within this embedding scheme, the minimal amount of layers which have to be included in the DFT part of the calculation will be two, since there is almost always a big difference observed between the results obtained from a description by only one metal layer and the addition of a second one. Further layers do not improve these results by the same amount and can therefore be disregarded for preliminary studies. Since stronger bonding of the retinoic acid can be expected because of the carboxy group at the end of the conjugated chain, using two layers of DFT is considered the minimal choice in describing the geometry of the adsorbed molecule. This will enable a rather accurate preoptimization and geometry screening, whereas energetics will have to be evaluated at a full DFT level. As for the dispersive part, ten layers of metal will be used, since convergence is definitely achieved at this point and the dispersive interaction does only add a negligible amount of additional computational cost whilst at the same time systematically improving the energetics.

Some slight disagreements were observed compared to the reference results [67]. These are associated with the optimization procedure using the BFGS algorithm as implemented in ASE as well as the choice of a smaller k-point grid, which was shown to have a non-neglectable influence on the outcome of a geometry optimization [74].

Chapter 4

Isolated Retinoic Acid

The photochemistry of isolated retinoic acid or retinoids in general is well studied and involves a photo-induced isomerization upon direct UV-excitation. In contrast, upon application of a bias voltage to retinoic acid molecules adsorbed on Au(111) STM topographs show three distinct states (cf. Chapter 1, Figure 1.1) associated with different Kondo lineshapes (Figure 1.2) and potentially also involving isomerized species. There are many reasons to believe that the underlying mechanism of the surface-adsorbed process is qualitatively different from the gas phase case. Not only will almost all electrons be absorbed by the metal substrate rather than the thin overlayer of molecules, but furthermore the presence of magnetic impurities giving rise to a Kondo effect points to a charge or spin transfer between adsorbate and substrate (or tip).

Photon- or electron-induced reaction dynamics of metal-adsorbed molecules can be understood in terms of the models of Menzel-Gomer, Redhead [75–77] (MGR), and Antoniewicz [78] (see Figure 4.1). These simple one-dimensional models have proven successful in the interpretation of photon- or electron-induced desorption processes of adsorbates from metal surfaces (desorption induced from electronic transitions – DIET), where a charge-transfer from or to the substrate induces an ionic resonance in the molecule. The corresponding excited state, although short-lived, induces nuclear motion, which suffices to overcome a reaction barrier.

In recent years these mechanisms have also been used to guide the interpretation of non-dissociative chemical reactions driven by indirect photoexciation or inelastic electron tunneling through a STM junction [77, 79]. In this case the successful switching depends on the probability of inducing such a cationic or anionic resonance in the frontier orbitals of the adsorbate molecule, which would also involve the occurrence on an unpaired spin that could give rise to a Kondo resonance.
In the following chapter the stability and electronic structure of such resonance states is studied for selected gas phase isomers of ReA, with a special focus on their magnetic properties in states different from the singlet ground state.

4.1 Computational details

To evaluate the gas phase molecules with DFT, the software package TURBOMOLE [80] and the GGA-functional PBE [42] and hybrid-functional PBE0 [43] were used in geometry optimizations with the triple zeta gaussian basis set def2-TZVP [81, 82] and a convergence setting of 10^{-6} hartree for the energy and 10^{-3} for the gradient. The integration grid for the exchange correlation functional was specified as m4 [83]. All geometries were optimized and the DFT total density and spin density ($\rho^{\alpha} - \rho^{\beta}$) of the converged KS-orbitals determined.

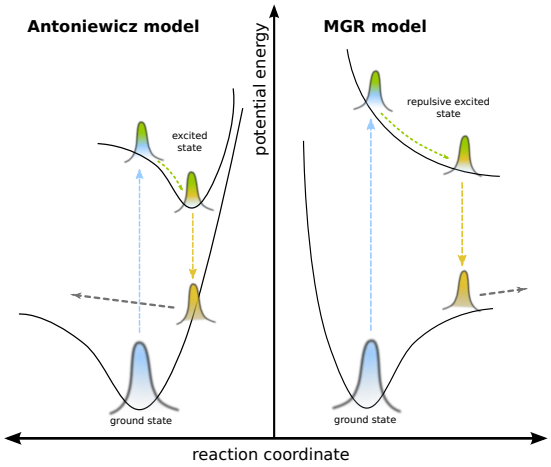

Figure 4.1: *Illustration of the Antoniewicz and Menzel-Gomer-Redhead mechanisms. In either case the adsorbate is first excited, however the topology of the excited state is repulsive in the MGR model and has a minimum in the Antoniewicz model. The excited molecule then relaxes on the excited PES and gains kinetic energy. The relaxation to the ground state can then be followed by a propagation into a different minimum if the kinetic energy of the molecule suffices to overcome the barrier.*

The Coupled Cluster reference calculations were done using the CC2 approximate coupled cluster doubles model [38] and the def2-TZVPP basis and auxiliary basis set [84] with a convergence criterion of 10^{-7} hartree for the energy and 10^{-7} for the one electron density convergence. Due to the computational expense of CC2, only single-point calculations were performed on top of optimized DFT-geometries and the total density as well as spin density explicitly constructed from the optimized orbitals afterwards. The electronic occupation was enforced in the initial Hückel approximation during the initialization of TURBOMOLE.

4.2 Geometry and Energetics

Four different geometries of retinoic acid were chosen to be studied by DFT in the gas phase. All of these geometries were optimized within the constraint of a specified open-shell electron configuration. Since the experimental results suggested a possible electron transfer between the molecule and the rest of the system (STM tip and metal surface) and the mechanistic nature of transition or excitation introduced above suggested the same, singlet (as the *reference*, unperturbed ground state), triplet as well as doublet configurations (anionic and cationic) for all four investigated geometries were studied. These configurations were chosen because they constitute the smallest changes in occupation possible and are hence potential candidates to model the observed transitions by either addition or removal of an electron. The triplet state is considered to account for the possibility of an internal change in electronic structure.
The four starting geometries analyzed in this chapter were chosen based on the X-ray data of a crystal of retinoic acid [85], labeled ***x*** in Figure 4.2. In the experiment the all-trans isomer (labeled ***at***) was evaporated and deposited on the metal surface, therefore this structure and associated geometric and electronic transitions are of special interest. Furthermore, the isomers of 7-cis-retinoic acid (labeled ***hzat***) and the 7,12-cis-retinoic acid isomer (labeled ***hz***) were studied, the former one because of the change in contrast in Figure 1.1 occuring at the cyclohexene ring system and the latter one to evaluate how multiple switched bonds affect the electronic structure and energetics of the molecule.

The geometries of the four isomers in Figure 4.2 were optimized for each of the above mentioned electronic states. Their relative energies with respect to the geometry with lowest energy (***x*** in all cases) are shown in Table 4.1. The ***hz*** and ***at*** geometries are of similar stability and are both less favoured than the crystal structure ***x*** but preferred over the most disfavored isomer: ***hzat***. Switching of the bond next to the cyclohexene-moiety might be suggested by the change in brightness of the protrusion associated with this part of the molecule in the experimental observation (cf. Figure 1.1). A cis-isomerization of ***at*** or ***x*** conformation (or in other words any of the two isomers on the left side of Figure 4.2 being transformed into one at the right side) would encompass a transition into an energetically disfavoured isomer, requiring the addition of further energy to the system. These

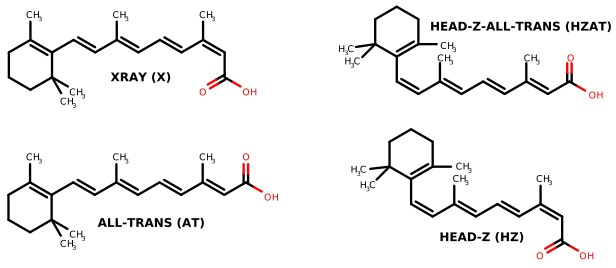

Figure 4.2: *Skeletal formulas of isomers of retinoic acid used in the preliminary gas phase investigations and the abbreviations used to designate them in this chapter. The all-trans isomer (**at**) was evaporated and deposited in the experiment, the structure designated (**x**) is the skeletal formula representation of published X-ray data [85] of a crystal of this particular isomer and was chosen as the starting geometry to construct templates of all shown structural formulas.*

observations are independent of the electronic occupation chosen and do not reveal any information upon stabilization of a certain geometry due to the addition, removal, or reordering of electrons. All these trends are observed for PBE and PBE0 calculations with similar relative energies between geometries. This is an important finding, since upon taking into account the Au(111) support in Chapter 5, a pure GGA functional is required, whereas without it usage of a hybrid functional is preferred[1].
The optimized geometries of all isomers are shown in Figure 4.3 together with their spin density distributions (which will be discussed in the following section). The depicted geometries are those obtained from DFT calculations with the PBE0 functional, which are essentially identical to those obtained with PBE. It is remarkable that the different electronic configurations of isomers ***x, at***, and ***hz*** converge towards similar geometries, while ***hzat*** has a different arrangement of the nuclei for each electronic configuration. This suggests that the ***hzat*** isomer is prone to geometrical readjustment in the vicinity of the ring system or, put differently, that for ***hzat*** there is a correlation between the electronic structure and the geometry, which is a very important finding towards identifying switchable intermediates.

4.3 Spin density distributions

The energetics of the optimized geometries alone do not allow an identification of the switched states observed in the experiment. Since the effect measured by our experimental collaborators seems to be located within the vicinity of the ring system, in the next step the spatial distribution of the electron density is analyzed by separation of the contributions of different spins. Therefore the spin density distribution $\rho^{\alpha} - \rho^{\beta}$ (the difference between unequal spins within the same molecule for each different geometry) was determined to identify preferred sites of excess spin on the molecular backbone. Since STM is capable of atomic resolution measurements and the Kondo effect was observed with the tip positioned above the cyclohexene-moiety, the information gained from the spin density distribution could in principle predict a Kondo effect by localization of the excess spin. Furthermore, the difference in total density $\rho_i^{tot} - \rho_{singlet}^{tot}$ for ρ_i^{tot} of the triplet and the doublet states was calculated. This quantity allows the interpretation of the likelyhood of electronic interaction by addition, removal, or rearrangement of electrons within the spatial domain. Since the densities are calculated on the same molecular backbone, this would correspond to a vertical transition and therefore to the first step of the mechanisms discussed in Figure 4.1.

In Figure 4.3 the optimized geometries introduced in the previous section are displayed together with the associated spin density difference calculated by DFT in an anionic, triplet, and cationic state. In the bottom of Figure 4.3 the spin density distribution in all-trans retinoic acid $\rho^{\alpha} - \rho^{\beta}$

[1] For details on the general performance of density functionals consult Chapter 2.2 or [41]

Table 4.1: *Relative energies of optimized structures of isomers in different electronic configurations for the PBE and PBE0 functional compared to the energetically most stable geometry for each spin state.*

	PBE	E_{rel} [eV]	PBE0	E_{rel} [eV]
anion	x	0.00	x	0.00
	at	0.10	at	0.11
	hz	0.23	hz	0.19
	hzat	0.36	hzat	0.34
singlet	x	0.00	x	0.00
	hz	0.19	hz	0.16
	at	0.21	at	0.22
	hzat	0.47	hzat	0.44
triplet	x	0.00	x	0.00
	at	0.24	hz	0.20
	hz	0.25	at	0.20
	hzat	0.25	hzat	0.23
cation	x	0.00	x	0.00
	at	0.33	hz	0.37
	hz	0.35	at	0.38
	hzat	0.99	hzat	1.07

obtained from DFT calculations is compared to the results of the CC2 calculations of the same systems. It is nowadays accepted that the Kohn-Sham non-interacting one electron orbitals can be interpreted as chemically relevant quantities [86]. From the comparison of the DFT calculation with the CC2 results it can be seen that the spin distributions are similar, which justifies the utilization of Kohn-Sham orbitals for the further analysis. The remaining error is accepted in favour of the computational benefit associated with DFT.

Figure 4.3 displays the ground state geometry in the anionic, triplet, and cationic state of all considered geometric configurations. The localization of the spin density on the molecule hardly deviates for the different geometries: the excess spin density is in all cases distributed over the extended conjugated π system. No unexpected populations on the cyclohexene-moiety are found that could have provided an explanation of the observed experiments. The important observation from these results consists in the fact that the spin distribution is similar within different geometries of the same electronic configuration.

The previous observations already conveyed some information about the electronic structure of the system in terms of spin localization of one specific state. In a next step, the short-term influence of a spin polarisation event will be investigated. In the clamped nuclei approximation (see section 2.1) the movement of the electrons is treated separately from the nuclei. It can be assumed that the experiment starts from the all-trans isomer which then experiences an electron transfer due to the STM-tip and the applied voltage. Subsequently, the electronic structure adapts before the nuclei do. Therefore the total density difference $\rho_i^{tot} - \rho_{singlet}^{tot}$ for ρ_i^{tot} of the triplet and the doublet states of the same geometry might show the effect of this transition.

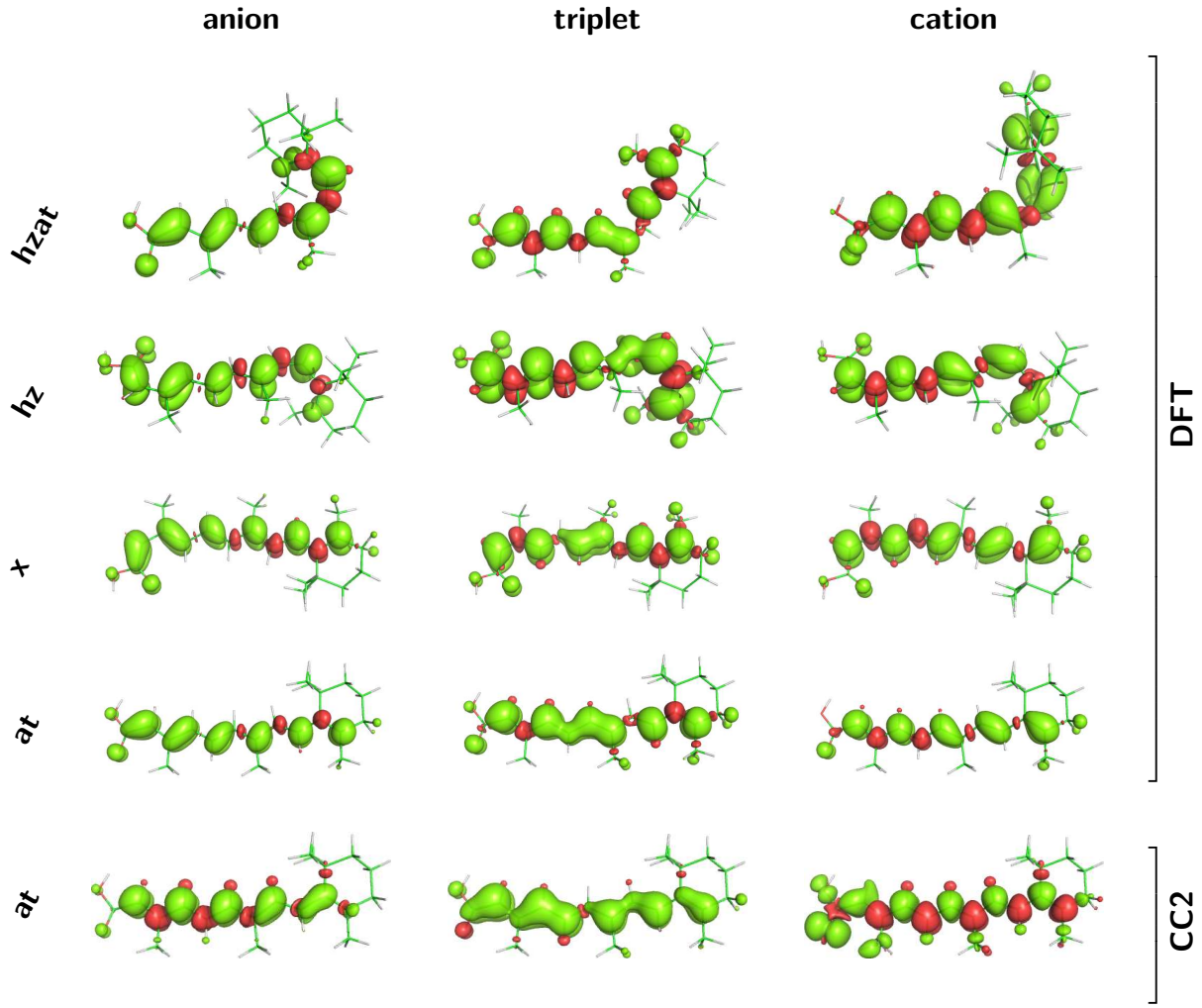

Figure 4.3: *Comparison of differential spin densities (ρ^{α} - ρ^{β}) obtained through DFT calculations for each geometry in anionic, triplet and cationic states and for the all-trans isomer based on a CC2 calculation. Isovalue = 0.002.*

Both cation (Fig. 4.4c) and anion (Fig. 4.4a) show a large rearrangement of electron density distributed all over the molecule, including the ring system. In the case of a cationic (doublet) occupation the excess density is further shifted towards the carboxy-end of the molecule and depleted everywhere else. Additionally, the electron density around the carboxy functional group is contracted compared to the singlet state. For the anionic structure there is no such trend observable. However, in a vertical transition to the anionic state, electron density is depleted from the molecular plane and accumulated on top and below it, whereas in the cationic (doublet) state the behavior is exactly opposite. The intramolecular electron density rearrangement due to a triplet occupation only involves lateral rearrangements and is primarily localized around the center of the conjugated system and depleted from the ends of the chain. Concludingly, the expectation from these pictures is that due to a vertical transition, electrons are potentially stronger localized in case of an intramolecular electron rearrangement and a cationic resonance state, whereas by addition of an electron it would diffuse and delocalize over the whole system.

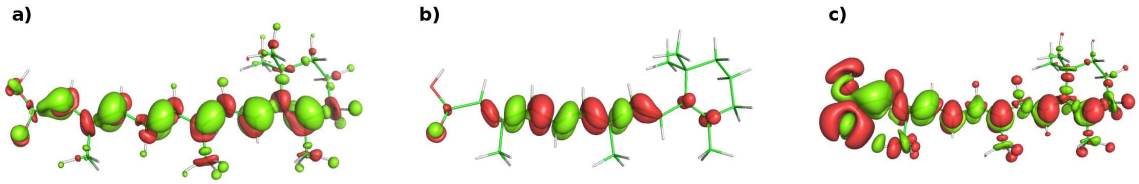

Figure 4.4: *Comparison of CC2 differential total electron density ($\rho_i^{tot} - \rho_{singlet}^{tot}$) of all-trans retinoic acid* ***a)*** *anion* ***b)*** *triplet and* ***c)*** *cation. Red depicts a removal of density and green an increase compared to the singlet density. Isovalue = 0.002*

In the experimental setup, the Kondo resonance was observed on the cyclohexene ring after application of a negative bias voltage (-2.5 V), theoretically leading to tunneling of electrons from the surface to the tip and formation of a cationic state on the surface. The calculated density difference upon formation of a cationic state due to a vertical transition suggests electron depletion at the cyclohexene-ring and a contraction of diffuse electrons around the carboxy functional group. This important perception coincides with the experimental observation of a localized electronic effect in the cyclohexene moiety.

4.4 Analysis of frontier orbitals

If inelastic electron tunneling occurs between a metal tip and a substrate, it involves the interaction of the electronic structure of the tip with the frontier orbitals of the molecule. It was shown that the structure of the molecular orbitals of an adsorbate on a non-isolating surface is accessible via differental conductance (dI/dV) measurements in an STM experiment [87]. However, these molecular orbitals as observed on STM topographs are often not clearly seperated into the propability distributions associated with a single molecular orbital but rather ensembles of these being located around the Fermi level. In Figure 4.5 the highest occupied and lowest unoccupied orbitals of an anionic, triplet, and a cationic state of all-trans retinoic acid (which was deposited in the experiment) are shown.

Usually, the HOMO and all lower-lying orbitals are accessible when probing with negative bias voltage, therefore pulling electrons from the substrate towards the tip. When applying a positive bias voltage, the LUMO and higher lying states are probed. In the current experiment a bias of -2.5 V was applied which would lead to electrons tunneling from the HOMO of the sample to the tip. The Kohn-Sham orbitals presented in Figure 4.5 are similar in appearance and predict a delocalized arrangement of electrons along the molecular backbone within the frontier orbitals. Even the HOMO-1 of the cationic state, which is the orbital with the most extended contributions on the ring system, is mainly located at the molecular backbone.

In Figure 4.6, the influence of Natural Transition Orbitals (NTO)[1] on the HOMO and LUMO are shown. The highest eigenvalues of NTOs are associated with the most dominant correction to the ground state and should therefore highlight the same tendencies ascribed to common HOMO and LUMO orbitals if this correction is added upon the orbitals obtained from a Hartree Fock calculation. The cationic and anionic HOMO predict a predominant localization of propability density on the ring system, whereas the triplet state does not affiliate with this behavior. The localization of cationic and anionic HOMO would coincide with the experimental observation of a bright protrusion in the STM topographs due to tunneling from the substrate to the tip. In the CC2-corrected LUMO orbitals, the most dominant propability amplitudes in vicinity of the ring system are observed on the anionic and triplet structure, expected to be seen upon application of a positive bias inducing tunneling from the tip to the sample.

[1] NTOs are obtained by diagonalisation of the transition density matrix $T(r) = |\Psi_{ex}(r_1, r_2, r_n)\rangle \langle \Psi_0(r_1, r_2, ...r_n)|$

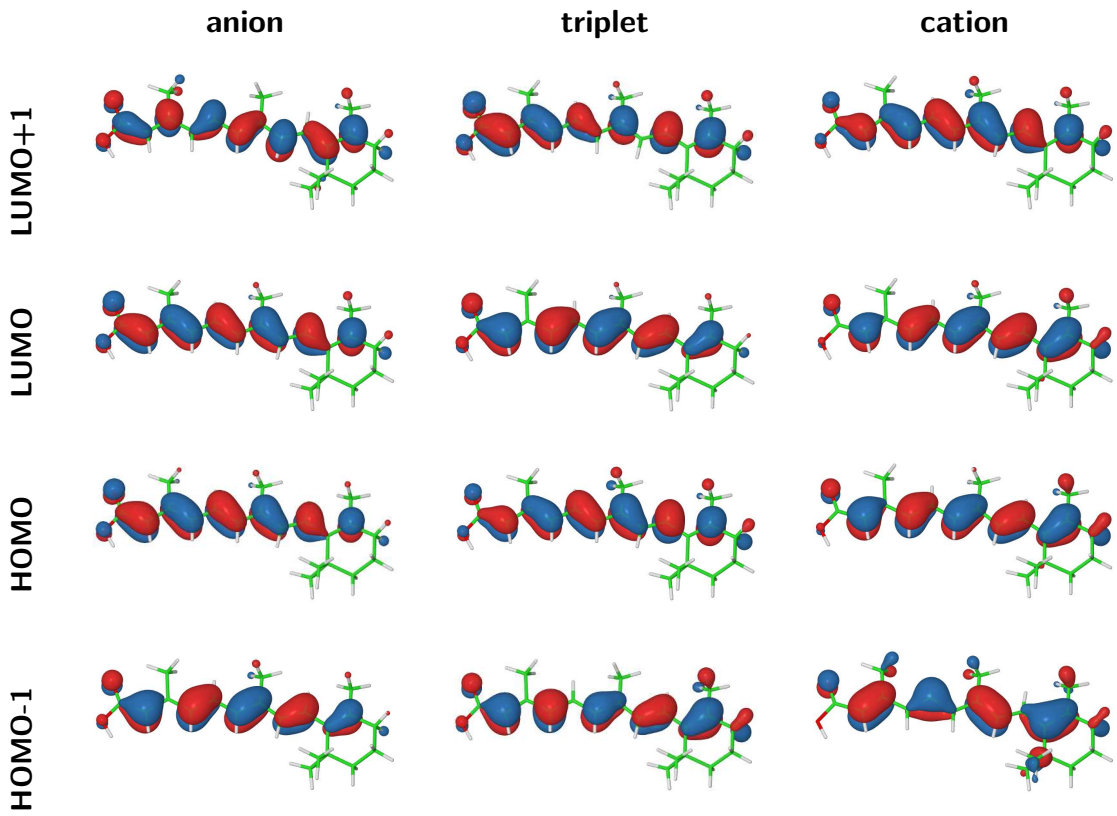

Figure 4.5: *HOMO, HOMO-1, LUMO, and LUMO+1 orbitals of all-trans retinoic acid for the anionic, triplet, and cationic state as calculated with DFT. Isovalue = 0.03*

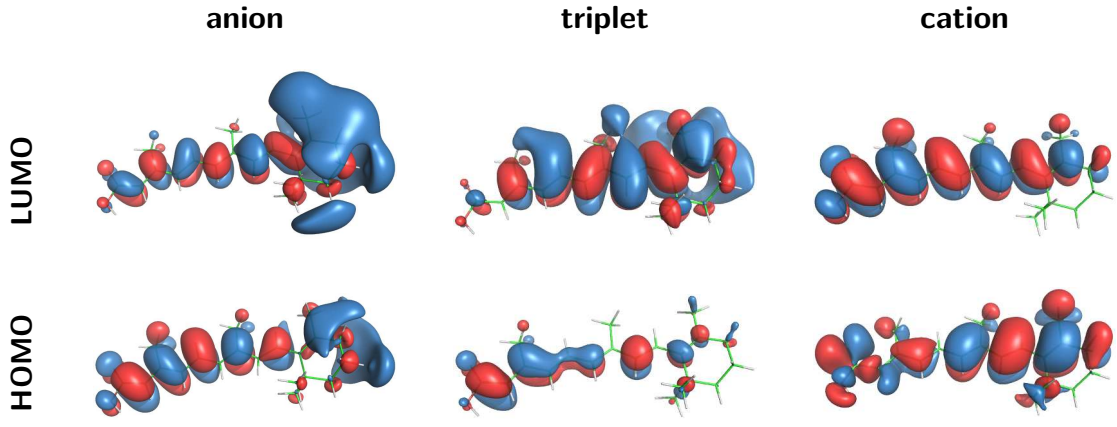

Figure 4.6: *HOMO and LUMO of all-trans retinoic acid corrected by dominant Coupled Cluster Singles amplitudes for the anionic, triplet, and cationic state as calculated with CC2. The orbitals were constructed of the sum of the spatial information of ψ^{α} and ψ^{β} of the highest eigenvalue obtained from decomposition of the basis expansion coefficients of ket-vectors in CC2 (assumed to contribute the most important correction to Φ_0) and the underlying Hartree Fock HOMO and LUMO orbitals. Isovalue = 0.03*

4.5 Summary and Conclusion

In this chapter, four different cis/trans isomers (for skeletal formulas compare Figure 4.2) of retinoic acid were analyzed in different electronic configurations, including singlet and triplet, as well as anionic and cationic states. In a first step the geometry of each isomer was optimized with DFT and the geometries as well as relative energetics compared. It was shown that the most favourable geometry is not universally independent of the electronic configuration but the relative stability of the chosen isomers is. In other words, if the same geometry is optimized in the three aforementioned electronic configurations, the outcome in geometry is different, but the total energy of each optimized geometry still follows the same relative ordering (***x*** $<$ ***at*** $\simeq$ ***hz*** $<$ ***hzat***). When comparing the results of the PBE and PBE0 functionals, no significant differences in either energetics or geometries were observed.
In the next step the differential spin densities ρ^{α} - ρ^{β} were analyzed in order to verify whether a localized unpaired electron spin is present for the investigated geometries. However, no distinct observations of a localized electron spin could be made which would explain the observed Kondo effect. Specifically, no unpaired electron spin is localized only on the ring system but all contributions are rather distributed over the conjugated part of the molecule in a similar pattern for each electronic occupation such as the tendency of localization towards the carboxy functional group and on the conjugated chain in the cation whereas in the anion it is localized in the chain and on the ring system. In the triplet no dominant localization was observed. The localization in the anionic structures could in principle be used to justify the observed Kondo resonance on the ring system, but this conclusion is counterintuitive with regard to the negative bias voltage applied in the experiment requiring electrons to be removed from the system. In conjunction with the partial delocalization in the conjugated chain and on the grounds of this delocalization being even more pronounced in the CC2 reference calculations done in this chapter, these indications are too vague to draw final conclusions. Nevertheless, a comparison with high-level post-HF methods (CC2) allowed to conclude that the accuracy of DFT is sufficient for the studies in this work.
Analysis of the difference in total electron density between the anion, triplet and cation states and the singlet occupation of the ***at*** (all-trans) geometry showed that only in the case of a cationic state a localization of electron density occurs which would be consistent with the observation of a change in electronic structure at the cyclohexene-moiety. Namely, electron density is depleted from the π-orbitals including the ring system and accumulated in the vicinity of the carboxy group, whereas in the anionic state a diffuse delocalization over the whole conjugated system is observed and in the triplet state a rearrangenemt of density in the center of the polyene chain occurs with only negligible influence on the ring system. However, the observed quantity is only a relative measure of electron density and does not contain spin-specific information which would be required in the discussion of the Kondo-effect.
The sum of the Hartree-Fock HOMO and the most dominant natural transition orbital obtained from the CC2 and the HOMO orbitals in DFT are delocalized over the conjugated chain with remarkable dominant propabilities on the ring system in the case of the cationic (NTO-HOMO, DFT-HOMO), anionic (NTO-LUMO), and triplet (NTO-LUMO) configurations. These orbitals can be used to explain the appearance of the STM topographs, with the anionic NTO-LUMO (despite being a counterintuitive orbital to be probed with a negative bias voltage) corresponding to a propability distribution which can be pictured to translate into the bright protrusions observed for switched states.

The study of the four representative geometries in the gas phase has shown that due to the large conjugated system in retinoic acid, electrons tend to distribute. It is therefore difficult to access certain properties, such as to where electrons are moving if the molecule undergoes a transition to a different electronic configuration. Crucial for the understanding of the nature of the localized Kondo effect would be to assign electrons within a confined area of space, which is largely inhibited due

to the delocalization of orbitals and electron density in the conjugated system. Judging from the frontier orbitals and NTOs, some of them could be assigned to the experimental observation in Figure 1.1, however only the HOMO orbitals of a cation are probed by a negative bias voltage and would qualify to explain the appearance of the (unswitched) STM topograph, because the spin density distribution of the cation is a contraindication to a switched state with unpaired spin localized on the ring system. Nevertheless, a few important facts were obtained, such as the correlation between geometry and electronic occupation as highlighted by the geometries obtained by optimization of the ***hzat*** structure. Furthermore, the spin density distribution in the gas phase molecule is largely independent of the geometry associated. Finally and most importantly, DFT is able to correctly describe the electronic structure and reproduce results obtained through more accurate Coupled Cluster (CC2) calculations. The conclusion at this point is that only from the gas phase calculation it is not possible to understand the magnetic properties observed in experiment, i.e. no unpaired spin could be located. Therefore, in the following chapter, the surface and its interaction with the adsorbate will be taken into account.

Chapter 5

Retinoic Acid on a Gold(111) surface

Already in the early 1970s, the application of single molecules as building blocks for molecular electronics sparked interest from a theoretical point of view [88] and has from then on evolved in a new interdisciplinary field of chemistry, physics and material science. Many different approaches were sought for controlling electron transport and realizing logical building blocks or storage devices on the molecular level. This led to the realization that conductivity of electrons primarily occurs through π- rather than σ-bonded systems, that the constitution of frontier orbitals is of paramount importance for the conduction, and the current decays exponentially with the distance from the surface [89]. With the invention of scanning tunneling microscopy [20], a new tool was available to investigate the behavior of molecular building blocks on a surface. It did not take long until the first STM-induced switching of molecules adsorbed on a support was observed [90]. Nowadays, many molecules are known which can be switched via electron tunneling from an STM tip, the most prominent example being Azobenzene and its derivatives [13]. However, molecules known to switch upon external stimuli in the gas phase or in solution do not have to follow the same behavior when adsorbed on a surface. Due to the presence of the surface new pathways and stabilized states can arise - as a matter of fact it was shown that a multitude of factors is responsible for the disappearance of switching, such as: stablilized molecular conformations which appear only upon a certain geometric alignment with the surface comparable to the key-lock principle [91], stabilization of the most planar form of a molecule due to the larger cross section with the surface upon adsorption [92], lateral stabilization due to the presence of multiple adsorbates in an ordered fashion next to each other [93], and the effective quenching of transition states due to their electronic interaction with the metal band structure and thus inhibiting the rearrangement of nuclei [94, 95]. It is hence the complex interplay of a variety of different parameters which enables or disables the reversible switching of molecules on a surface. Popular approaches towards designing such switches include for example the chemical modification of non-switching compounds to increase the steric demand of the molecule and therefore to lessen the interaction with the surface or more fundamental modifications like the introduction of functional groups which result in changes of the switching process [68].

The previous chapter discussed retinoic acid as an isolated molecule in gas phase, where for one of the investigated isomers a correlation between electronic and geometric structures was found. However, it was not possible to locate an unpaired spin which could explain the experimentally observed Kondo feature. Furthermore, the STM images do not allow to conclude whether the observed switched states originate from a change in geometry or are solely based on changes in electronic structure. However, since changes in the electronic structure are expected upon switching owing to the observed Kondo-effect, it has to be assumed that a concurrent structural rearrangement plays a role in the switching process on the grounds of the mentioned correlation between geometry and electronic structure. Retinoic acid consists of an extended π-system coupled to a flexible cyclohexene

moiety, which is prone to conformational rearrangement itself as has been shown before [64]. Even though a cis/trans - bond switching for the center of the chain seems unlikely due to no direct evidence of this in the STM topograph, still a variety of different geometric changes are thinkable. Possible changes include tilting or twisting the ring system in relation to the chain or switching the conjugated bonds in direct vicinity to a cis-configuration, which might be hidden in the STM topograph due to the lateral extension of the dominant protrusion upon switching (cf. Fig. 1.1). Viewing the retinoic acid molecule in the light of the parameters controlling bistability of surface-adsorbed switches introduced above (such as the influence of lateral interactions [93], or preferred adsorption of flat conformations [92]) allows to speculate that the deposition on the surface leads to a flat initial geometry. However, as pointed out in Ref. [93], lateral dispersive interactions could stabilize the tightly-packed ring-systems of retinoic acid, allowing molecular conformations which would not correspond to a local minimum in the potential energy surface of the isolated molecule. A cis/trans bond-switching in the conjugated carbon chain would also not prevent a flat adsorption. The first step in elucidating the influence of the metal surface on the adsorbate is to find geometries which are consistent with experimental observations. This represents a high-dimensional problem due to the multitude of possible internal deformations. Therefore a computational screening approach using DFTB will be employed which makes use of the van-der-Waals embedding described in Chapter 3: It allows to take into account a huge number of possible candidates and to identify possible adsorption geometries. The such obtained geometries will be analyzed further to verify whether single spins can be localized on the molecules, which could provide an explanation for the observed Kondo-feature. Finally, in section 5.3, the analysis of a few selected geometries will be repeated using full DFT calculations to verify the validity of the screening approach.

5.1 Computational Details

To enable an efficient computational screening of a large number of geometries, the embedding model introduced in Chapter 3 was coupled with the DFTB-software Hotbit [54], which was parametrized using results obtained from DFT-calculations with the PBE functional [42] in FHI-AIMS [73]. All optimizations were done in a periodic supercell approach, mimicking an extended surface. In the vertical direction slabs are separated by sufficient vacuum space in order to minimize interactions between the slabs. The initial geometry of each calculation is chosen such that the ring system is adsorbed similar to benzene on Au(111), where the C-C bonds of the ring are inclined by 30° and the nearest distance between atoms of the surface and the molecule does not lie below 2 Å.

The DFTB equations were solved self-consistently and a Multipole-Expansion was used [96] to calculate the Coulomb-Contribution. Therefore in x and y lateral directions, five periodic images were considered, whereas none in the vertical direction (k = (5, 5, 1)), together with a choice of n = (3, 3, 1) numbers of points within each cell to contribute to the expansion. Furthermore, the

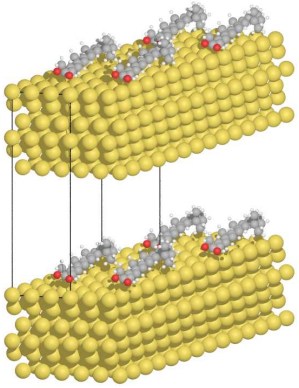

Figure 5.1: *Geometry of the supercell used in the calculations for retinoic acid on Au(111). The box encloses one image of the supercell which is repeated along the borders mimicking an endless surface. Van-der-Waals interactions between neighboring units of the adsorbate are deactivated to simulate a low-coverage situation.*

maximal width of the Fermi broadening function was limited to 0.1 eV, the density convergence was set to 10^{-7} Å^{-3} difference between consecutive iteration steps by using the Pulay-mixing procedure [97] and the k-lattice was chosen as a 2x2x1 grid. Dispersive interactions were accounted for by the dftdisp-module introduced in Chapter 3 whereas the system was seperated into two domains, namely the adsorbate and the surface. Interactions between adsorbate and surface were accounted for, whereas lateral interactions with the periodic images were deactivated for the adsorbate and between the slab and its images in the c-direction orthogonal to the surface facet. Furthermore, intramolecular dispersive interactions were deactivated for the substrate and the C_6^{AB} coefficients for Au rescaled by 0.9452, a constant which arises due to the fact that the vdW$^{\text{surf}}$ scheme is referenced to atomic volumina in a metal bulk [50], whereas the initial theory employed the free atom volume as a reference [49]. The value was provided by Dr. Maurer [68]. The Hirsheld-partitioning as described within the vdW$^{\text{surf}}$ method could not be applied, due to the lack of evaluation of Hirshfeld volumina in Hotbit. The embedding model was setup with two explicit layers treated by DFTB and six layers of dispersive interaction and treated within the frozen surface approximation by constraining all metal atoms. The metal surface was constructed as a 3x7x6 Au(111) surface with a PBE-optimized lattice constant of $g_{Au} = 4.19$ (using FHI-AIMS) and 10 Å of vacuum between the metal slabs in the vertical direction. The overall convergence criterion for the geometry optimizations was chosen to be a maximum force of 0.025 eV/Å per atom using the BFGS algorithm as implemented in ASE. The calculation of the local density of states (LDOS), needed to simulate STM topographs according to Tersoff and Hamann [61] was calculated in a single-point calculation with a bias voltage of -2.5 V and a real space grid spacing of 0.2 Å and different values for the cutoff (3.0 Å, 4.0 Å, 4.5 Å, 5.0 Å).

Optimization of the retinoic acid molecules in a dimeric structure similar to that presentin the STM image (Figure 1.1) was also calculated using DFTB, however due to the extensive system size the software DFTB+ [58, 98] was used instead of Hotbit. In order to enable the use of DFTB+, a conversion script was written that converts DFTB-parameters from Hotbit-format into DFTB-format[1]. In contrary to Hotbit, DFTB+ can be run in parallel on multiple CPUs which reduces the computing time drastically. The computational settings for DFTB+ were chosen to be equivalent to the Hotbit-settings mentioned above, by usage of the charge self-consistent (SCC) method, with the density convergence set to 10^{-7} Å^{-3} difference between consecutive iteration steps and a 2x2x1 mesh of k-points in the Brillouin zone. However, DFTB+ is not able to calculate the local density of states (LDOS) from the parameter set provided by Hotbit. Therefore, the LDOS was calculated in a single-point calculation using Hotbit with the same settings as specified above, except for the Coulomb potential being solved by the DirectCoulomb method instead of the Multipole Expansion, which can not be used for cells deviating largely from a cubic reference system. The Coulomb potential was therefore cut off using an error function at a distance of 30 A. The dispersive part of the embedding model was treated equally as described above. The metal surface for the dimeric structures was constructed as a 3x12x6 Au(111) slab with a PBE-optimized lattice constant of $g_{Au} = 4.19$ and the vacuum between the two metal slabs was set to 20 Å. The overall convergence criterion for the geometry optimizations was chosen to be a maximum force of 0.025 eV/Å per atom using the BFGS algorithm as implemented in ASE.

The DFT optimizations of selected adsorbate geometries in section 5.3 were done using FHI-AIMS and the PBE functional on a 3x7x10 Au(111) ($g_{Au} = 4.19$) slab. Hereby the adsorbate geometry obtained from the DFTB screening approach served as a starting point. For the geometry optimizations two gold layers were considered within the explicitly treated region with FHI-AIMS and the whole system within dispersive interaction embedding. For the calculation of adsorption energies and the LDOS four excplicit DFT layers were used. The basis set was chosen as the *light* standard numerical atom centered set for the geometry optimization and *tight* for calculation of the

[1] For further details see Appendix A.3

adsorption energies and the LDOS. The convergence criteria for the maxium force were set to 10^{-3} eV/Å, 10^{-4} eV for the total energy and the density convergence set to 10^{-7} Å^{-3} difference between consecutive iteration steps. The calculations were done within a periodic system as mentioned above and the associated k-point grid was chosen as a 2x2x1 mesh for the optimizations and a 4x2x1 mesh for the calculation of the adsorption energy. The scalar zeroth order relativistic atomic scaling (ZORA) was applied for heavy atoms with a treshold of 10^{-6} eV. Gaussian broadening of the Fermi electron occupations with 0.1 eV was applied. The dispersive interaction was accounted for with the same settings as in the screening approach with the notable exception of lateral interactions between molecules being turned on. The overall convergence criterion for the geometry optimizations was chosen to be a maximum force of 0.025 eV/Å using the BFGSLineSearch algorithm as implemented in ASE. The LDOS was calculated with bias voltages of -2.5, -1.5, +1.5, and +2.5 Volts on a grid spaced with 0.1 Å.

5.2 Screening of geometries on the surface

A computational screening approach consists in the parallel evaluation of selected properties of a representative library of compounds (or in this case geometric structures) and in systematically eliminating some of these structures based on different observables. The remaining members of this library have to be classified and become the starting point for a more detailed treatment by more sophisticated methods. In order to properly describe the geometry of ReA on the surface, a variety of different internal degrees of freedom of the adsorbate has to be taken into account (Figure 5.2).

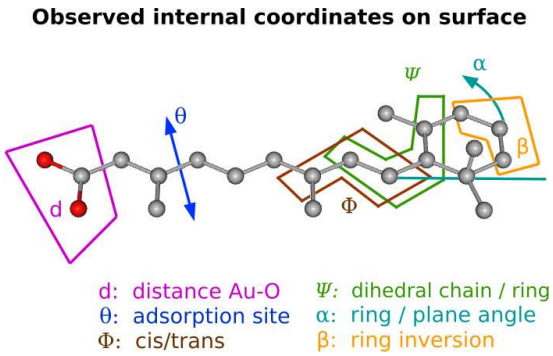

Figure 5.2: *Observed internal degrees of freedom of adsorbed retinoic acid considered in the screening approach in this work. The parameters $\Phi_{1,2}$[1], $\Psi_{1,2}$ [2], α, and β were varied based on chemical intuition and all the resulting geometries optimized on the metal surface. Furthermore, the removal of hydrogen atoms from the ring system was simulated for each of the potential geometric candidates. The analysis and classification was based on all shown parameters.*

Ψ_1 and Ψ_2 designate dihedral angles between the ring system and the onset of the conjugated chain, Φ_1 and Φ_2 are dihedrals describing the cis/trans configuration from C7 to C9. α is the angle between the polyene chain and the surface facet, whereas θ is the angle with the Au-Au orientation. β is used to illustrate the state of the ring conformation (either identical to the X-ray structure [85] or inverted). The distance between the oxygen atoms and the surface is designated by d_1 and d_2. Based on these internal coordinates and the suggestion of our experimental collaborators [24] to investigate the possibility of deprotonation of the adsorbate due to the applied tunneling voltage[3], a total of 122 different starting geometries were constructed. Those geometries were optimized on a Au(111) surface as described in section 5.1, followed by the determination of the internal coordinates and the adsorption energy. Approximately 25% of all optimized conformations were discarded in this first step if either the geometries were heavily distorted, bond breaking or different chemical rearrangement of the molecule occured which were not to be expected in the experiments and/or chemically unreasonable, or the convergence criteria imposed on the calculations could not

[1] Φ_1 and Φ_2 designate the cis/trans configuration of the bonds between carbon atoms C7-C8 and C8-C9, respectively.
[2] Ψ_1 and Ψ_2 designate the dihedral angle between carbon atoms C8-C7-C6-C5 and C8-C7-C6-C1, respectively.
[3] This event was simulated by systematic removal of hydrogens on the ring system for every proposed geometry.

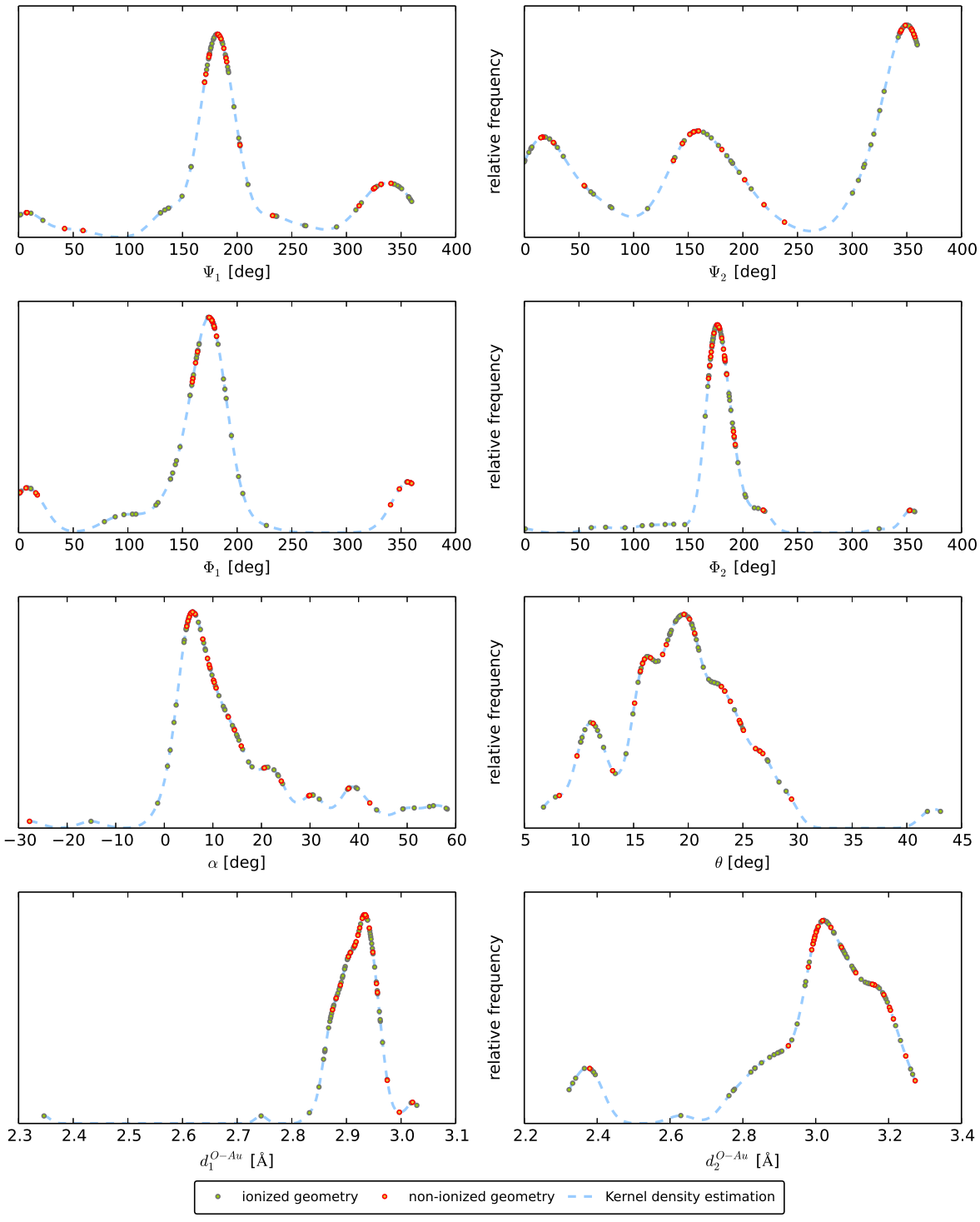

Figure 5.3: *Kernel Density Estimation of the observed interal parameters of optimized retinoic acid geometries on the surface. The non-converged and evidently wrong geometries (due to bond breaking or other chemical rearrangement) were excluded from this analysis. Highlighted in red are the non-ionized geometries, leading to the conclusion that due to ionization no additional geometric features arise.*

be reached. The remaining 75% of different geometries were still too numerous to evaluate *per inspectionem*, which lead to the application of a statistical methodology known as Kernel Density Estimation (KDE). The KDE is a mathematical method which allows to transform a randomly distributed dataset into a continuous function describing the relative frequency of a certain value within the given set of values [99, 100]. A probably more familiar tool to accomplish a similar visualization is the use of histograms, which however lack the versatility of a smooth continuous function. All internal coordinates of the geometries analyzed in the KDE in Figure 5.3 are listed in Appendix B.1, Table B.1.

In Figure 5.3 the Kernel Density Estimation of the observed internal coordinates is shown, overlaid with green dots of the ionized geometries and red dots of the non-ionized conformations. This visualization was accomplished with a Gaussian density kernel method as implemented in SciPy [101]. This distribution function allows not only to visualize and therefore easily determine the most probable values of the internal coordinates but also leads to one important finding, namely the presence of non-ionized geometries within all regions of elevated relative frequency. This leads to the

Table 5.1: Classification of optimized geometries on the surface after the screening approach and statistical analysis by Kernel Density Estimation validating the exclusion of ionized geometries

	ID	F^{max} [meV/Å]	E^{Ads} [eV]	Properties
①	hr8	23.6	3.14	▪ all-trans ▪ ring adsorbed flat
	hr10	18.6	3.14	
	hr5	18.9	3.12	
	hr4	20.7	3.12	
	hr16	22.7	3.29	▪ all-trans ▪ ring inversion[1]
	hr15	19.1	3.05	
②	hr21	14.3	3.11	▪ C7/C8 cis-isomer ▪ ring adsorbed flat[2]
	hr18	21.2	3.04	
	hr25	16.0	2.75	
	hr6	18.7	2.70	
	hr22	18.4	2.68	
	hr12	14.6	2.47	
	hr24	17.1	2.43	
③	hr14	12.3	2.95	▪ all-trans ▪ Dimethyl towards surface
	hr23	18.6	2.58	
	hr20	16.5	2.41	
	hr17	20.1	2.28	
	hr19	39.2	2.13	▪ Methyl towards surface

[1] The *common* ring conformation is identical to the X-ray structure (cf. Chapter 4, Fig. 4.2 and 4.3, isomer ***x***).
[2] Except geometry hr12 where the ring system is elevated.

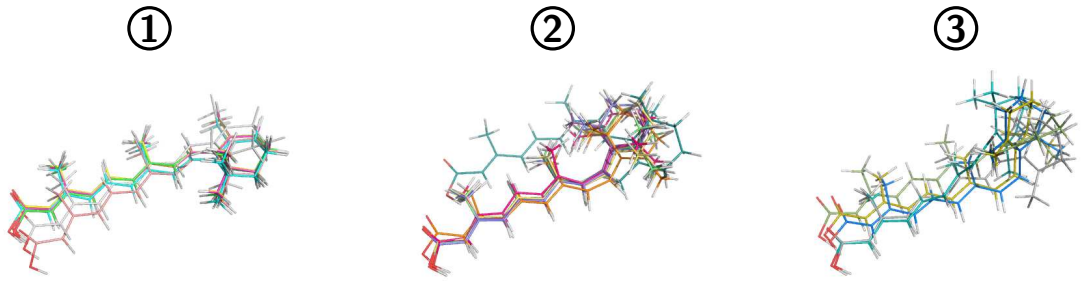

Figure 5.4: *Overlay of the geometries assigned to groups in Table 5.1*

conclusion, that the adsorption geometry is largely invariant to an ionization of the adsorbate and it is therefore a valid simplification to discard all geometries associated with ionization and continue evaluation of only the remaining non-ionized 18 geometries. This is further justified by the reversibility of the experimentally observed STM-induced switching, which points to a non-dissociative process.

These 18 remaining geometries (listed in Table 5.1) can be classified into three main groups approximately similar in size: the first one contains all flat adsorbed geometries in all-trans configuration (shown in Figure B.1). The major differences observed between the isomers of this group are reducible to different adsorption positions on the surface as well as an inversion of the cyclohexene ring conformation. A well-aligned adsorption geometry of a flat molecule on a flat surface gives grounds to expect a high adsorption energy. In fact, the isomers of group one show the highest adsorption energy with an average of 3.1 eV. The second group (Figure B.2) encompasses all conformations associated with a single conjugated bond switched into a cis-conformation. All these isomers are adsorbed flat on the surface; the location of the switched bond, the adsorption site on the surface, the orientation of the ring system in relation to the chain, and the ring inversion are the distinguishing parameters. The adsorption energies of this group are significantly lower than those obtained for the first group, which leads to the conclusion that a switched bond is disadvantageous for the adsorption of ReA on Au(111). The absolute values lie between 2.43 and 3.11 eV. The third and last group contains geometries with the cyclohexene ring rotated approximately 90° in relation to the horizontal plane spanned by the aromatic chain, leading to an adsorption with the methyl- or dimethyl-substituent pointing towards the surface (Figure B.3). The difference between the conformations are the exact degree of rotation and resultant additional changes (e.g. buckling due to the steric strain) in the chain. This third group of isomers is characterized by an even lower adsorption energy than the previous geometries introduced. The absolute values between 2.13 and 2.95 eV are rationalized by the enforced twisting of the ring system, leading to a partial desorption of the flat polyene chain. The significance of the adsorption energies in comparison to other adsorbates will be further described in section 5.3 using adsorption energies calculated from high-level DFT theory, whereas the energies obtained from DFTB calculations in this chapter should be seen as a qualitative measure. Figure 5.4 shows an overlay of all geometries belonging to one group (as classified in Table 5.1) and illustrates the degree of similarity within each group. It follows from the observation of these geometries, that the most interesting conformational changes in terms of torsion angles between the cyclohexene ring and the remaining conjugated system occur predominantly within group three and only partially within group two. The first group consists entirely of geometries without these properties. This would suggest the adsorbate conformation of the unswitched state **N** can be found within the former two groups, while the switched state is more likely to be found in group three.

The geometric features of the third group - a rotation of the ring system - lead to a distinct increased height of the molecule which would be a likely candidate for a protrusion in the experimental

STM topograph. In order to verify this assumption and to isolate more likely candidates for the four observed states, simulations of STM topographs in the form of Tersoff-Hamann simulations were performed for all members of each group. In order to simulate the size of the tip and the associated blurred experimental STM signatures when probing the surface, a rolling-ball model in conjunction with a gaussian smoothing algorithm was applied, thankworthily provided by Dr. Maurer. The simulated STM topographs of four representative geometries are shown in Figure 5.5, together with the differential spin density of the adsorption geometry in the gas phase.

In Appendix B.2, the simulated STM images of all isomers belonging to the groups introduced above are shown. The direct comparison of these images inside each group allows to interpret how a small change in geometry translates into a change in contrast in the final image. Figure B.1 depicts STM images of isomers belonging to the first group. Most topographs in this group are almost identical with the exception of a different chain alignment (θ) of isomer hr16. The second group (cf. Figure B.2) contains some isomers (hr22, hr12, hr24) with differently shaped protrusions of the cyclohexene-moiety compared to the first group which is caused by a ring inversion and a slight increase in the adsorption angle α (cf. Table B.1). Furthermore, the effect of a different alignment of the polyene chain in isomer hr6 is observed. Figure B.3 contains the isomers of group three, which are all characterized by a large increase in the brightness of the protrusion corresponding to the ring system. The changes in the shape of this bright protrusion are rationalized by the type of adsorption with either one (hr17) or two (hr19) methyl substituents pointing away from the surface or the stabilization of the upright ring system by buckling the polyene chain into a cis conformation at C7 (hr23, hr20). The less brightest isomer (hr14) is only slightly twisted and therefore shares a larger

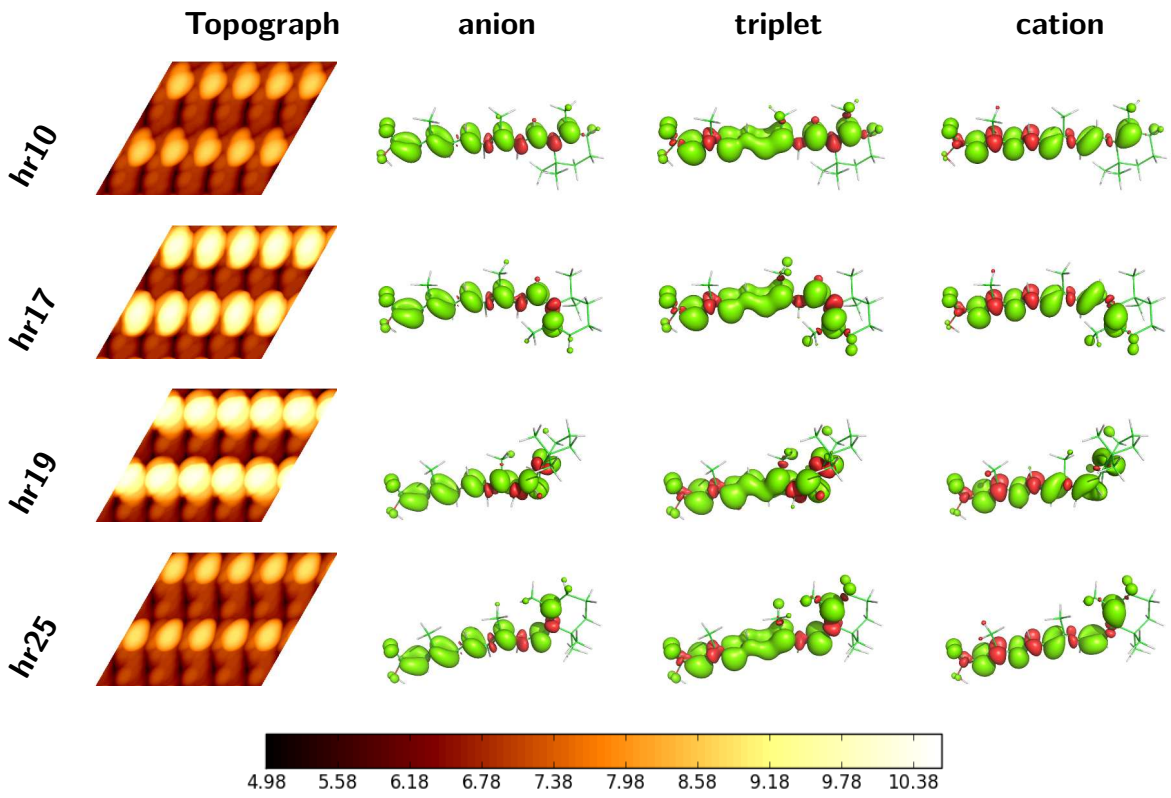

Figure 5.5: *Simulated STM topographs and differential spin densities (ρ^{α} - ρ^{β}) of the representative adsorption geometries hr10, hr17, hr19, and hr25. The STM topographs are calculated at DFTB level of theory, whereas the spin densities of adsorption geometries were calculated in the gas phase with DFT.*

resemblence to the members of group one and two. However, this is the only exception apart from which the STM images obtained for each group are consistent highlighting the similarity between the contained isomers. A tentative conjecture at this point would be to assign the non-switched isomer **N** to group one and the switched isomers **Y**, **B**, and **O** to groups two and three. This assumption will be further adressed for selected isomers in a full DFT description in section 5.3.

In Figure 5.5 the differences in spin density ρ^{α} - ρ^{β} of four adsorption geometries are shown. This quantity was calculated with TURBOMOLE following the same method employed in Chapter 4 and aiming at elucidating whether the conformational distorsion caused due to the adsorption of the molecule on the surface leads to the stabilization and therefore localization of single spins (for further images compare Appendix B.2, Figure B.1 to B.3). This quantity could potentially yield important informations towards the origin of the observed Kondo-effect, which were not observed in the gas phase calculations, since the now investigated geometries were obtained including the constraints imposed by the metal surface. Indeed, a small shift in unpaired electron density of the cationic and triplet states towards the ring group is observed, which is especially prominent in the case of geometries involving the tilting and twisting of the cyclohexene-moiety. In this case, the flat conjugated system is distorted and this disturbance in the aromatic system potentially leads to a higher propability of localized unpaired spin density. This important finding suggests that the geometries assigned to group three are more likely to develop a Kondo-effect compared to non-distorted ones. In analogy to the results presented in Chapter 4, also the differential total density $\rho_{i}^{tot} - \rho_{singlet}^{tot}$ was analyzed for the anionic, cationic and triplet occupation. However (as can been seen in Appendix B.2) the difference in total density is very similar in each of the cases calculated.

The observations based on the simulated STM images suggested a tentative assignment of the experimental observations **Y**, **B**, and **O** to different isomers contained within groups two and three on the grounds of the brightness of the protrusion associated with the cyclohexene-moiety. However, the relative orientation of the conjugated chain towards the ring system as observed in the experimental STM topograph in Figure 1.1 highlights a peculiar feature, namely a slightly bent orientation of the polyene chain towards the carboxy group of the second monomer in the dimeric arrangement. By comparison of the Tersoff-Hamann simulations based upon the LDOS obtained from the DFTB-calculation, this geometric detail is not observed within the majority of the presented topographs in Appendix B.2. In all these calculations (and in contrast to the experiment) only single adsorbate geometries were considered, although it seems possible that the experimentally observed bending might

Table 5.2: *Geometrical change occuring during the optimization of dimeric structures. By measurement of the angle γ between the atoms designated by spheres in the image to the left, a qualitative measurement of chain-bending can be obtained. γ_0 designates the angle of the starting geometry and γ_{M1}, γ_{M2} are the angles of monomer one and two within the dimeric arrangement.*

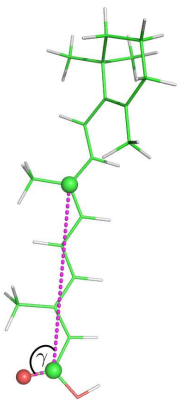

group	ID	γ_0 [deg]	γ_{M1} [deg]	γ_{M2} [deg]
①	hr10	129.5	127.8	124.5
②	hr25	129.3	128.2	126.5
③	hr17	129.2	121.5	124.9
③	hr19[1]	124.4	128.0	128.4
③	hr20	127.2	124.8	125.0
③	hr23[1]	124.3	126.1	129.3

[1] Bending already observed in monomer STM simulation.

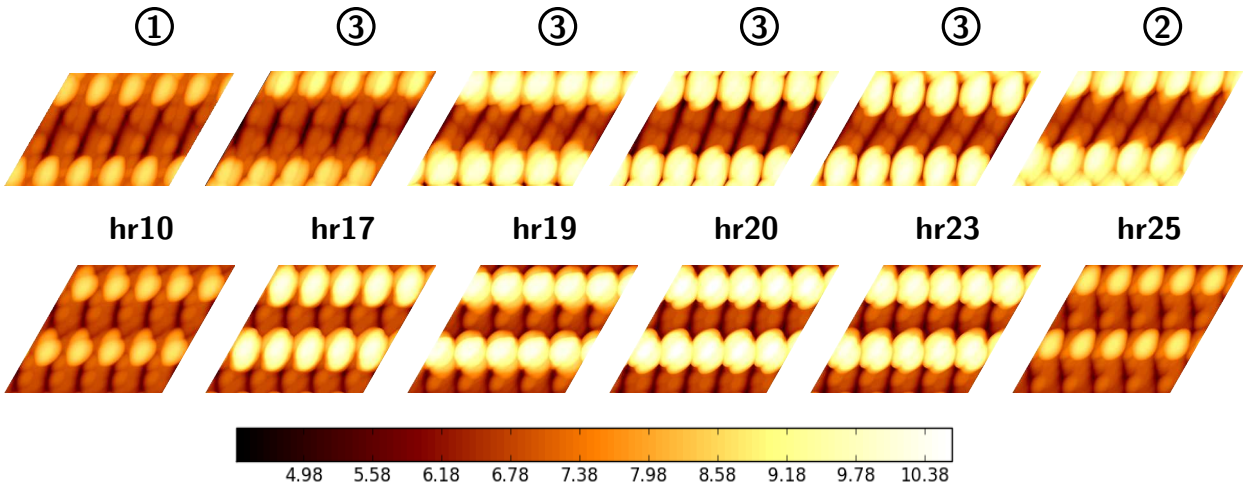

Figure 5.6: *Simulated STM topographs for selected dimers (upper row) in comparison with the images of the monomeric simulations (lower row)*

arise due to the interaction of two molecules arranged as shown in Figure 1.1. This arrangement of molecules including the bent polyene chain was reproduced for a free standing overlayer of molecules as reported earlier [19]. In order to reproduce this effect on the Au(111) surface, typical geometries of group two and three were optimized in a periodic system of repeating dimers. Table 5.2 lists the angle γ obtained after the geometry optimization of selected isomers in dimeric arrangements on the surface. Apart from hr19 and hr23 (which already had shown the geometric feature discussed above after optimization in the monomeric case), the value of the angle decreases from the initial value, which can be interpreted as a buckling of the carbon chain due to the mutual geometric rearrangement of the carboxy functional groups. Further internal coordinates of the optimized dimers are listed in Table B.2 (Appendix B). In Figure 5.6 the Tersoff-Hamann images of different optimized dimers are compared. Two properties are remarkable: First, the geometric feature of the chain described above is the result of the interaction of the carboxyl-groups and leads to a regular arrangement of the polyene chain, which is also visible in the simulated STM topographs (Figure 5.6). Hence, it might be assumed that also other monomer geometries obtained from the computational screening are prone to the same chain bending due to dimerization. Therefore the absence of this geometrical feature in the STM topographs is not to be considered a rationale to exclude them from further investigations. Furthermore, by comparing the simulated STM topographs of the dimers with those of the corresponding monomers (Figure 5.6), in the case of hr25 a discrepancy in brightness of the protrusion associated with the ring system is observed. This detail arises due to the different type of interaction between dimers, namely the cyclohexene groups allowing a stabilization not expected when only considering a monomeric arrangement as simulated before.

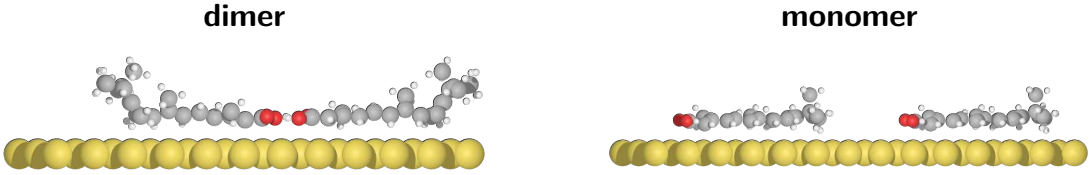

Figure 5.7: *New geometrical features arising due to optimization of dimers, exemplary shown by the dimeric structure of monomer-conformation hr25. The tilted ring geometry is believed to occur due to the interaction with a second cyclohexene-moiety of a surrounding repetition unit in the periodic lattice.*

In Figure 5.7 the side-view of the optimized dimer-geometry of monomer-conformation hr25 shows that the value of angle α between the surface and the ring group has largely increased. The upwards tilted ring feature might be stabilized due to the proximity of the cyclohexene-moiety with another repetition unit in the periodic lattice. This leads to the conclusion that tightly packed dimeric structures have more possible different conformations than their respective monomeric counterparts (shown on the right side of Figure 5.7). However, the observed experimental switching is not restricted to the dimeric arrangement of retinoic acid but was also observed in the other adsorption patterns on Au(111) [24], which include star-shaped pentameric and tetrameric arrangements of different surface coverage [19]. These arrangements do not necessarily involve two neighboring cyclohexene-moieties which leads to the conclusion that the additional conformations arising due to dimerization can explain the different appearances of measured and simulated STM images, but are not crucial for the identification of the switched geometries of ReA on Au(111).

5.3 Retinoic Acid on Au(111) from a DFT perspective

By the computational screening procedure described in the previous section three classes of different adsorbate conformations were identified, namely **all-trans**, **cis-switched**, and **dimethyl/methyl-switched**. Four representative geometries of those groups (Figure 5.8) were chosen for full DFT investigations using the introduced vdW^{surf} embedding model with two layers of constrained, explicitly treated gold atoms. The isomer hr10 (**all-trans**) likely corresponds to the non-switched *off*-state **N**. The remaining three distorted geometries (hr17, hr19, hr25) are possible candidates for the observed switched states (**Y**, **B**, **O**) on the surface[1]. The internal coordinates of the (DFT) optimized isomers are listed in Table 5.3 along with the adsorption energy of each conformation (in parentheses the intermolecular contribution of the dispersive long range interaction is given). A top view of the adsorption geometries of all isomers is shown in Figure 5.8.

The optimized **all-trans** (hr10D) isomer is adsorbed flat on the surface without any tilting, i.e., the angle α between the surface facet and the carbon atoms at the onset of the conjugated chain is 5.3 degrees. No twisting is observed, as shown by the dihedral angles Φ_1 and Φ_2 of the carbon chain being close to 180 degrees, which corresponds to a trans-configuration. Furthermore, the ring system is coplanar with the chain and an almost regular hexagon with the dihedral angle Ψ_1 between the π-conjugated atoms of the ring and the atoms in the chain closely approaching 180 degrees and Ψ_2 approaching the ideal value of 360 degrees. The conjugated chain is approximately

Table 5.3: *Internal Coordinates and adsorption energy* E_{ads} *of DFT-optimized isomers hr10D, hr17D, hr19D, and hr25D. The internal coordinates are identical with those defined in section 5.2, Figure 5.2. Additional parameters are the average adsorption height* ϕ*, which was defined as the c-component of the center of mass of the adsorbate above the metal facet.* d^c_{max} *is the c-component of the highest atom above the surface and* d^c_{ring} *is the center of mass of the cyclohexene ring above the surface.*

coordinate	hr10D	hr25D	hr17D	hr19D
group	① **all-trans**	② **cis-switched**	③ **dimethyl-switched**	③ **methyl-switched**
Ψ_1 [deg]	172.3	317.1	317.9	299.2
Ψ_2 [deg]	345.7	142.9	142.0	126.0
Φ_1 [deg]	178.6	353.7	163.1	342.1
Φ_2 [deg]	177.9	173.9	187.5	177.1
α [deg]	5.3	17.4	27.3	-27.3
θ [deg]	18.3	29.1	23.1	29.8
$d_1^{O\|Au}$ [Å]	3.1	3.0	3.1	3.0
$d_2^{O\|Au}$ [Å]	3.5	3.3	3.7	3.1
ϕ [Å]	3.5	3.6	4.0	4.2
d^c_{max} [Å]	6.1	6.2	7.6	8.0
d^c_{ring} [Å]	3.8	4.0	5.1	4.9
E_{ads} [eV]	1.71 (0.75)	1.23 (0.60)	1.22 (0.62)	0.88 (0.45)

[1] To distinguish the geometries optimized with DFTB (previous section) and those optimized with DFT in this section, the suffix D (for DFT) was appended.

20 degrees (θ) inclined towards the Au-Au orientation and most carbon atoms preferably located on *bridged* positions between surface atoms. The adsorption distance shows a slight gradient from the carboxy-end of the chain towards the ring system and lies between 3.1 Å of the lowest oxygen atom and 6.1 Å of the highest hydrogen atom. The c-component of the center of mass of the ring system places it very close to the surface, with a distance of 3.8 Å, which is only 0.3 Å above the center of mass of the whole molecule above the surface. It is known that pure hydrocarbons usually adsorb due to dispersive interactions contributing to the attractive forces on Au surfaces [63]. In the case of the **all-trans** isomer these contributions sum up to 40% of the total adsorption energy (1.71 eV). The adsorption energy is suprisingly low for a large flat adsorbate compared to the values of the much smaller molecules benzene (0.74 eV [67]) and E-azobenzene (1.44 eV [68]). This might be due to the not perfectly flat geometry of the saturated ring system and because the additional methyl-substituents on the ring and on the chain prohibit the adsorbate to further approach the surface. The average adsorption height (3.5 Å) lies 0.5 Å above the value for benzene (3.05 Å [67]) and E-azobenzene (2.98 Å [68]).

The **cis-switched** (hr25D) isomer shares a lot of similarities with the **all-trans** adsorption geometry, however, the composition of the ring system is already distorted with the angles Ψ_1 and Ψ_2 differing by 40 degrees from the **all-trans** values and the ring system lifted up from the surface by 17.4 degrees. This explains the increased average adsorption height of 3.6 Å of the molecule and 4.0 Å of the cyclohexene ring. A remarkable detail is the lower adsorption height of the oxygen atoms compared to the **all-trans** configuration, due to the cis-oriented bond ($\Phi_1 \simeq 360$ degrees) being less sterically constrained and therefore facilitating the interaction between the π-electrons and the surface. This stronger bonding interaction between the cis-bond and the metal surface also lead to a buckling of the polyene chain, resulting in the C-19 methyl group to protrude upwards. The positions of the carbon atoms again preferably occupy *bridged* positions between Au atoms. The large inclination of the carbon chain towards the Au-Au bonds ($\theta = 29.1$ degrees) is rationalized by the presence of the cis-oriented bond. The average position of the ring system (4.0 Å) and the highest position of an atom above the surface (6.2 Å) are slightly increased compared to the **all-trans** isomer. Because the system is mainly interacting via physisorption, the increased distance from the surface is reflected by the lower adsorption energy of 1.23 eV. Of all four investigated on-surface geometries, the **cis-switched** and **all-trans** isomers are most similar and therefore expected to show the least differences in the appearance of their simulated STM topographs.

The **dimethyl-switched** (hr17D) isomer is almost identical to the **cis-switched** isomer, though with two important differences: first, the conjugated polyene-chain only contains bonds in trans-configuration, and secondly, the ring system is skewed by 90 degrees in comparison to the chain which leads to a large increase in average adsorption height of the cyclohexene group (5.1 Å) and an angle of almost 30 degrees between the surface and the flat adsorbed chain ($\alpha = 27.3$ degrees). Furthermore, the highest adsorbate atom is located 7.6 Å above the surface facet. The upright positioning of the ring system lifts the whole molecule as if a wedge was inserted between the surface and the ring. It leads to an increased average adsorption height of 4.0 Å and even lifts one of the oxygen atoms up to 3.7 Å. This twisted ring conformation is stabilized by the dimethyl group being arranged

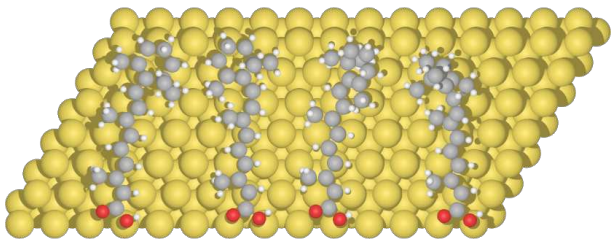

Figure 5.8: *DFT optimized adsorption geometries of (fltr)* ***all-trans****,* ***cis-switched****,* ***dimethyl-switched****, and* ***methyl-switched*** *conformations. The carbon atoms prefer bridged positioning on the surface and the inclination angle between the Au-Au orientation and the molecule is either 20 or 30 degrees.*

on the surface similar like a trestle. In conjunction with the surface-attracted polyene chain being fixed in a structure best described as tripodal, the molecule cannot tumble. This stable conformation is also underlined by the high adsorption energy of 1.22 eV compared to the **cis-switched** isomer (which is much less lifted from the surface), despite its disadvantageous conformation.

The **methyl-switched** (hr19D) isomer is also stabilized in a tripodal arrangement, however the three legs are all different: the single methyl-substituent of the ring system, the first methyl-substituent on the conjugated chain (C-19), and the C-4 carbon inside the ring system. The special arangement requires the carbon chain to buckle away from the surface (α = -27.3 degrees) and stabilize this loop via formation of a cis-bond at C-7 ($\Phi_1 \simeq 360$ degrees). Nevertheless, the strong attraction between the remaining polyene chain and the metal surface keep the molecule attached in a distance of 3.0 and 3.1 Å at the carboxy group and an average height of the whole adsorbate of 4.2 Å. The buckling of the molecule leads to one of the methyl-substituents on the C-1 carbon being the uppermost atom of the adsorbate with a maximum height of 8.0 Å. In compliance with all other adsorption geometries, *bridged* postions of the carbon atoms are preferred. Similarly to the **cis-switched** isomer, the molecule is inclined by nearly 30 degrees in comparison to the Au-Au orientation. The chain buckeling of this isomer reduces the effective cross section of the molecule with the surface, which explains the large decrease in adsorption energy (0.88 eV).

The conclusions which can be drawn from the obtained internal coordinates are that the average position of the molecule is shifted away from the surface facet if the ring system is twisted, but one oxygen atom of the carboxy functional group acts as an anchor to keep the molecule on the surface, whereas the second oxygen atom can also be lifted by up to 0.6 Å (isomer **dimethyl-switched**). This is not only observed by the change in adsorption height of the oxygen atoms but also by the change in the c-component of the center of mass (designated ϕ in Table 5.3) and the drop in adsorption energy of all isomers compared to **all-trans**. These findings prove the initial assumption of our experimental collaborators [24] that the ring system is lifted due to switching of the molecule to be correct. It furthermore explains the increase in brightness at the cyclohexene-moiety, whereas the remaining conjugated chain is partially immobilized due to the carboxy functional group and does therefore not change in intensity upon switching.
It is remarkable that the adsorption energy is made up by a large part of dispersive interaction (40-50%) and the contribution increases by uplifting the chain. This confirms the initial presumption of the molecule primarily interacting via physisorption. In addition, the asymmetric anchoring effect observed here does also not vanish if two retinoic acid molecules are optimized on the surface as might be suspected due to mutual stabilization of the hydrogens of both carboxy functional groups, which was confirmed using the results obtained through DFTB optimizations of dimers (cf. App. B, Tab. B.2). In general, the geometries optimized on the full DFT level (Table 5.3) agree very well with the corresponding DFTB results (Table B.1): For d_1 and d_2 the typical deviation (with

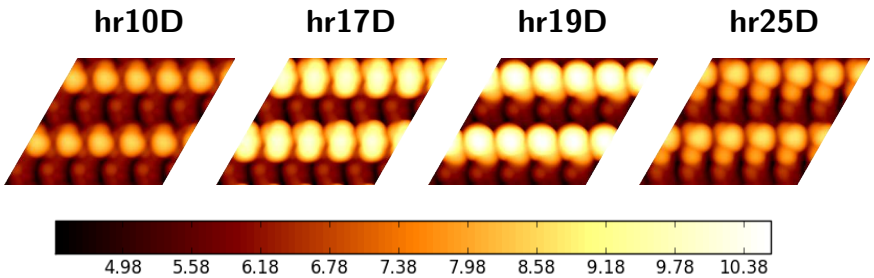

Figure 5.9: *Simulated STM topographs of* ***all-trans*** *(hr10D),* ***dimethyl-switched*** *(hr17D),* ***methyl-switched*** *(hr19D), and* ***cis-switched*** *(hr25D) based on DFT calculations*

the exception of hr17D where it is 0.5 Å) from the DFT values is 0.1 Å (3%), while for example for Ψ_1 deviations range from 11 - 24 degrees (6-7%). This shows that sufficient results can already be achieved on the DFTB level and that, in general, the results obtained in section 5 seem trustworthy.

In a final step, STM images are simulated with DFT in order to verify the DFTB results from section 5. In Figure 5.9 the Tersoff-Hamann simulation of STM topographs of the DFT calculations are shown. It can be concluded from these images that those twisted geometries with the methyl-substituents in an orientation towards the surface lead to STM topographs with increased brightness of the ring system. An interesting detail is that a distinct difference is observed between the methyl-adsorption (hr19D, circular symmetric protrusion), and dimethyl-adsorption (hr17D, oval pattern). The major influence of the cis/trans isomerization is not a different orientation of the conjugated chain but an increase in brightness of the first segment on the chain. This happens because the stronger bonding interaction between the cis-bond and the surface forces the polyene chain to buckle, resulting in the C-19 methyl-group to protrude vertically. It is remarkable, that this methyl-moiety is distinguishable from the bigger protrusion corresponding to the cyclohexene-ring. Figure 5.10 shows the simulated monomer STM topographs of the final DFT calculations in comparison to the real experimental data. An artificial side-to-side arrangement of monomers is produced on the right side to allow an easier comparison of the different protrusions. Following this comparison, the protrusions of isomer hr19D suit the experimental state **O** best. These STM simulations compare well with the rolling-ball enhanced images of the DFTB-simulations, validating this method as a good first guess towards the appearance of the final DFT-simulated topographs. However, certain details such as the appearance of a distinct second protrusion in the **cis-switched** isomer is easily overlooked because smoothed out using the rolling-ball algorithm.

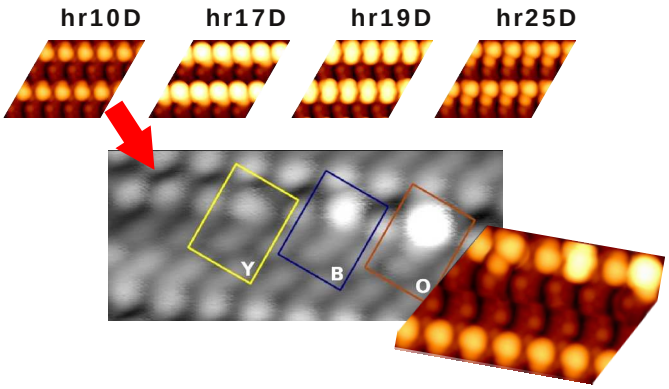

Figure 5.10: *Graphical reconstruction of the experimental topograph with monomers. The Tersoff-Hamann simulated STM topographs of retinoic acid isomers **all-trans** (hr10D), **dimethyl-switched** (hr17D), **methyl-switched** (hr19D), and **cis-switched** (hr25D) are artificially assembled to mimic a similar pattern as observed in the experiment in order to ease the comparison in relative size and shape.*

5.4 Summary and Conclusion

In this chapter retinoic acid adsorbed on a Au(111) surface was investigated using DFTB and DFT, focusing on the identification of the geometric and electronic conformations that correspond to the switched (Kondo) states observed experimentally.

In a first step, a set of 122 initial geometries was optimized on a Au(111) surface slab, combining DFTB with the van-der-Waals embedding described in Chapter 3. The such obtained geometries were then systematically classified, leading to three groups of most likely conformations occuring on the surface. The principle approach was to choose a representative number of internal coordinates which fully describe the adsorbed molecule and to analyze whether or not after optimization on the surface and excluding physically unsatisfactory results, a preference for certain values of these internal coordinates is observable. This was facilitated by the usage of Kernel Density Estimations,

which transform a set of discrete values into a continuous function of the internal coordinate, giving a measure of its relative frequency at each chosen position. Peaks in this distribution function correspond to preferred values of the internal coordinate - similar to a histogram but not restricted to discrete intervals. The application of this method led to 18 potentially interesting geometries which can be classified into three groups: The first group consists of very similar conformations of flat-adsorbed all-trans geometries, the second group contains cis/trans isomers, and the third and most inhomogeneous group contains changes in conformations due to tilting and twisting of the cyclohexene-moiety. Spin-polarized calculations performed on the isolated molecules indicated, that the third group holds the most promising candidates to stabilize unpaired spin density. Furthermore, the simulated STM topographs exhibit very bright features compared to the corresponding images from groups one and two. This led to a first tentative conclusion that the unswitched ReA conformation might be found in group one, while group three might contain the switched isomers. By optimization of dimeric arrangements of selected conformations, additional geometric features, such as an increase in the angle α between the molecule and the surface were observed which are ascribed to the interaction between adjacent cyclohexene-moieties from neighboring unit cells in the periodic lattice. The relative brightness of the main protrusions in the dimeric structures between different groups follows the trends for the monomers. Therefore, and due to the fact that the switching ability of surface-adsorbed retinoic acid was also observed for pentameric and tetrameric arrangements on the surface (which do not include neighboring ring systems), it was concluded that these geometrical features do not play a predominant role in the search for a conformation which may stabilize unpaired electrons.

The screening approach described above has proven to be a versatile and systematic way of adressing the problem of finding the adsorption geometries of large adsorbate molecules on a metal surface. Instead of relying on chemical and physical intuition alone for an educated guess about the adsorbate geometry, it is possible to screen many different conformations, thus introducing statistics as an additional tool in refining the initial guess before a more in-depth evaluation of the system is performed. In this stepwise approach the accuracy of the employed methods can be increased constantly while at the same time reducing the amount of treated geometries. Furthermore, due to the fact of that DFTB is derived from DFT and fitted upon results obtained from DFT calculations, a method was chosen to preoptimize the given system at little computational effort while still reliably predicting many properties such as the geometry on the surface and allowing the evaluation of observables such as Tersoff-Hamann simulations of STM topographs, which facilitate to interpret the impact of changes in molecular rearrangement on their appearance in STM images. In addition to observables obtained directly from the calculations performed in the screening approach, the obtained adsorbate conformation can be used to study the influence on equilibrium geometries arising due to the surface imposing certain constraints on the internal coordinates of the adsorbate molecule. These geometries can be studied by advanced DFT calculations without the surface in the form of a constrained free molecule, giving an insight into the consequences of molecular distortion upon the electronic structure. The sum of these informations can then be used to select certain representative conformations of this preliminary screening and use them in DFT calculations. By the application of this screening methodology, it can be assured that the subsequent DFT calculations will be performed on a representative data set.

One section of this chapter was dedicated to DFT calculations, studying which geometrical details arise if four selected isomers (**all-trans**,**dimethyl-switched**, **methyl-switched**, and **cis-switched**) of retinoic acid are optimized on the metal surface using full DFT with the van-der-Waals approach described in Chapter 3. The results of these calculations suggest that geometrical switching leads to a partial lifting of the molecule, especially prominent around the ring system, whereas one oxygen atom acts as an anchor to keep the molecule attached to the surface. Nevertheless, the adsorption

energy decreases rapidly due to the change in adsorption height, which is characteristic of a system primarily interacting via dispersive interactions. The physisorbed bonding is highlighted by the rather large (40-50%) part of the total adsorption energy provided via intermolecular dispersive interaction, which increases if the molecule is lifted up.
The simulated STM topographs allow a comparison with the original experimental data. It was shown that the shape and brightness of the **methyl-switched** isomer matches those of the switched state, whereas the **all-trans** isomer likely corresponds to the non-switched state. Thus, by combining existing DFTB and DFT codes with the newly implemented van-der-Waals embedding, it was possible to identify conformations matching the experimental STM features even for an organic adsorbate as large and complex as retinoic acid.

Chapter 6

Conclusion and Outlook

Established assembly techniques come to a natural limit when it comes to manufacturing smaller and smaller electronic devices. A possible solution is to go down to the molecular level and use single molecules as functional units. Among the most basic building blocks are switches; molecules with switching capability therefore attract great interest. Only recently our experimental collaborators have shown that retinoic acid adsorbed on Au(111) can be reversibly switched with an STM tip by application of a negative bias voltage, leading to different appearant heights in the STM topographs in vicinity of the cyclohexene-ring [24]. Intriguingly, dI/dV curves of these states show a Kondo feature, suggesting the presence of an unpaired spin in the switched states. From experiment alone it is not possible to identify the corresponding adsorption geometries and to explain the observed Kondo-effect. The goal of the present work was to identify the geometry and electronic structure of the switching intermediates from first-principles calculations in order to justify the experimentally observed changes using a molecular model.

To study the correlation between geometry and electronic structure isolated ReA molecules ("gas phase") were investigated in a first step using density functional theory and Coupled Cluster Approximates Doubles (Chapter 4). For this purpose, the geometries of four cis/trans isomers were optimized in different electronic configurations, including anion, cation, triplet and singlet states. A comparison of the relative energies revealed that for each of the four electronic configurations **x** (the crystal structure ReA) is most and **hzat** (multiple switched bonds) least favored. For the latter the DFT calculations showed that the electronic structure and the geometry of the molecule are correlated, i.e. that the optimized geometry depends on the given electronic configuration.
Analysis of the frontier orbitals with DFT and Coupled Cluster Approximate Doubles (CC2) led to the conclusion that due to the delocalized character of most orbitals, most of them could be assigned to the experimental observation, however only the HOMO orbitals of a cation are probed by a negative bias voltage and would qualify to explain the appearance of the (non-switched) STM topograph. The gas phase study could not provide an explanation for the Kondo-effect, i.e., the localization of an unpaired electron spin: This was attempted by calculation of the differential spin density $\rho_\alpha - \rho_\beta$, which showed a delocalized spin density distribution in the conjugated π-system for each of the observed states, independent of the differences in gas phase geometries. Furthermore, the addition or removal of an electron as simulated by vertical transitions showed that in a cationic species a localized rearrangement of electron density occurs. However, as this quantity is calculated from the total electron density, the information about the spin localization is lost. It was concluded that while the gas phase simulations gave a first understanding of the electronic and geometric structure of retinoic acid, they could not provide an explanation for the experimental observation. This led to the assumption, that the metal support played an important role and therefore had to be included in the simulation.

Unfortunately, the inclusion of a metal support drastically increases the computational requirements of the simulation. Therefore, a new embedding scheme was developed and implemented (Chapter 3): It treats only a few metal layers (and the adsorbate) explicitly with DFT. Those are embedded in a vdW^{surf} description of the whole system, which accounts for long-range interactions using a pairwise potential interaction. This is especially suitable in the study of this system due to Au(111) predominately interacting by physisorption with organic adsorbates [63]. The embedding scheme was implemented within the Atomic Simulation Environment (ASE) and tested upon the applicability to organic adsorbates on a Au(111) and Pt(111) surface. It was shown that the geometry and adsorption energy of a benzene molecule on a Au(111) surface, i.e., a physisorbed system, reach convergence by including only two layers of metal treated within DFT. Also the geometry of benzene on the Pt(111) surface converged with only two layers of metal, but additional layers are needed to calculate the adsorption energy on this kind of chemisorbed systems. It was concluded, that two layers of Au(111) are the minimal requirement to simulate retinoic acid on the Au(111) surface if additional ten layers are included in the description of the long-range dispersive interaction. Typically, DFT calculations of this kind of systems are performed using four- or even six-layered metal slabs, meaning that the computational costs can be reduced tremendously by using the newly implemented van-der-Waals embedding approach.

Due to the many internal degrees of freedom in the retinoic acid molecule, a computational screening approach was chosen to identify the most probable adsorption geometries associated with the change in contrast of the protrusions observed in the experiment. A library of different starting geometries was generated from selected internal coordinates and optimized on a periodic surface of Au(111) using dispersion-corrected density functional tight binding with a customized parameter set, allowing the simulation of an organic adsorbate containing oxygen on a Au surface. The calculations were performed with the newly implemented embedding scheme using the DFTB-code Hotbit [54] and the vdW^{surf}-dispersion correction [50]. The results of the optimizations were statistically analyzed and led to the identification of 18 out of originally 122 potential adsorbate geometries. These 18 geometries were classified in three different groups: The first group contained only all-trans isomers, whereas the second group listed all geometries with a bond in cis-configuration. The third group involved geometries with twisted and tilted ring systems. DFT calculations for the such obtained geometries in gas phase were performed. The analysis of the corresponding differential spin densities $\rho_\alpha - \rho_\beta$ showed that geometries with distorted aromatic systems were able to localize unpaired electron spin.
In the next step, enhanced (gaussian-smoothed rolling-ball) Tersoff-Hamann simulations were performed to obtain STM images of the adsorbate geometries. The simulation of STM images identified the cyclohexene-moiety as a bright protrusion when the ring system is twisted, which explains the experimental STM topograph on the grounds of changes in geometry. In addition to the adsorption of single molecules on the surface, also dimeric arrangements were considered, which allowed to reproduce the dimeric pattern observed in the experimental STM topographs by comparison to the simulations for all tested conformations.
On the basis of the STM image and the differential spin density, four representative geometries were chosen to be studied by full DFT calculations using the newly developed embedding model and the all-electron code FHI-AIMS. The results of these calculations have shown that the experimentally observed switched states are most likely associated with the ring system being lifted from the surface, whereas the carboxy group and the conjugated chain act as an anchor to keep the molecule attached to the surface. The shape and brightness of one observed isomer (**methyl-switched**, cf. Figure 5.9) matches those of the experimentally switched states and the STM image of the **all-trans** isomer resembles the non-switched state.

Thus, it was shown that the newly implemented embedding scheme is capable of correctly describ-

ing the metal-organic interface for physisorbed systems even for large organic adsorbates, because the computational cost is reduced significantly with only minor loss in accuracy compared to the full DFT treatment. This advantage was used in this thesis in conjunction with a computational screening approach to identify the most probable adsorbate geometries corresponding to the switched and un-switched states of retinoic acid on Au(111). However, the results presented here cannot provide full, conclusive explanations for the experimentally observed Kondo-effect. These could be provided in a next step (which goes beyond the scope of this thesis) using full spin-polarized calculations on a constraint-DFT level.

Appendix A

Further details of implementation

A.1 Documentation of qmme.py and dftdisp.py interface

During the course of this thesis, the ASE-calculator modules qmme.py and dftdisp.py were implemented as introduced in Chapter 3. This chapter will briefly introduce how to use these modules and serves as a documentation of the input routines.

A.1.1 dftdisp.py

The ASE calculator dftdisp.py replaces all input routines of the CASTEP fortran-module [71] upon which it is based whilst still keeping the names of the internal variables in order to lessen confusion. A sample input of dftdisp.py would look like this:

```
1
2  """
3  This is a sample input script for the dftdisp.py calculator within ASE assuming
4  a predefined geometry of an adsorbate counting 50 atoms.
5  """
6
7  from ase.calculators.dftdisp import dftdisp
8  from ase.io import read
9
10 slab = read('sampleinput.xyz')
11
12 calc_vdw = dftdisp(sedc_print_level=3,
13         sedc_scheme='TS-SURF',
14         sedc_n_groups=2,
15         sedc_pbc_g_only_intra=[0, -1],
16         sedc_groups=[50, slab.get_number_of_atoms() - 50],
17         sedc_pbc_g_switches=[[1, 1, 0, 1, 1, 0],
18                              [1, 1, 0, 1, 1, 0]],
19         sedc_tssurf_vfree_div_vbulk=[1.00, 1.00, 1.00, 0.9452],
20         sedc_do_standalone=True)
21
22 slab.set_calculator(calc_vdw)
23 slab.get_potential_energy()
24 slab.get_forces()
```

Listing A.1: Sample input of the dftdisp.py interface implemented in ASE

Table A.1: *Input keywords of the dftdisp.py calculator. Additional development parameters are available and documented within the code.*

Parameter	Usage
`sedc_print_level`	Switch to control the verbosity, possible values range from 1-5. Default = 3.
`sedc_scheme`	Specifies which scheme should be used in the calculation. The implemented choices are OBS [102], G06 [103], JCHS [104], TS [49], and TS-SURF [50]. The default value is TS.
`sedc_n_groups`	Number of logical groups in the model, i.e. two in case of an adsorbate and a substrate.
`sedc_pbc_g_only_intra`	Boolean switch to deactivate the intra-group dispersive interaction. When set to `True` = -1, then the dispersive interaction within this group will be discarded.
`sedc_groups`	List of integers which specify the number of atoms within each group in ascending order of the atom definition in the ASE Atoms-object.
`sedc_pbc_g_switches`	List of `sedc_n_groups` lists specifying whether or not the dispersion interaction is turned on along that coordinate [-x, -y, -z, +x, +y, +z].
`sedc_pbc_g_cells`	List of cell definitions for each group within the molecule (i.e. allowing different periodicity of adsorbate and bulk material). This parameter is overwritten if used within qmme.py and defaults to the cell of the ASE Atoms-object if omitted.
`sedc_ts_veff_div_vfree`	Hirshfeld partitioning ratio obtained from DFT calculations. If used in conjunction with qmme.py these values are assigned automatically. If not available defaulting to 1, TS and TS-SURF schemes only.
`sedc_tssurf_vfree_div_vbulk`	List of floating point scaling coefficients arising due to the TS-SURF scheme being based on bulk atom volumina, whereas the initial TS scheme was based on the volume of free atoms. For more details on this see [68].
`sedc_do_standalone`	Boolean switch, if `True`, the module is called in standalone-mode whereas the default `False` is used if called in conjunction with another QM-calculator.
`logfile_name`	Name of the logfile written by the dftdisp.py module.
`sedc_pbc_force_tol`	Force convergence criterion, defaulting to 1e-7 eV/A
`sedc_pbc_energy_tol`	Energy convergence criterion, defaulting to 1e-6 eV
`sedc_do_pbc`	Boolean turning the periodic calculations on (-1) or off (0), turned on by default.

`sedc_xc` Name of exchange-correlation functional the chosen dispersion scheme is applied with. Choices are different for each scheme and the default set to PBE.

scheme	exchange-correlation term
OBS	PZ81, PW91
G06	PBE, BLYP, BP86, B3LYP, TPSS
JCHS	PBE, BLYP, B3LYP, TPSS
TS	PBE, RPBE, PBE0, BLYP, B3LYP, AM05
TSSURF	PBE, RPBE, PBE0, BLYP, B3LYP, AM05

The dftdisp.py ASE calculator can in principle be used as a standalone calculator as well as within the embedding-model calculator qmme.py. It is however designed to be used in conjunction with the embedding, which facilitates certain tasks such as the rescaling of C_6^{AB} coefficients in the TS and TS-SURF scheme with the Hirshfeld-ratios obtained from QM-calculators. At the present time, this functionality is provided by the FHI-AIMS and CASTEP calculators in ASE, whereas both of these calculators have to be configured to calculate the Hirshfeld partitioning, triggered by the settings `output=['hirshfeld']` for FHI-AIMS and `iprint=2, calculate_hirshfeld=True` in CASTEP, respectively.
Additional internal variables of the fortran-module are available under their designation in the source code and listed in the calculator-interface within ASE. The original code in `semp_disp_corr.f90` [71] was developed by E. McNellis, J. Meyer, and K. Reuter and published under the LGPL v3.0 and above[1]. The code was used and modified with permission of the authors (K. Reuter).

A.1.2 qmme.py

The ASE calculator qmme.py is the implementation of the embedding model introduced in Chapter 3. The module was designed in a very general way to allow the usage of an arbitrary number of calculators for the explicitly treated region as well as the dispersive region, both of which are allowed to overlap. Additionally, a different cell definition can be supplied to each region allowing to treat the adsorbate and the surface in a different periodicity, hence simulating variable adsorbate arrangements and coverages. At the moment both the calculation of forces and the potential energy are supported. Due to the special usage case presented within this thesis, some specific features such as the automatized handling of rescaling of C_6^{AB} coefficients within the dispersion schemes TS and TS-SURF (*vide supra*) are implemented as well but ignored if used with calculators not meant to apply to this application scenario. Due to the very generic implementation, this module can be easily tailored to serve as the backbone of other embedding or QMMM methodologies. A sample input structure of qmme.py is shown in Listing A.2.

```
1
2  """
3  This is a sample input script for the qmme.py calculator within ASE assuming
4  a predefined geometry of an adsorbate counting 50 atoms.
5  """
6
7  from ase.calculators.qmme import qmme
8  from ase.calculators.aims import Aims
9  from ase.calculators.dftdisp import dftdisp
10 from ase.optimize import BFGS
11 from ase.io import read
```

[1] The license is available from http://www.gnu.org/licenses/

```
12
13 slab = read('sampleinput.xyz')
14
15 QM1 = Aims()
16 MM1 = dftdisp()
17
18 calc_embed = qmme(atoms=slab,
19                    nqm_regions=1,
20                    nmm_regions=1,
21                    qm_calculators=[QM1],
22                    mm_calculators=[MM1],
23                    qm_atoms=[[0:71]],
24                    mm_mode='allatoms')
25
26 slab.set_calculator(calc_embed)
27 dyn = BFGS(slab, trajectory='slab2.traj')
28 dyn.run(fmax=0.025)
29 slab.get_potential_energy()
30 slab.get_forces()
```

Listing A.2: Sample input of the qmme.py interface implemented in ASE

Table A.2: *Input keywords of the qmme.py calculator.*

Parameter	Usage
`atoms`	ASE Atoms object which will be used in the embedding calculation. This object has to be specified during initialization.
`nqm_regions`	Integer of explicitly treated regions within the embedding scheme. All can have different calculators assigend.
`nmm_regions`	Integer of dispersively treated regions within the embedding scheme. All can have different calculators assigend.
`qm_calculators`	List of the calculators used in treatement of the regions of QM treatment.
`mm_calculators`	List of the calculators used in treatement of the regions of dispersion treatment.
`qm_atoms`	List of lists containing slices of atoms assigned to the `qm_calculators`. The index of `qm_atoms` and `qm_calculators` is equivalent.
`mm_mode`	String, either *allatoms*, *complementary*, or *explicit*. The latter case allows to specify the keyword `mm_atoms` to explicitly define the atoms considered in dispersive treatment, *complementary* equals to all atoms not considered in any of the `qm_calculators`.
`mm_atoms`	Same as `qm_atoms` but relating to `mm_calculators`. Only available if `mm_mode = 'explicit'`.
`qm_pbcs`	Optional list of 3x1 boolean lists specifying the periodic boundary conditions (PBC) of each molecular fragment of the `qm_atoms`. Defaults to the PBCs of the atoms object.
`mm_pbcs`	Optional list of 3x1 boolean lists specifying the periodic boundary conditions (PBC) of each molecular fragment of the `mm_atoms`. Defaults to the PBCs of the atoms object.

`qm_cell`	Optional list of 3x3 floating point lists specifying the cell definition of each molecular fragement of the `qm_atoms`. Defaults to the cell of the atoms object.
`mm_cell`	Optional list of 3x3 floating point lists specifying the cell definition of each molecular fragement of the `mm_atoms`. Defaults to the cell of the atoms object.
`logprfx`	Optional string-type argument specifying a name of the subdirectory used to store temporary files.
`hirlog`	Optional boolean argument which leads to hirarchial logging, i.e. for each calculation of each calculator a systematically named directory is created. Initially implemented as a workaround to log all data of a calculation by FHI-AIMS, primarily used for debugging.
`reuse`	If `hirlog = True`, this optional boolean value allows to overwrite existing logs.

The qmme.py calculator performs rudimentary checks if the specified initialization keywords are correct and prints error messages if values are missing, upon successful initialization a summary is printed. At the present point in time, the qmme.py module can calculate forces and the potential energy of a system and presents therefore the minimum requirements for geometry optimizations with the dynamics module within ASE. If any of the `qm_calculators` provide a value for the Hirshfeld partitioning ratio required in the TS-SURF scheme (*vide supra*), these are provided to all `mm_calculators` able to accept them.

A.2 DFTB Parameters

In Chapter 2.4 the theory behind Density Function Tight Binding was introduced and the derivation from DFT theory shown briefly. It was established in equation 2.23 that the total energy from DFTB theory is separated into three different terms, namely the band structure term E_{BS}, the Coulomb term E_C, and the repulsive energy term E_{rep}. In contrast to DFT or wave function methods, the terms are not calculated from an *ab initio* approach, but rather arise from an optimized set of parameters which originate from a DFT calculation. This chapter provides a short overview of the parameters contained, their origin, and their physical significance. This overview is based upon the work of M. Stoehr [105].

1. **Band structure E_{BS}** $(r_0, \ \{\epsilon_i\})$
   DFTB theory is conceptually expressed as a linear combination of atomic orbitals (LCAO) and focused on the valence orbitals of each species. In order to mimic the *tighter* localization of electrons around nuclei as compared to the atomic case, a confinement potential V_{conf} is applied. This potential can be approximated as:

$$V_{conf} = \left(\frac{r}{r_0}\right)^2 \tag{A.1}$$

   r_0 is the confinement radius which determines the degree of localization around the nuclei. In this work a radius 1.85 times the covalent radius of the respective atom was used. It was shown in equation 2.20, that the integral of $\langle\varphi_a|\,\hat{H}\,|\varphi_a\rangle$ in DFTB reduces to a mere sum of coefficients of two-center integrals and their respective eigenvalues in a basis set expansion of a minimal basis. These values of $H^0_{\mu\nu}$ and $S_{\mu\nu}$ (the overlap integral) are taken from a DFT calculation and stored in the Slater-Koster tables. The overlap integral $S_{\mu\nu}$ is needed in the calculation of addition or removal of electrons on each atom and is therefore also responsible for the calculation to be self-consistent in charges (SCC). It is dependent on the interatomic

distance R_{AB} and interpolated in the actual DFTB calculation from the values saved in tables. The eigenvalues have been taken from all-electron DFT calculations of the isolated atom using a LDA functional.

2. **Coulomb term E_C** $(U, \quad FWHM)$
   As shown in equation 2.21, parametrization of the coulomb interaction requires the knowledge of the Hubbard U parameters and the extra charges Δq_I and Δq_J, the latter being calculated via Mulliken orbital population analysis. Furthermore, the full-width-at-half-maximum (FWHM) value of the gaussian approximation of atomic contributions to the density fluctuation introduced in equation 2.19 is needed to calculate E_C for the heteronuclear case [54]. The Hubbard U parameter has been calculated as the difference between ionization potential and electron affinity $U = IP - EA$. These have been calculated as the energy difference between cation and anion of the isolated atom.

3. **Repulsive term E_{rep}** (r_{cut})
   The repulsive term in DFTB is used similarily to the exchange-correlation term in DFT by avoiding the analytically unknown description of many-body effects. However, in contrary to DFT exchange-correlation functionals in DFTB the *missing part* described in E_{rep} is simply the difference between the known DFT value for the energy and the DFTB-energy without the repulsive potential.

$$E_{rep} = E_{tot}^{DFT} - E_C - E_{BS} \tag{A.2}$$

   Since the repulsive potential V_{rep} is a function in dependence of the distance, the fitting process involves calculating the forces of a set of molecules at different distances and then numerically reconstructing a curve describing the ensemble of values. The repulsive potential is then given by integration of the force yielding a potential curve. In the present fitting approach the derivative of the repulsive potential was fitted to a spline function. This approach artificially corrects for all remaining interactions not considered due to the approximative nature of DFTB in comparison to DFT. However, as mentioned in Chapter 2.3, DFT lacks the possibility to account for long-range effects due to their inherent local description within most exchange-correlation functionals. In this work the repulsive potential was truncated at 3 Å.

The repulsive potentials for the metal-C,H,O parameters have been fitted to simple diatomic binding energy curves by Dr. Maurer using the DFTB-code Hotbit in the above mentioned manner. All other parameters (C, H, O, Au-Au) have been taken from [106]. Interconversion of the parameter sets allows their usage within other implementations, one of which used in this thesis is DFTB+ [58, 98].

A.3 Interconverting parameter files - hb2skf

The large system size of the investigated surface slabs prompted the need for a more efficient parallel implementation of DFTB than was available in Hotbit. The implementation of DFTB+ [58, 98] is based on a SMP-parallelized FORTRAN95 code and therefore much better suited to adress larger systems. Since both programs rely on the same underlying theory, it is possible to interconvert the parameter files from Hotbit to DFTB+. In collaboration with Dr. Maurer a script was implemented to convert the information contained within Hotbit .elm and .par files into the .skl database format used by DFTB+. The layout of the latter is based on the description of the DFTB+ file format [107].

The majority of parameters such as eigenvalues of the free atoms, the Hubbard U parameters, the atomic mass, and the neutral atom populations could be directly transferred to the DFTB+-format. A small error occurs due to the grid spacing of the Hamiltonian and overlap integral tables, which is

explicitly defined for each interval in Hotbit but has to have a fixed value width in DFTB+, therefore leading to a small numerical inconsistency, which was negligible for the here investigated system. Furthermore, the repulsive potential is defined similarily but not exactly equivalent in DFTB+, therefore the repulsive potential from Hotbit was fitted with an exponential function of the form shown in equation A.3 up to the last entry in Hotbit lower than 0.5 a_0, cubic splines until 0.4 a_0 below the specified cutoff for the repulsive potential, and fifth order splines describing the remaining 0.4 a_0:

$$V_{rep} = \begin{cases} e^{-\alpha_1 r+\alpha_2} + \alpha_3 & \text{for } 0 < r \leq 0.5\ a_0 \\ \beta_1\xi^3 + \beta_2\xi^2 + \beta_3\xi + \beta_4 & \text{for } 0.5\ a_0 < r < r_{cut} - 0.4\ a_0 \\ \beta_1\xi^5 + \beta_2\xi^4 + \beta_3\xi^3 + \beta_4\xi^2 + \beta_5\xi + \beta_6 & \text{for } r_{cut} - 0.4\ a_0 < r < r_{cut} \\ 0 & \text{elsewhere} \end{cases} \quad \text{(A.3)}$$

$$\text{with: } \xi = (r - r_p)$$

The fitting process relies on a spacing of 0.1 a_0, starting from the lowest value present in the Hotbit-repulsion and ending at the cutoff value specified in Hotbit. Testing of the obtained parameter files yielded almost exactly the same results for both DFTB+ and Hotbit. The remaining error is in the size of the numerical noise and most likely ascribed to the small fluctuations in the spacing of the Hamiltonian and overlap integral tables.

```
#!/usr/bin/python

"""
This script transforms Hotbit Parameters for specified Atoms in
Hotbit-Parameter files (*.par, *.elm) to DFTB (*.skf) files.
argv[1], argv[2] = atomic symbol (i.e. H H, C H, ..)

    usage: hb2skf C C

RJ Maurer & GS Michelitsch, Technische Universitaet Muenchen, 14/03/2014
"""

from sys import argv
from hotbit.io import native


def generate_DFTBplus_repulsion(filename, DEBUG=False):
    """
    Transforms Hotbit repulsion to DFTB+ format.
    This function generates output to be added to an .skf
    file. It outputs a string that has to be inserted
    in the right position.
    RJ Maurer, 14/03/2014
    """

    import numpy as np
    from scipy.interpolate import splrep, splev
    from scipy.optimize import curve_fit

    tmp = filename
    line = 0
    #read until the repulsion begins
    while not 'repulsion=' in tmp[line]:
        line += 1
    else:
        #skip commentary
```

```
37          line += 1
38          x, y = [], []
39          while line < len(tmp):
40              try:
41                  is_line = '.' in tmp[line].strip('\n').split()[0]
42              except:
43                  break
44              if not is_line:
45                  break
46              data = tmp[line].strip('\n').split()
47              x.append(float(data[0]))
48              y.append(float(data[1]))
49              print x[-1], y[-1]
50              line += 1
51
52      ##Repulsion is defined by an initial exponential part
53      #and a third order spline with weird knots with
54      #a 5th order spline at the end
55
56      #repulsion function is stored in x and y
57      def expfit(x, a1, a2, a3):
58          return np.exp(-a1 * x + a2) + a3
59
60      def splinefit(t, c0, c1, c2, c3):
61          x, x0 = t[0], t[1]
62          func = c0 + c1 * (x - x0) + c2 * (x - x0) ** 2 + \
63              c3 * (x - x0) ** 3
64          return func
65
66      def splinefit2(t, c0, c1, c2, c3, c4, c5):
67          x, x0 = t[0], t[1]
68          func = c0 + c1 * (x - x0) + c2 * (x - x0) ** 2 + \
69              c3 * (x - x0) ** 3 + c4 * (x - x0) ** 4 + \
70              c5 * (x - x0) ** 5
71          return func
72
73      #third order scipy spline
74      SPLINE = splrep(x, y, s=0, k=3)
75
76      #START WITH EXPONENTIAL FIT
77      #find last x value below 0.50 Bohr
78      s1 = x[0]
79      x_cut = x[-1]
80      for i in x:
81          if i < 0.50:
82              s2 = i
83
84      print 'Exponential function will be fitted in ' + \
85          'the range {0} to {1}'.format(s1, s2)
86
87      t = np.linspace(s1, s2, 10)
88      print t
89      data = splev(t, SPLINE)
90      expParams, fitCovariances = curve_fit(expfit, t, data)
91      print ' Exp. fit coefficients:\n', expParams
92      print ' Covariance matrix:\n', fitCovariances
93
94      repulsion_string = 'Spline\n'
95
96      if DEBUG:
97          import matplotlib.pylab as pl
98          a1, a2, a3 = expParams
```

```
99          X = np.linspace(s1, s2, 30)
100
101         Y = [splev(x, SPLINE) for x in X]
102         Y2 = [expfit(x, a1, a2, a3) for x in X]
103
104         pl.plot(X, Y)
105         pl.plot(X, Y2)
106
107     #now we fit the cubic splines piecewise,except the last
108     #hereby we split the range in pieces of length 0.10 Bohr,
109     #except the last one with 0.4 Bohr
110     deltax = 0.10
111     final_dx = 0.30
112     x_end = x_cut - final_dx
113     N_dftbplus = int((x_end - s2) / deltax)
114     x_end = s1 + deltax * N_dftbplus
115
116     repulsion_string += '{0} {1:4.2f}\n'.format(N_dftbplus + 1, x_cut)
117     a1, a2, a3 = expParams
118     repulsion_string += '{0:18.15f} {1:18.15f} {2:18.15f}\n'.format(a1, a2, a3)
119
120     start = s2
121     end = s2 + deltax
122     for knot in range(N_dftbplus):
123         print 'Fitting a spline basis function in the range between ' + \
124             '{0} and {1}'.format(start, end)
125         t = np.linspace(start, end, 6)
126         data = splev(t, SPLINE)
127         splParams, fitCovariances = curve_fit(splinefit, [t, start], data)
128         print ' Spline fit coefficients:\n', splParams
129         print ' Covariance matrix:\n', fitCovariances
130
131         c0, c1, c2, c3 = splParams
132         repulsion_string += '{0:5.3f} {1:5.3f} {2:19.15f} {3:19.15f} \
133 {4:19.15f} {5:19.15f}\n'.format(start, end, c0, c1, c2, c3)
134
135         if DEBUG:
136             X = np.linspace(start, end, 20)
137             Y = [splev(x, SPLINE) for x in X]
138             Y2 = [splinefit([x, start], c0, c1, c2, c3) for x in X]
139             pl.plot(X, Y)
140             pl.plot(X, Y2)
141
142         start = end
143         end += deltax
144
145     end = x_cut
146     print 'Now Fitting the final spline basis function in the range ' + \
147           'between {0} and {1}'.format(start, end)
148
149     t = np.linspace(start, end, 12)
150     data = splev(t, SPLINE)
151     splParams, fitCovariances = curve_fit(splinefit2, [t, start], data)
152     print ' Spline fit coefficients:\n', splParams
153     print ' Covariance matrix:\n', fitCovariances
154
155     c0, c1, c2, c3, c4, c5 = splParams
156     repulsion_string += '{0:5.3f} {1:5.3f} {2:19.15f} {3:19.15f} {4:19.15f} \
157 {5:19.15f} {6:19.15f} {7:19.15f}\n'.format(start, end, c0, c1, c2, c3, c4, c5)
158
159     if DEBUG:
160         X = np.linspace(start, end, 20)
```

```
161             Y = [splev(x, SPLINE) for x in X]
162             Y2 = [splinefit2([x, start], c0, c1, c2, c3, c4, c5) for x in X]
163             pl.plot(X, Y)
164             pl.plot(X, Y2)
165             pl.show()
166 
167         return repulsion_string
168 
169     def generate_DFTBplus_header(elmdat, pardat, hetero):
170         """
171         Transforms Hotbit Metadata and Hamiltonian to DFTB+ format.
172         This function generates output to be added to an .skf
173         file. It outputs a string that has to be inserted
174         in the right position.
175         GS Michelitsch, 14/03/2014
176         """
177         # First Line
178         # [gridDist]   [nGridPoints]   [?]
179         # Uncommented non-documented 3rd parameter, it breaks Hotbit
180         header = str("%.12f" % (pardat[0][1] - pardat[0][0])) + ', ' + \
181             str(len(pardat[1]) + int(pardat[0][0] / (pardat[0][1] - pardat[0][0])))
182         #+ ', ' + '0\n'
183 
184         header += '\n'
185 
186         if hetero:
187             # Second Line
188             # [Ed]   [Ep]   [Es]
189             # (if present, otherwise 0.0)
190             for i in range(3 - len(elmdat[0]['epsilon'].keys())):
191                 header += '0.0 '
192             for key in sorted(elmdat[0]['epsilon'].keys()):
193                 header += str("%.8f" % elmdat[0]['epsilon'][key]) + ' '
194 
195             # Second Line
196             # [SPE]   [Ud]   [Up]   [Us]
197             # (we don't have the SPE value in Hotbit: Spin Polarization Error of
198             # early implementations in DFTB. Apparently only Us is evaluated,
199             # therefore we have the same value for Ud Up Us)
200             header += ', 0.0, ' + (str("%.6f" % elmdat[0]['U']) + ' ') * 3
201 
202             # Second Line
203             # [fd]   [fp]   [fs]
204             # Occupation numbers of valence orbitals
205             for i in range(3 - len(elmdat[0]['valence_orbitals'])):
206                 header += '0.0 '
207             for key in sorted(elmdat[0]['configuration'].keys()):
208                 if key in elmdat[0]['valence_orbitals']:
209                     header += str("%.1f" % elmdat[0]['configuration'][key]) + ' '
210 
211             header += '\n'
212 
213         # Third line
214         # [mass]   [c2] - [c9]   [rcut]   [d1] - [d10]
215         # Except for [mass], all parameters are set to 1.0
216         header += str("%.2f" % elmdat[0]['mass']) + ', 19*1.0,\n'
217 
218         # Fourth Line
219         # [Hxxx]
220         # Integral table containing the DFTB Hamiltonian
221         if pardat[0][0] != 0:
222             for i in range(int(pardat[0][0] / (pardat[0][1] - pardat[0][0]))):
```

```
223                 header += str(len(pardat[1][0])) + '*1.0,\n'
224         ct, theader = 0, ''
225         for i in range(len(pardat[1])):
226             for j in range(len(pardat[1][i])):
227                 if pardat[1][i][j] == 0:
228                     ct += 1
229                     theader = str(ct) + '*0.0 '
230                 else:
231                     ct = 0
232                     header += theader
233                     theader = ''
234                     header += '{0: 1.12e}  '.format(pardat[1][i][j])
235             if theader != '':
236                 ct = 0
237                 header += theader
238                 theader = ''
239                 header += '{0: 1.12e}  '.format(pardat[1][i][j])
240             header += '\n'
241 
242         return header
243 
244 elmf = None
245 
246 # Open Files
247 try:
248     parf = open(argv[1] + '_' + argv[2] + '.par')
249     elmf = open(argv[1] + '.elm')
250 except:
251     parf = open(argv[2] + '_' + argv[1] + '.par')
252 
253 
254 # Read line-by-line (needed for repulsive term)
255 tmp = parf.readlines()
256 
257 
258 for carousel in [(argv[1], argv[2]), (argv[2], argv[1])]:
259 
260     # Open Outfile
261     skff = open(carousel[0] + '-' + carousel[1] + '.skf', 'w')
262 
263     # Read relevant data (A-B and B-A is different!)
264     elmdat = native.read_element_from_elm(elmf, argv[1])
265     pardat = native.read_HS_from_par(parf, carousel[0], carousel[1])
266 
267     # Generate DFTBplus format string
268     print 'Reading in Hotbit Metadata and repulsive potential'
269     header = generate_DFTBplus_header(elmdat,
270                                       pardat,
271                                       argv[1] == argv[2]) + \
272         generate_DFTBplus_repulsion(tmp,
273                                     DEBUG=False)
274 
275     skff.write(header)
276     skff.close()
277 
278 # Close files
279 parf.close()
280 elmf.close()
```

Listing A.3: hb2skf.py - A script to convert Hotbit .elm and .par files into DFTB+ compatible .skf Slater-Koster tables

Appendix B

Supplementary data

B.1 Internal parameters of DFTB-screening

Table B.1: *Set of internal coordinates in the screening appoach used to generate the Kernel Density Estimations (KDE) diagrams. This Table holds all conformations after exclusion of those not satisfying the physical boundary conditions and chemical requirements. Identifiers "-hnn" designates the removal of a hydrogen atom.*

	Ψ_1 [°]	Ψ_2 [°]	Φ_1 [°]	Φ_2 [°]	α [°]	θ [°]	$d_1^{O\|Au}$ [Å]	$d_2^{O\|Au}$ [Å]
hr1	232.4	54.8	163.8	218.6	24.1	20.1	2.9	3.3
hr1-h24	1.0	190.6	158.4	179.5	17.3	15.4	2.9	3.0
hr1-h27	233.7	55.5	162.7	219.8	24.4	20.5	2.9	3.2
hr1-h29	202.3	23.1	165.2	202.7	20.7	20.3	2.9	3.1
hr1-h38	348.4	167.3	141.0	173.1	37.7	14.3	2.9	3.0
hr1-h39	261.7	78.6	173.8	210.4	14.3	27.2	3.0	3.3
hr1-h42	209.9	35.7	175.5	218.9	12.2	21.0	3.0	3.2
hr1-h48	358.6	177.6	164.0	107.9	49.2	22.5	2.9	3.0
hr1-h49	308.6	137.6	147.7	195.5	30.5	20.3	2.9	3.1
hr2-h24	1.9	185.3	187.5	188.0	-1.4	10.2	2.8	2.4
hr3	182.7	354.1	179.2	170.6	4.6	18.0	2.9	3.2
hr3-h27	182.2	352.5	178.5	172.6	4.1	18.1	2.9	3.0
hr3-h29	172.7	343.7	174.5	176.1	8.4	24.8	2.9	3.1
hr3-h38	182.5	351.7	178.2	169.6	4.6	20.4	2.8	3.1
hr3-h39	185.0	355.3	179.3	167.9	5.0	18.5	2.9	3.1
hr3-h48	133.8	311.4	226.8	220.0	-15.1	19.2	2.9	2.3
hr4	174.5	344.7	176.7	176.2	5.3	15.1	2.9	3.2
hr4-h27	174.7	343.5	176.9	176.9	4.5	14.9	2.9	3.2
hr4-h29	176.2	346.6	176.4	176.0	4.8	15.7	2.9	3.2
hr4-h38	178.7	347.8	174.5	173.4	5.7	20.0	2.9	3.0
hr4-h39	175.7	343.4	175.9	177.9	4.5	16.2	2.9	3.1
hr5	174.1	344.1	176.8	176.9	5.5	16.5	2.9	3.2
hr5-h27	173.8	342.1	176.5	177.7	4.7	17.0	2.9	3.2
hr5-h29	180.2	349.9	178.0	169.7	6.2	19.7	3.0	3.2
hr5-h38	179.0	350.4	173.8	175.1	6.5	22.7	2.9	2.4
hr5-h39	184.2	352.6	178.2	168.8	5.0	18.9	2.9	3.1
hr5-h42	186.2	359.6	173.8	172.2	5.2	17.0	3.0	2.8
hr5-h49	262.8	80.0	194.7	74.4	20.4	43.1	3.0	3.1
hr6	202.5	26.6	177.4	352.7	4.9	20.6	2.9	3.1
hr6-h24	172.0	357.9	201.3	352.0	13.1	11.9	3.0	3.2

	Ψ_1 [°]	Ψ_2 [°]	Φ_1 [°]	Φ_2 [°]	α [°]	θ [°]	$d_1^{O\|Au}$ [Å]	$d_2^{O\|Au}$ [Å]
hr6-h27	177.0	6.3	182.5	0.8	2.0	22.1	2.9	3.1
hr6-h29	191.9	18.6	181.2	357.3	5.4	19.2	2.9	2.9
hr6-h38	170.3	358.1	205.2	353.3	15.0	16.3	2.9	2.9
hr6-h39	175.9	0.0	189.9	356.6	8.1	21.4	2.9	3.0
hr6-h42	202.7	27.5	178.2	352.6	5.1	20.0	2.9	3.0
hr6-h48	137.3	317.1	188.8	61.3	15.4	11.1	2.9	2.8
hr6-h49	235.3	60.9	178.3	324.7	0.7	16.2	2.9	2.9
hr7	190.4	16.9	1.4	183.6	10.7	23.3	2.9	3.0
hr7-h27	191.3	16.2	359.6	187.5	12.4	23.0	2.9	3.0
hr7-h29	192.2	19.5	359.4	183.8	9.8	23.3	2.9	3.0
hr7-h38	180.5	6.9	11.1	180.1	14.9	28.3	2.9	2.6
hr7-h39	197.1	23.2	358.5	180.3	10.2	27.3	2.7	2.8
hr7-h42	201.5	30.3	0.6	192.2	7.0	11.7	2.9	2.4
hr7-h48	157.8	329.2	143.4	92.1	21.3	41.9	2.9	2.8
hr7-h49	129.8	310.4	107.3	170.3	4.5	24.2	2.9	2.8
hr8	184.2	355.0	178.8	168.6	5.1	17.7	2.9	3.2
hr8-h24	186.8	356.1	159.7	179.3	18.1	18.3	2.9	3.1
hr8-h27	181.8	352.0	178.6	171.6	4.1	16.7	2.9	3.1
hr8-h29	174.4	345.8	174.7	174.5	8.5	22.4	2.9	3.1
hr8-h39	174.8	354.2	178.8	165.5	10.5	21.9	2.9	3.1
hr8-h42	189.6	4.2	174.2	168.8	5.7	7.9	2.3	3.1
hr8-h49	157.8	325.2	164.0	190.4	7.4	20.6	2.9	3.0
hr9	331.9	155.5	159.5	178.7	29.7	15.6	3.0	3.2
hr9-h24	357.3	190.3	160.0	176.6	16.1	13.3	2.9	3.1
hr9-h29	359.7	196.6	163.3	181.2	12.5	26.5	3.0	2.9
hr9-h38	350.5	171.0	139.0	173.1	38.1	10.5	2.9	3.1
hr9-h39	22.2	207.6	165.1	173.9	11.2	20.7	2.9	2.4
hr9-h42	325.6	146.3	156.9	172.5	30.7	18.4	2.9	3.3
hr9-h48	11.3	189.0	144.5	128.9	49.1	20.9	2.9	3.0
hr10	183.3	354.7	175.3	171.0	6.3	13.1	3.0	3.2
hr10-h24	182.0	356.5	104.2	175.2	55.4	10.2	2.9	3.1
hr10-h27	181.4	351.8	179.4	172.7	2.4	11.5	2.9	2.8
hr10-h29	130.0	300.2	156.9	191.0	31.9	18.4	2.9	3.2
hr10-h38	183.1	0.5	78.5	174.5	54.6	6.8	2.9	3.2
hr10-h39	182.1	353.2	177.9	172.1	5.9	19.4	2.9	3.0
hr10-h42	186.3	359.4	173.4	172.6	5.5	18.3	3.0	2.8
hr10-h48	189.2	6.0	127.5	146.8	51.5	22.8	2.9	3.1
hr10-h49	136.8	305.7	139.0	201.9	39.5	17.3	2.9	3.1
hr11	182.1	357.3	176.7	180.7	8.9	11.3	2.9	2.4
hr11-h24	182.9	358.8	88.4	177.3	58.0	10.3	2.9	2.3
hr11-h38	178.2	356.9	96.4	177.9	58.3	11.3	2.9	2.3
hr11-h39	149.6	319.8	162.8	176.1	39.8	15.6	2.9	2.4
hr11-h49	236.2	63.3	11.4	214.0	43.7	15.9	2.9	3.0
hr12	324.8	144.7	6.7	185.2	20.6	23.8	3.0	3.0
hr12-h24	343.3	158.6	355.4	193.2	23.4	19.1	3.0	2.9
hr12-h27	326.5	144.6	8.0	185.1	21.0	23.8	2.9	3.0
hr12-h29	327.9	153.3	355.2	187.2	14.0	25.0	2.9	3.0
hr12-h38	346.7	163.9	356.1	189.0	23.5	18.8	3.0	2.9
hr12-h39	356.8	151.8	359.5	172.2	1.2	22.2	2.9	2.9
hr12-h42	344.0	158.1	2.3	178.9	9.5	12.3	2.9	2.9
hr12-h48	313.7	137.7	125.7	116.5	38.1	29.0	2.9	2.9
hr12-h49	290.9	112.8	17.0	136.7	22.6	18.3	3.0	3.0
hr13	170.2	348.6	181.1	173.6	7.9	15.8	2.9	3.2
hr14	7.1	201.6	162.0	178.1	13.2	26.6	2.9	3.0
hr15	171.3	344.8	174.5	177.2	9.4	25.1	2.9	3.0
hr16	185.2	356.5	176.9	169.7	5.8	29.5	2.9	3.0

	Ψ_1 [°]	Ψ_2 [°]	Φ_1 [°]	Φ_2 [°]	α [°]	θ [°]	$d_1^{O\|Au}$ [Å]	$d_2^{O\|Au}$ [Å]
hr17	331.6	155.0	159.0	178.3	29.9	19.6	3.0	3.2
hr18	189.8	16.1	358.3	183.3	10.1	16.0	2.9	3.0
hr19	311.6	136.4	340.3	183.1	-27.7	23.0	3.0	3.0
hr20	59.0	238.1	17.2	191.4	42.3	8.2	2.9	3.1
hr21	187.8	15.1	1.1	182.3	10.3	24.7	2.9	3.0
hr22	326.0	151.5	348.4	171.8	14.5	26.8	2.9	3.0
hr23	42.1	219.3	15.7	192.0	37.9	9.8	2.9	2.9
hr24	7.7	180.7	359.6	193.0	15.8	24.8	2.9	3.0
hr25	340.8	159.5	356.0	183.5	9.2	26.2	2.9	3.0

Table B.2: Set of internal coordinates of the isomers optimized as dimers with DFTB (Hotbit). The index designates the first and second molecule in the dimeric arrangement.

	Ψ_1 [°]	Ψ_2 [°]	Φ_1 [°]	Φ_2 [°]	α [°]	θ [°]	$d_1^{O\|Au}$ [Å]	$d_2^{O\|Au}$ [Å]
$hr10_1$	185.6	359.3	174.5	173.9	7.7	176.3	2.7	2.9
$hr10_2$	184.5	355.2	173.6	173.0	7.6	6.8	2.7	3.0
$hr17_1$	0.1	192.5	158.6	184.2	15.9	173.8	2.8	2.8
$hr17_2$	5.8	200.6	162.8	176.8	10.9	2.6	2.6	3.0
$hr19_1$	312.3	138.2	341.7	177.9	-26.3	152.3	2.8	2.7
$hr19_2$	310.8	137.6	343.0	180.2	-26.3	30.7	2.9	2.6
$hr20_1$	43.6	221.6	11.8	196.6	38.7	172.4	2.8	3.0
$hr20_2$	44.5	224.2	14.0	201.0	41.8	7.3	2.8	3.0
$hr23_1$	43.2	219.1	15.8	195.4	38.0	3.3	2.8	2.9
$hr23_2$	45.4	224.3	13.6	198.4	36.5	174.4	2.8	2.9
$hr25_1$	288.5	105.0	13.5	168.3	38.5	176.6	2.8	2.9
$hr25_2$	281.7	101.2	12.2	176.5	41.4	3.8	2.8	3.0

B.2 Tersoff-Hamann images and spin density

Shown here are Tersoff-Hamann STM topographs calculated from DFTB-LDOS obtained from Hotbit and differential spin densities (ρ^{α} - ρ^{β}) obtained from DFT calculations with TURBOMOLE of the screening candidates listed in Table 5.1. The LDOS was calculated at a bias voltage of -2.5 V using a grid-spacing of 0.2 Å and the atomic pro-molecular wavefunctions were cut off at 3 Å. A rolling-ball-smearing was applied with a ball-size of 2 Å at an average density of 10^{-5} electrons. A Gaussian smoothing post-processing filter with 4.0 Å in x- and y-dimensions was applied. All topographs were normalized to one scale. Isovalue of spin density distribution = 0.002.

Figure B.1: *Simulated STM topographs and differential spin density (ρ^{α} - ρ^{β}) of screening group 1*

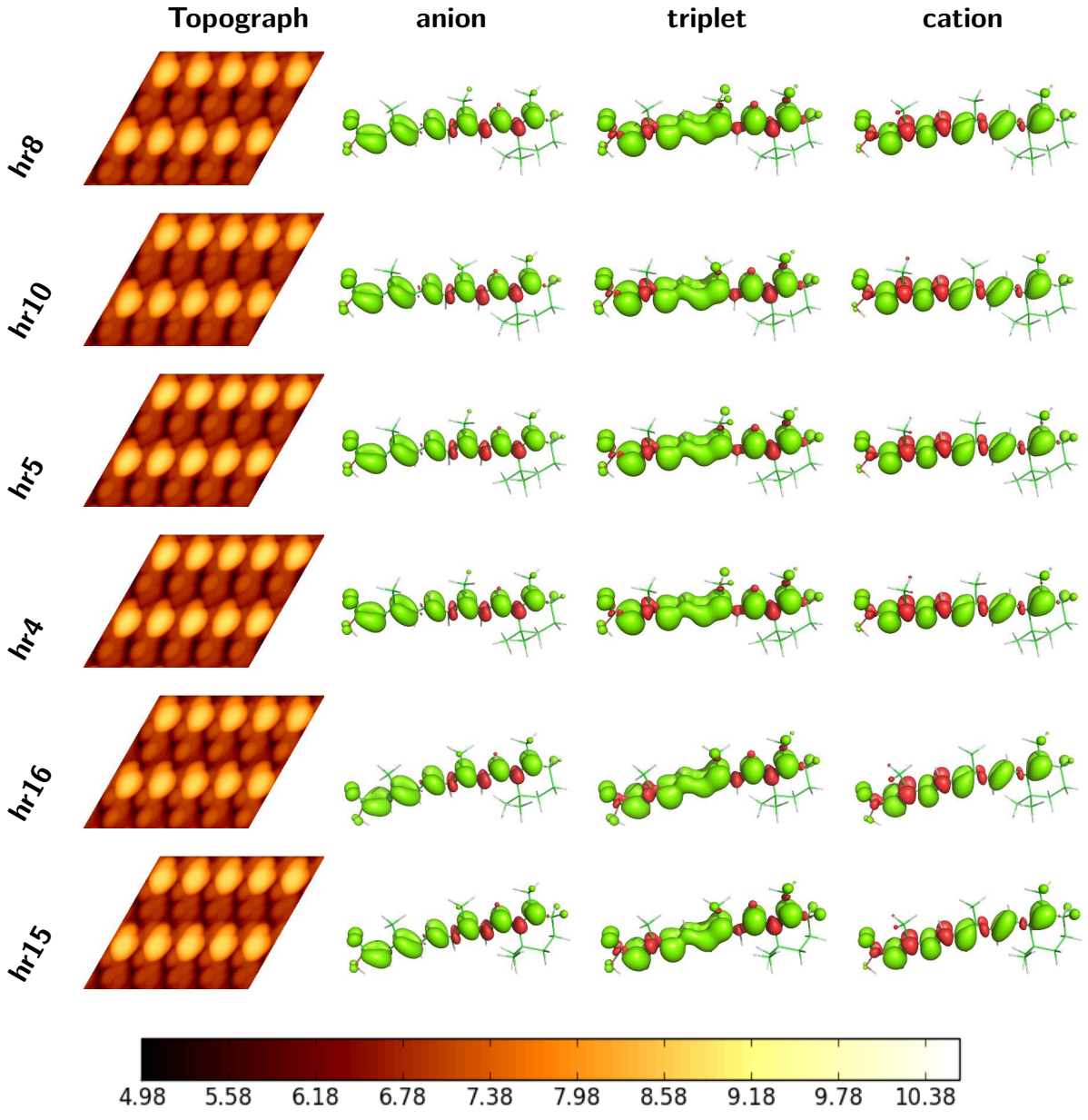

Figure B.2: *Simulated STM topographs and differential spin density (ρ^{α} - ρ^{β}) of screening group 2*

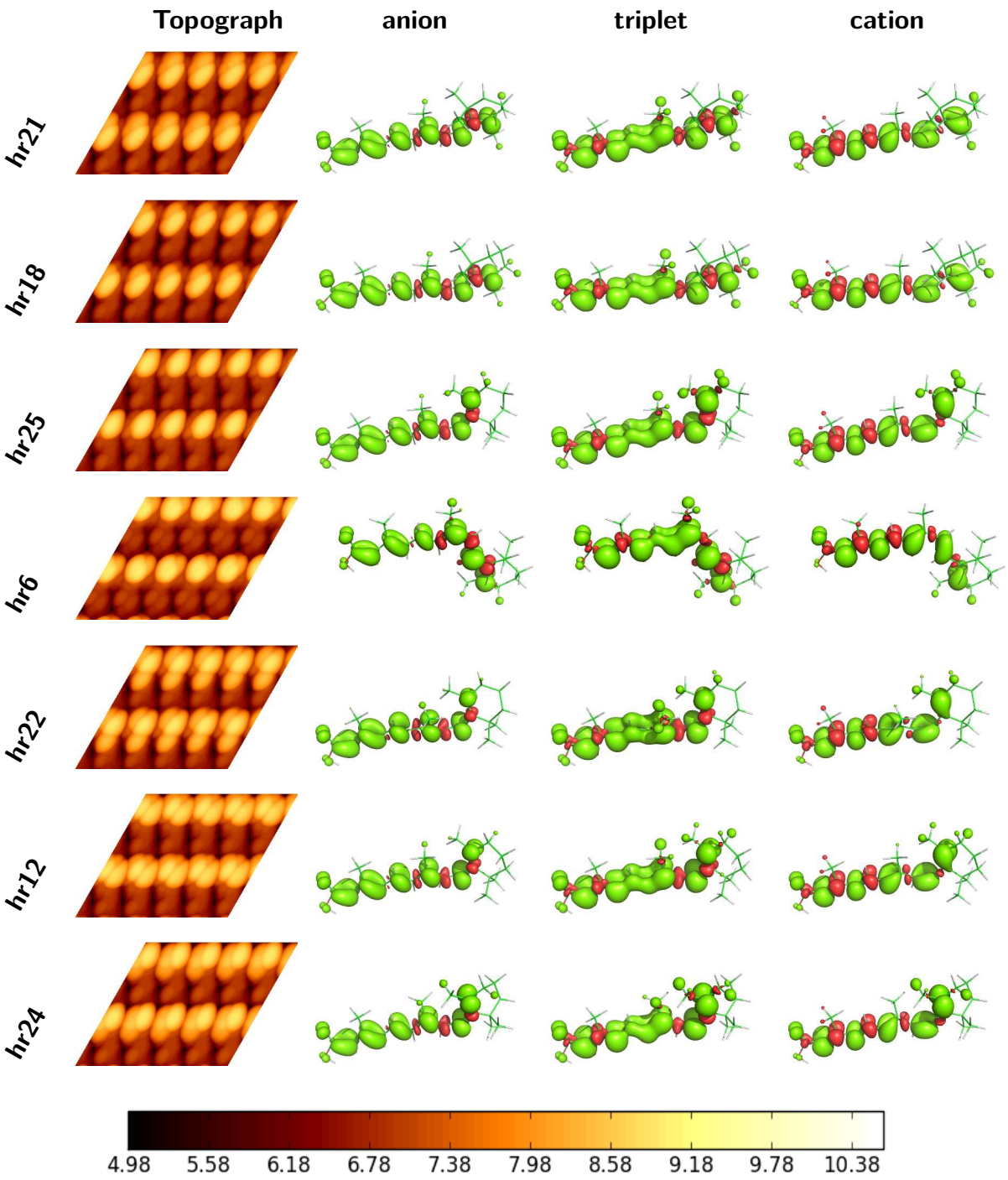

Figure B.3: *Simulated STM topographs and differential spin density (ρ^{α} - ρ^{β}) of screening group 3*

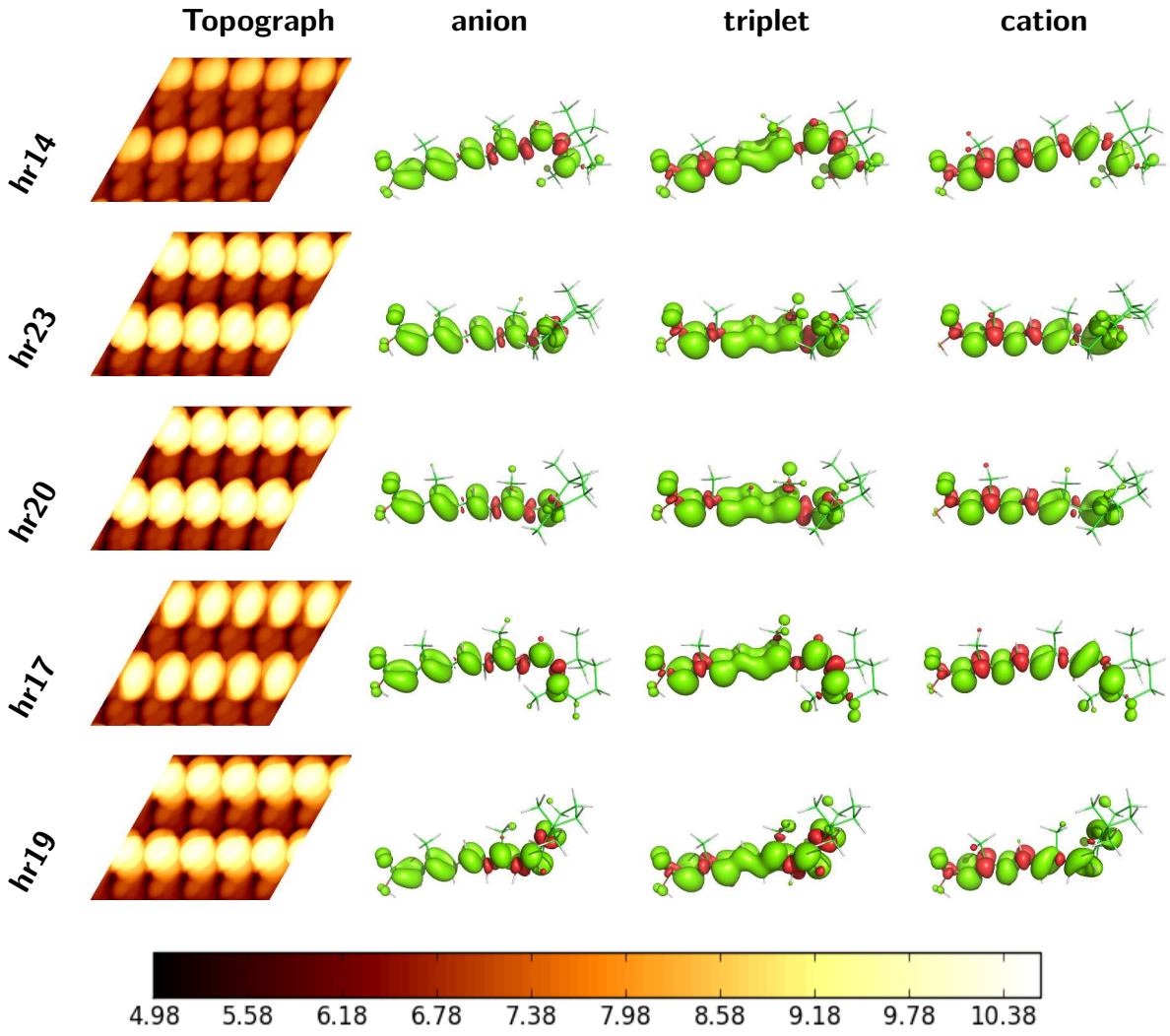

Figure B.4: *Total density difference of screening group 1*

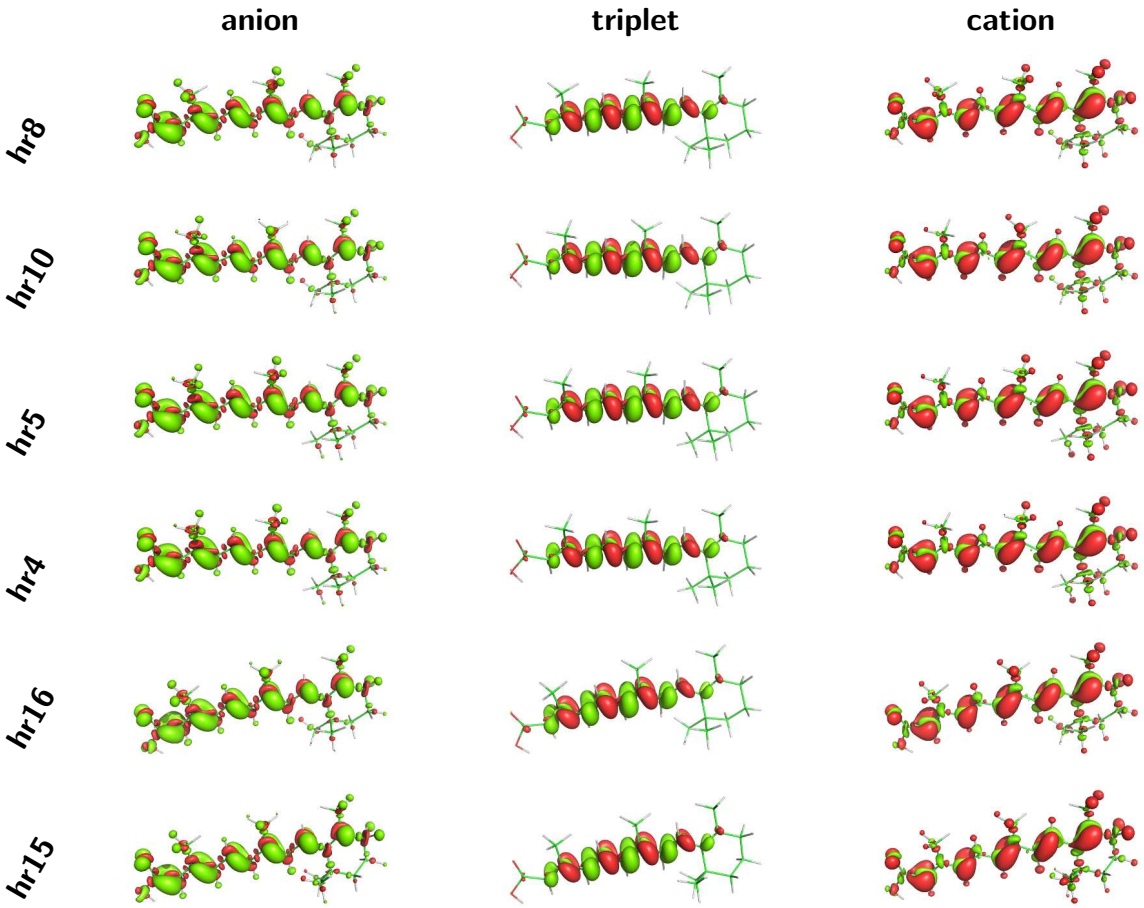

Figure B.5: *Total density difference of screening group 2*

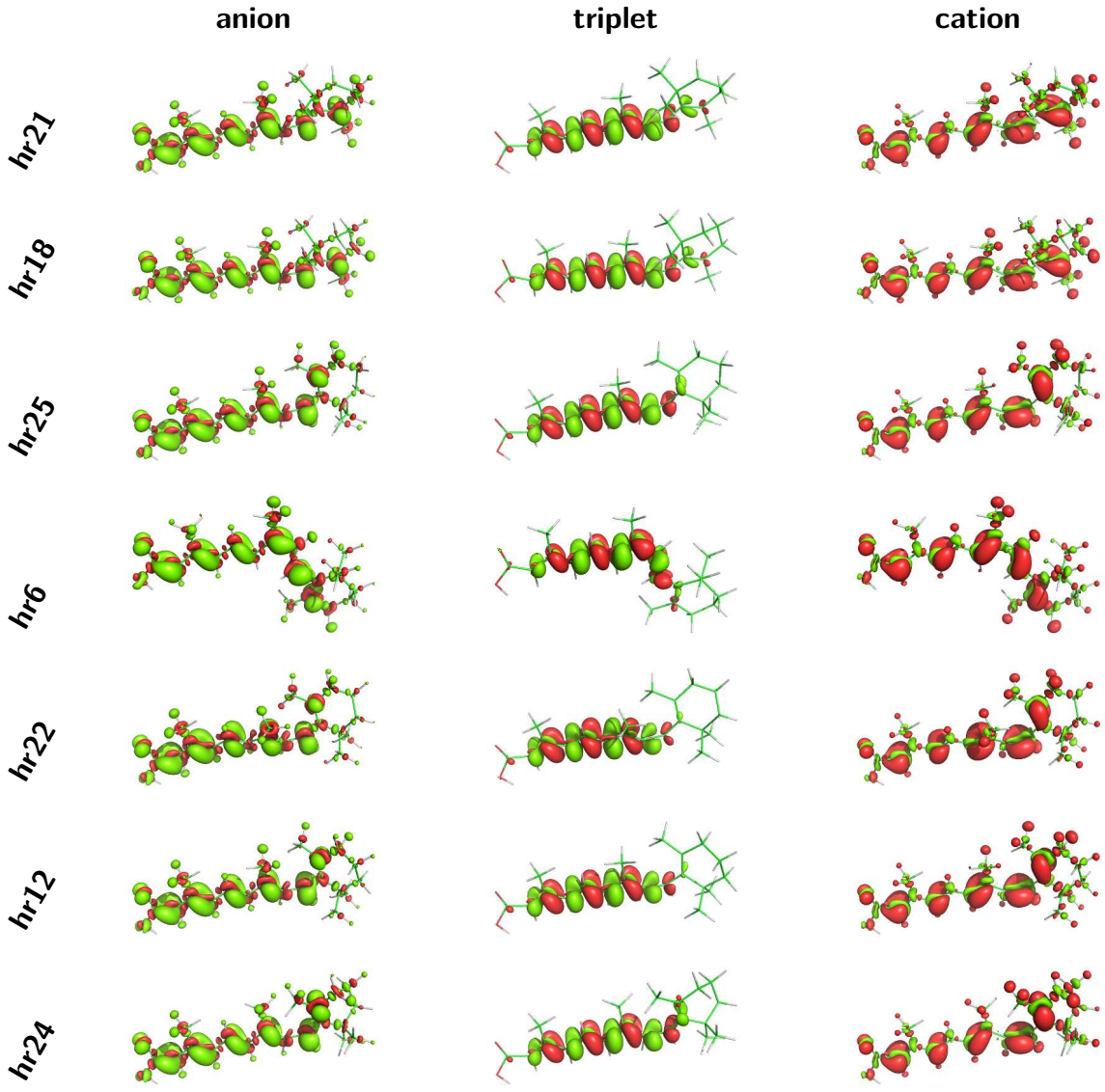

Figure B.6: *Total density difference of screening group 3*

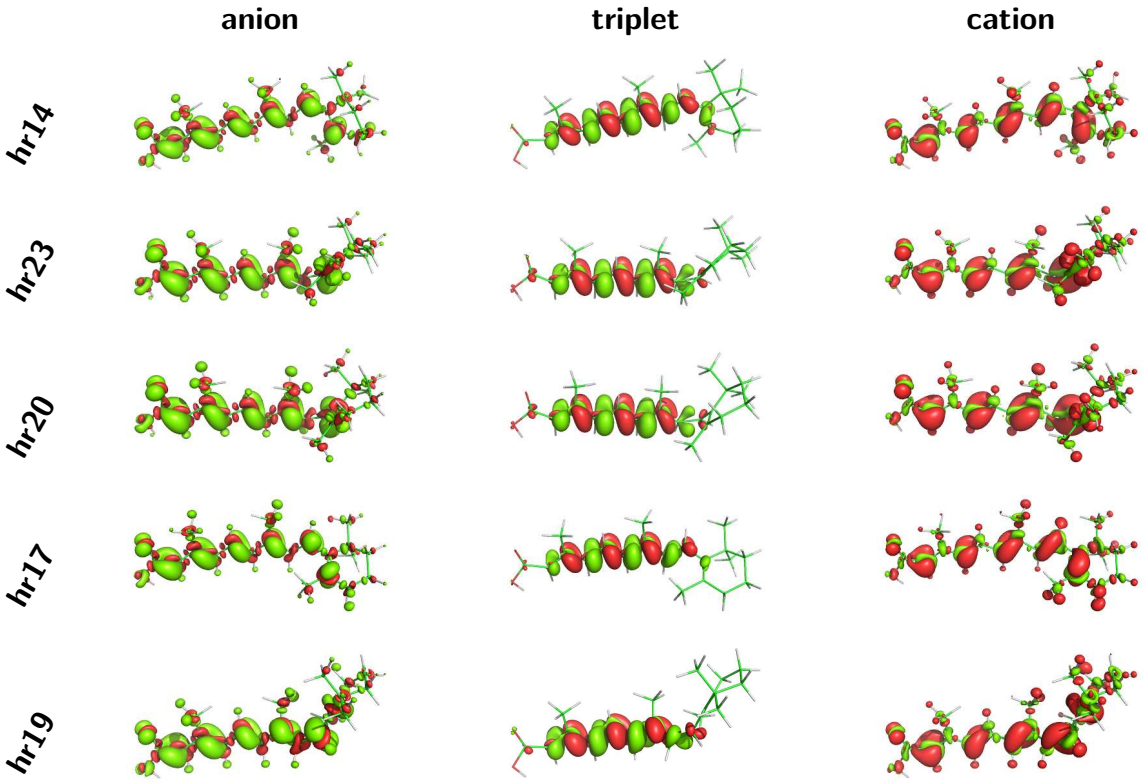

List of Figures

List of Tables

Bibliography

[1] Boole, G. *The Mathematical Analysis of Logic: Being an Essay Towards a Calculus of Deductive Reasoning, by George Boole*; Henderson and Spalding: London, Cambridge, 1847.

[2] Eckert, J. P.; Mauchly, J. W. Electronic numerical integrator and computer. 1964; US Patent 3,120,606.

[3] Zuse, K. *Der Computer - Mein Lebenswerk*; Springer Berlin Heidelberg, 2007.

[4] Bashe, C. J.; Johnson, L. R.; Palmer, J. H.; Pugh, E. W. *IBM's early computers*; The MIT Press: Cambridge, 1985.

[5] Moore, G. *Electronics* **1965**, *38*, 114–117.

[6] Lim, H. S.; Han, J. T.; Kwak, D.; Jin, M.; Cho, K. *J. Am. Chem. Soc.* **2006**, *128*, 14458–9.

[7] Feng, X.; Liu, J.; Rieke, P. C.; Fryxell, G. E. *Macromolecules* **1998**, *31*, 7845–7850.

[8] Liu, X.; Ye, Q.; Yu, B.; Liang, Y.; Liu, W.; Zhou, F. *Langmuir* **2010**, *26*, 12377–82.

[9] Xu, L.; Chen, W.; Mulchandani, A.; Yan, Y. *Angew. Chem. Int. Ed.* **2005**, *44*, 6009–12.

[10] Morin, J.-F.; Shirai, Y.; Tour, J. M. *Org. Lett.* **2006**, *8*, 1713–6.

[11] Tierney, H. L.; Murphy, C. J.; Jewell, A. D.; Baber, A. E.; Iski, E. V.; Khodaverdian, H. Y.; McGuire, A. F.; Klebanov, N.; Sykes, E. C. H. *Nat. Nanotechnol.* **2011**, *6*, 625–9.

[12] Feringa, B. L. In *Molecular Switches*; Feringa, B. L., Ed.; Wiley-VCH Verlag GmbH: Weinheim, FRG, 2001.

[13] Morgenstern, K. *Prog. Surf. Sci.* **2011**, *86*, 115–161.

[14] Gärtner, W. *Angew. Chem.* **2001**, *113*, 3065–3069.

[15] Huntress, M. M.; Gozem, S.; Malley, K. R.; Jailaubekov, A. E.; Vasileiou, C.; Vengris, M.; Geiger, J. H.; Borhan, B.; Schapiro, I.; Larsen, D. S.; Olivucci, M. *J. Phys. Chem. B.* **2013**, *117*, 10053–70.

[16] Gozem, S.; Schapiro, I.; Ferré, N.; Olivucci, M. *Science* **2012**, *337*, 1225–8.

[17] Frutos, L. M.; Andruniów, T.; Santoro, F.; Ferré, N.; Olivucci, M. *Proc. Natl. Acad. Sci. U. S. A.* **2007**, *104*, 7764–9.

[18] Ferré, N.; Cembran, A.; Garavelli, M.; Olivucci, M. *Theor. Chem. Acc.* **2004**, *112*, 335–341.

[19] Karan, S.; Wang, Y.; Robles, R.; Lorente, N.; Berndt, R. *J. Am. Chem. Soc.* **2013**, *135*, 14004–7.

[20] Binnig, G.; Rohrer, H.; Gerber, C.; Weibel, E. *Phys. Rev. Lett.* **1982**, *49*, 57–61.

[21] Eigler, D. M.; Schweizer, E. K. *Nature* **1990**, *344*, 524–526.

[22] Grill, L.; Dyer, M.; Lafferentz, L.; Persson, M.; Peters, M. V.; Hecht, S. *Nat. Nanotechnol.* **2007**, *2*, 687–91.

[23] Comstock, M.; Cho, J.; Kirakosian, A.; Crommie, M. *Phys. Rev. B* **2005**, *72*, 153414.

[24] Berndt, R.; Wang, Y.; Karan, S. *private communication*; 2013/2014; Institut für Experimentelle und Angewandte Physik, Christian-Albrechts Universität Kiel.

[25] Morrison, G. H. *Pure Appl. Chem.* **1974**, *41*, 405–431.

[26] Madhavan, V. *Science* **1998**, *280*, 567–569.

[27] Kondo, J. *Prog. Theor. Phys.* **1964**, *32*, 37–49.

[28] de Haas, W.; de Boer, J.; van dën Berg, G. *Physica* **1934**, *1*, 1115–1124.

[29] Requist, R.; Modesti, S.; Baruselli, P. P.; Smogunov, A.; Fabrizio, M.; Tosatti, E. *Proc. Natl. Acad. Sci. U. S. A.* **2014**, *111*, 69–74.

[30] Scott, G. D.; Natelson, D. *ACS Nano* **2010**, *4*, 3560–79.

[31] Fernández-Torrente, I.; Franke, K.; Pascual, J. *Phys. Rev. Lett.* **2008**, *101*, 217203.

[32] Levine, I. N. *Quantum chemistry*, 5th ed.; Prentice-Hall, Inc: New York, 2000; p 739.

[33] Szabo, A.; Ostlund, N. S. *Modern Quantum Chemistry: Introduction to Advanced Electronic Structure Theory*; Dover Publications, Inc.: Mineola, New York, 1996.

[34] McQuarrie, D. A. *Quantum Chemistry*, 2nd ed.; University Science Books: Sausalito, California, 2008.

[35] Koch, W.; Holthausen, M. C. *A Chemists Guide to Density Functional Theory*; Wiley-VCH Verlag GmbH: Weinheim, Germany, 2000.

[36] Schrödinger, E. *Ann. Phys.* **1926**, *384*, 361–376.

[37] Born, M.; Oppenheimer, R. *Annalen der Physik* **1927**, *389*, 457–484.

[38] Christiansen, O.; Koch, H.; Jørgensen, P. *Chem. Phys. Lett.* **1995**, *243*, 409–418.

[39] Hohenberg, P.; Kohn, W.; Others, *Phys. Rev.* **1964**, *136*, B864–B871.

[40] Kohn, W.; Sham, L. J. *Phys. Rev.* **1965**, *140*, A1133–A1138.

[41] Sousa, S. F.; Fernandes, P. A.; Ramos, M. J. *J. Phys. Chem. A* **2007**, *111*, 10439–52.

[42] Perdew, J. P.; Burke, K.; Ernzerhof, M. *Phys. Rev. Lett.* **1996**, *77*, 3865–3868.

[43] Perdew, J. P.; Ernzerhof, M.; Burke, K. *J. Chem. Phys.* **1996**, *105*, 9982.

[44] Adamo, C.; Barone, V. *J. Chem. Phys.* **1999**, *110*, 6158.

[45] Stephens, P. J.; Devlin, F. J.; Chabalowski, C. F.; Frisch, M. J. *J. Phys. Chem.* **1994**, *98*, 11623–11627.

[46] Dion, M.; Rydberg, H.; Schröder, E.; Langreth, D. C.; Lundqvist, B. I. *Phys. Rev. Lett.* **2004**, *92*, 246401.

[47] Klimeš, J.; Michaelides, A. *J. Chem. Phys.* **2012**, *137*, 120901.

[48] Grimme, S.; Antony, J.; Ehrlich, S.; Krieg, H. *J. Chem. Phys.* **2010**, *132*, 154104.

[49] Tkatchenko, A.; Scheffler, M. *Phys. Rev. Lett.* **2009**, *102*, 073005.

[50] Ruiz, V. G.; Liu, W.; Zojer, E.; Scheffler, M.; Tkatchenko, A. *Phys. Rev. Lett.* **2012**, *108*, 146103.

[51] Zaremba, E.; Kohn, W. *Phys. Rev. B* **1976**, *13*, 2270.

[52] Hirshfeld, F. L. *Theor. Chim. Acta* **1977**, *44*, 129–138.

[53] Oliveira, A. F.; Seifert, G.; Heine, T.; Duarte, H. A. *J. Braz. Chem. Soc.* **2009**, *20*, 1193–1205.

[54] Koskinen, P.; Mäkinen, V. *Comp. Mater. Sci.* **2009**, *47*, 237–253.

[55] Slater, J. C.; Koster, G. F. *Phys. Rev.* **1954**, *94*, 1498–1524.

[56] Foulkes, W.; Haydock, R. *Phys. Rev. B* **1989**, *39*, 12520.

[57] Frauenheim, T.; Seifert, G.; Elstner, M.; Niehaus, T.; Köhler, C.; Amkreutz, M.; Sternberg, M.; Hajnal, Z.; Carlo, A. D.; Suhai, S. *J. Phys.: Condens. Matter* **2002**, *14*, 3015–3047.

[58] Elstner, M.; Porezag, D.; Jungnickel, G.; Elsner, J.; Haugk, M.; Frauenheim, T.; Suhai, S.; Seifert, G. *Phys. Rev. B* **1998**, *58*, 7260–7268.

[59] Seifert, G. *J Phys Chem A* **2007**, *111*, 5609–13.

[60] Mulliken, R. S. *J. Chem. Phys.* **1955**, *23*, 1833.

[61] Tersoff, J.; Hamann, D. R. *Phys. Rev. B* **1985**, *31*, 805–813.

[62] Bardeen, J. *Phys. Rev. Lett.* **1961**, *6*, 57–59.

[63] Liu, W.; Tkatchenko, A.; Scheffler, M. *Acc. Chem. Res.* **2014**, doi: 10.1021/ar500118y.

[64] Cox, B. D.; Muccio, D. D.; Hamilton, T. P. *Comput. Theor. Chem.* **2013**, *1011*, 11–20.

[65] Ferré, N.; Olivucci, M. *J. Am. Chem. Soc.* **2003**, *125*, 6868–9.

[66] Mercurio, G.; McNellis, E. R.; Martin, I.; Hagen, S.; Leyssner, F.; Soubatch, S.; Meyer, J.; Wolf, M.; Tegeder, P.; Tautz, F. S.; Reuter, K. *Phys. Rev. Lett.* **2010**, *104*, 036102.

[67] Liu, W.; Carrasco, J.; Santra, B.; Michaelides, A.; Scheffler, M.; Tkatchenko, A. *Phys. Rev. B* **2012**, *86*, 245405.

[68] Maurer, R. J. First-Principles Description of the Isomerization Dynamics of Surface-Adsorbed Molecular Switches. Dissertation, Technische Universität München, 2014.

[69] Bahn, S.; Jacobsen, K. *Comput. Sci. Eng.* **2002**, *4*, 56–66.

[70] Clark, S. J.; Segall, M. D.; Pickard, C. J.; Hasnip, P. J.; Probert, M. I. J.; Refson, K.; Payne, M. C. *Z Kristallogr* **2005**, *220*, 567–570.

[71] McNellis, E. R.; Meyer, J.; Reuter, K. *Phys. Rev. B* **2009**, *80*, 205414.

[72] Peterson, P. *Int. J. Comput. Sci. Eng.* **2009**, *4*, 296–305.

[73] Blum, V.; Gehrke, R.; Hanke, F.; Havu, P.; Havu, V.; Ren, X.; Reuter, K.; Scheffler, M. *Comput. Phys. Commun.* **2009**, *180*, 2175–2196.

[74] Carrasco, J.; Liu, W.; Michaelides, A.; Tkatchenko, A. *J. Chem. Phys.* **2014**, *140*, 084704.

[75] Menzel, D.; Gomer, R. *J. Chem. Phys.* **1964**, *41*, 3311.

[76] Redhead, P. A. *Can. J. Phys.* **1964**, *42*, 886–905.

[77] Groß, A. *Theoretical Surface Science*; Springer Berlin Heidelberg, 2009.

[78] Antoniewicz, P. *Phys. Rev. B* **1980**, *21*, 3811–3815.

[79] Wolf, M.; Tegeder, P. *Surf. Sci.* **2009**, *603*, 1506–1517.

[80] TURBOMOLE V6.4 2012, a development of University of Karlsruhe and Forschungszentrum Karlsruhe GmbH, 1989-2007, TURBOMOLE GmbH, since 2007; available from `http://www.turbomole.com`.

[81] Schäfer, A.; Huber, C.; Ahlrichs, R. *J. Chem. Phys.* **1994**, *100*, 5829.

[82] Weigend, F.; Ahlrichs, R. *Phys. Chem. Chem. Phys.* **2005**, *7*, 3297–305.

[83] Treutler, O.; Ahlrichs, R. *J. Chem. Phys.* **1995**, *102*, 346.

[84] Weigend, F. *Chem. Phys. Lett.* **1998**, *294*, 143–152.

[85] Gu, Z.; Li, Z.; Zhao, N.; Wang, Y. *Z. Krist.-New. Cryst. St.* **2007**, *222*, 383–384.

[86] Stowasser, R.; Hoffmann, R. *J. Am. Chem. Soc.* **1999**, *121*, 3414–3420.

[87] Soe, W.-H.; Manzano, C.; Sarkar, A. D. *Phys. Rev. Lett.* **2009**, *102*, 176102.

[88] Aviram, A.; Ratner, M. A. *Chem. Phys. Lett.* **1974**, *29*, 277–283.

[89] Ratner, M. *Nat. Nanotechnol.* **2013**, *8*, 378–81.

[90] Aviram, A.; Joachim, C.; Pomerantz, M. *Chem. Phys. Lett.* **1988**, *146*, 490–495.

[91] Dri, C.; Peters, M. V.; Schwarz, J.; Hecht, S.; Grill, L. *Nat. Nanotechnol.* **2008**, *3*, 649–53.

[92] Piantek, M.; Schulze, G.; Koch, M.; Franke, K. J.; Leyssner, F.; Krüger, A.; Navío, C.; Miguel, J.; Bernien, M.; Wolf, M.; Kuch, W.; Tegeder, P.; Pascual, J. I. *J. Am. Chem. Soc.* **2009**, *131*, 12729–35.

[93] Lotze, C.; Luo, Y.; Corso, M.; Franke, K. J.; Haag, R.; Pascual, J. I. *J. Phys. Condens. Matter* **2012**, *24*, 394016.

[94] Bronner, C.; Schulze, G.; Franke, K. J.; Pascual, J. I.; Tegeder, P. *J. Phys. Condens. Matter* **2011**, *23*, 484005.

[95] Maurer, R. J.; Reuter, K. *Angew. Chem. Int. Ed.* **2012**, *51*, 12009–11.

[96] Lambert, C. G.; Darden, T. A.; Board Jr., J. A. *J. Comput. Phys.* **1996**, *126*, 274–285.

[97] Pulay, P. *Chem. Phys. Lett.* **1980**, *73*, 393–398.

[98] Aradi, B.; Hourahine, B.; Frauenheim, T. *J. Phys. Chem. A* **2007**, *111*, 5678–84.

[99] Parzen, E. *Ann. Math. Statist.* **1962**, *33*, 1065–1076.

[100] Scott, D. W. Multivariate Density Estimation and Visualization. 2004; CASE - Center for Applied Statistics and Economics, Berlin.

[101] Jones, E.; Oliphant, T.; Peterson, P.; Al, E. SciPy: Open source scientific tools for Python. http://www.scipy.org/.

[102] Ortmann, F.; Bechstedt, F.; Schmidt, W. *Phys. Rev. B* **2006**, *73*, 205101.

[103] Grimme, S. *J. Comput. Chem.* **2006**, *27*, 1787–99.

[104] Jurecka, P.; Cerný, J.; Hobza, P.; Salahub, D. R. *J. Comput. Chem.* **2007**, *28*, 555–69.

[105] Stoehr, M. SCC-DFTB+D Applicability to Hybrid Inorganic-Organic Systems. 2014; Technische Universität München.

[106] Mäkinen, V.; Koskinen, P.; Häkkinen, H. *Eur. Phys. J. D* **2013**, *67*, 38.

[107] Dftb.org, Format of the v1.0 Slater-Koster files. http://www.dftb.org/fileadmin/DFTB/public/misc/slakoformat.pdf.

Acknowledgements

First, I would like to thank Reinhard J. Maurer and Katharina Diller for their endless support and patience in supervising me during this thesis, especially during the last few months until its completion. You not only guided me scientifically but we also had a great time together on conferences and group activities. Thank you Reini, without your incentive I would have never applied for writing my master's thesis in Munich.

I especially want to thank Prof. Sax from Graz for being my advisor. The current constellation on how I am writing my thesis is symptomatic for my unfortunate talent of making simple things complicated, like my bachelor's thesis in Graz. Thank you, Prof. Sax for your patience and support over the last few years.

I would also like to especially thank Prof. Reuter for accepting me into his working group in Munich and allowing me to attend multiple conferences during my master's thesis. Thank you for your academic and financial support and the opportunity to stay three more years in Munich.

I would also like to thank the working group and the colleagues in my office in Munich for the warm welcome and very comfortable atmosphere. It is a pleasure for me to be a member of the mensa-boycott lunch group, being able to enjoy serious and less serious conversations day after day. I am honored to be a founding member of the coffee cooperative society.

Thank you to all my friends in Graz whom I am so lucky to be studying with, without you the last six years would not have been the same! Thank you for always giving me a warm welcome whenever I come back to Graz and being always available in personal, professional, and less professional matters. Thank you, Yu-Meng for your support and motivation in the last three years and especially the last two months leading to the completion of this thesis.

Last but not least, I would like to thank my family and relatives for supporting me in my decision of going to Munich and enabling me to study in the first place. Thanks to my parents for their support and for the chance to study without worries and even enjoy the luxury of going abroad. Thank you to my aunt Sylvia for not only accomodating me in Munich but also the long and interesting conversations we shared.

I acknowledge thankfully the financial support offered by the Erasmus-SMP exchange program.

Georg S. Michelitsch
Graz, Austria, June 2014